Ultra-low temperature dilatometry

by

John Leonard Dunn

A thesis
presented to the University of Waterloo
in fulfillment of the
thesis requirement for the degree of
Master of Science
in
Physics

Waterloo, Ontario, Canada, 2010

I hereby declare that I am the sole author of this thesis. This is a true copy of the thesis, including any required final revisions, as accepted by my examiners.

I understand that my thesis may be made electronically available to the public.

Abstract

This thesis presents research of two novel magnetic materials, $LiHoF_4$ and $Tb_2Ti_2O_7$. Experiments were performed at low temperatures and in an applied magnetic field to study thermal expansion and magnetostriction using a capacitive dilatometer designed during this project. This thesis presents 3 distinct topics.

This manuscript begins with a thermodynamic description of thermal expansion and magnetostriction. The design of a capacitive dilatometer suitable for use at ultra-low temperatures and in high magnetic fields is presented. The thermal expansion of oxygen free high conductivity copper is used as a test of the absolute accuracy of the dilatometer.

The first material studied using this dilatometer was $LiHoF_4$. Pure $LiHoF_4$ is a dipolar coupled Ising ferromagnet and in an applied transverse magnetic field is a good representation of the transverse field Ising model. An ongoing discrepancy between theoretical and experimental work motivates further study of this textbook material. Presented here are thermal expansion and magnetostriction measurements of $LiHoF_4$ in an applied transverse field. We find good agreement with existing experimental work. This suggests that there is some aspect of $LiHoF_4$ or the effect of quantum mechanical fluctuations at finite temperatures which is not well understood.

The second material studied is the spin liquid $Tb_2Ti_2O_7$. Despite theoretical predictions that $Tb_2Ti_2O_7$ will order at finite temperature, a large body of experimental evidence demonstrates that spins within $Tb_2Ti_2O_7$ remain dynamic to the lowest temperatures studied. In addition $Tb_2Ti_2O_7$ also exhibits anomalous thermal expansion below 20K, giant magnetostriction, and orders in an applied magnetic field. Thermal expansion and magnetostriction measurements of $Tb_2Ti_2O_7$ are presented in applied longitudinal and transverse fields. Zero-field thermal expansion measurements do not repeat the previously observed anomalous thermal expansion. A large feature is observed in thermal expansion at 100mK, in rough agreement with existing experimental work. Longitudinal and transverse magnetic fields were applied to $Tb_2Ti_2O_7$. Longitudinal magnetostriction measurements show qualitatively different behavior than previous observations. These measurements were taken along different crystal axes so direct comparison cannot be made. Thermal expansion measurements in an applied transverse field show evolution with the strength of the applied field. This evolution may relate to an ordering transition, however difficulties in repeatability in a transverse field require that these results be repeated in an improved setup.

Acknowledgements

The work presented here would not have been completed without my supervisor, Rob Hill. I owe Rob many thanks for his patience and guidance throughout my graduate work. His desire for perfection has motivated me to rise to the challenge, and I am better for it. His insight into all aspects of physics, and his ability to explain any concept simply and intuitively has been an invaluable resource since of my 4th year project. Working with Rob has truly been a pleasure.

I would also like to thank my supervisory committee, Jan Kycia and Michel Gingras. They have consistently provided advice and direction when needed, and are a seemingly endless source of knowledge of experimental and theoretical physics. Their critique has been invaluable, I am grateful for this.

Many thanks go to the people who have helped with this project along the way. Issam Alkesho, Yarema Reshitnyk, Will Sim, Claudia Stahl, Will Toews and Kevin Liu have all provided much needed assistance with lab work, helium transfers, or being the only other person foolish enough to still be at work at 2 am on a Saturday night. Thanks go out to all my friends for providing much needed help on class work, for making coffee breaks enjoyably ridiculous, and many pints of beer celebrating both our successes and our failures. The Kycia group is owed many thanks for the hundreds of liters of liquid helium borrowed or provided, and being kindred spirits in the ongoing battle to get experiments to work. This project could not have been completed without the skill of STS: Harman Vander Heide, Andy Coglough, Mike Lang, Peter Kessel, Hiruy Haile, and Andrew Dube have provided invaluable assistance with all jobs large and small. Particular thanks go to Mike Lang for his craftsmanship and attention to detail in machining multiple dilatometers.

I would like to thank my family for their unconditional support through good times and bad. Finally, my incredible fiancée Stef motivated me to begin graduate work at the outset. Her unending source of love and support has kept me motivated and made me a better person.

Dedication

Stand back, I'm going to try science!

Contents

List of Figures

Chapter 1

Introduction

The study of condensed matter typically involves extremely complex systems, requiring an understanding of a multitude of effects which act on a variety of length and energy scales. Understanding these behaviors begins with consideration of simple toy models which can reproduce salient features, but lack an in-depth description of material properties. Occasionally serendipitous materials are found which can be modelled almost completely using these simple toy models.

The goal of this thesis has been to develop a measurement apparatus which can be used to investigate the phase diagrams of exotic materials, in order to determine when these materials deviate from model behavior. Thermal expansion was chosen as the response to be measured, using capacitive dilatometry. The relationship between thermal expansion and the Gibbs free energy, as well as heat capacity and the Grüneisen parameter ensures that thermal expansion will be a good measurement technique in identifying phase transitions. Heat capacity is a broadly used technique in identifying phase transitions; capacitive dilatometry is a simpler measurement technique which is easily used in an applied magnetic field.

This thesis begins with a description of the thermodynamics of first and second order phase transitions, providing theoretical background of thermal expansion and magnetostriction. Capacitive dilatometry, and the dilatometers used in this work, are described in Chapter 3. The analysis, sources of error, and strengths and weaknesses of this tool are discussed there.

Chapter 4 presents an investigation of the phase diagram of $LiHoF_4$ near the classical, zero field phase transition. $LiHoF_4$ exhibits ideal Ising ferromagnetism at low temperatures [8, 7]. At low temperatures and in an applied transverse field, the Hamiltonian which describes $LiHoF_4$ can be reduced to the transverse field Ising model, making this material an ideal candidate for study. Good agreement is found with existing experimental work [11]. This confirms the existing discrepancy between experimental and theoretical work [79] and indicating that some aspect of $LiHoF_4$ is being overlooked in current theoretical descriptions.

Chapter 5 presents a preliminary dilatometric study of $Tb_2Ti_2O_7$. $Tb_2Ti_2O_7$ is a frustrated pyrochlore magnet, similar to $Ho_2Ti_2O_7$ and $Dy_2Ti_2O_7$. $Ho_2Ti_2O_7$ and $Dy_2Ti_2O_7$ can be successfully described by the dipolar spin-ice model, however the dipolar spin-ice model applied to $Tb_2Ti_2O_7$ fails to described the behavior of $Tb_2Ti_2O_7$ [32]. $Tb_2Ti_2O_7$ remains poorly understood by the theoretical community, this chapter outlines further experiments which could be undertaken.

The appendices conclude this manuscript with technical information for use and fabrication of the dilatometer presented in this work.

Chapter 2

Theoretical Background

As discussed in Chapter 1, the goal of this experimental work is to measure phase transitions in exotic materials at ultra-low temperatures and in high magnetic fields. This chapter discusses thermal expansion and magnetostriction in terms of their use in detecting phase transitions, with a focus on application to magnetic systems. A more general treatment can be found in the texts by Stanley [76], Yates [86], Schwabl [72] or the report by Lee [45].

Phase transitions can be broadly categorized into two distinct types: 1st and 2nd order (or continuous) phase transitions. These two types are distinguished by a discontinuity in the 1st or 2nd (or higher order) derivative of a thermodynamic potential, such as the Gibbs free energy or Helmholtz free energy as shown in Figure 2.1. In order to identify a phase transition a measurement technique which probes one of these potentials is required. Many texts present thermodynamic potentials using volume or magnetization as intensive variables. This is not sufficient for this work, so we will begin by writing the partition function in the grand canonical ensemble. We can then derivative thermodynamic relations using volume, pressure, magnetization and magnetic field. This will allow us to express thermal expansion and magnetostriction in terms of thermodynamic potentials, and to illustrate the usefulness of these two measurement techniques in detecting phase transitions.

The grand canonical ensemble considers a macroscopic number of microscopic ensembles. Here we will replace the (typically present) number of particles in a specific ensemble (N_j) with the magnetization of that ensemble (m_j) [54].

$$Z = \sum_{i,j} e^{-\beta E_i - h m_j} \tag{2.1}$$

Where the summation is over all ensembles n_{ij}, where an ensemble n_{ij} has energy E_i and magnetization m_j. $\beta = \frac{1}{kT}$ and $h = -\beta H$ are the conjugate variables. k is the Boltzmann constant,

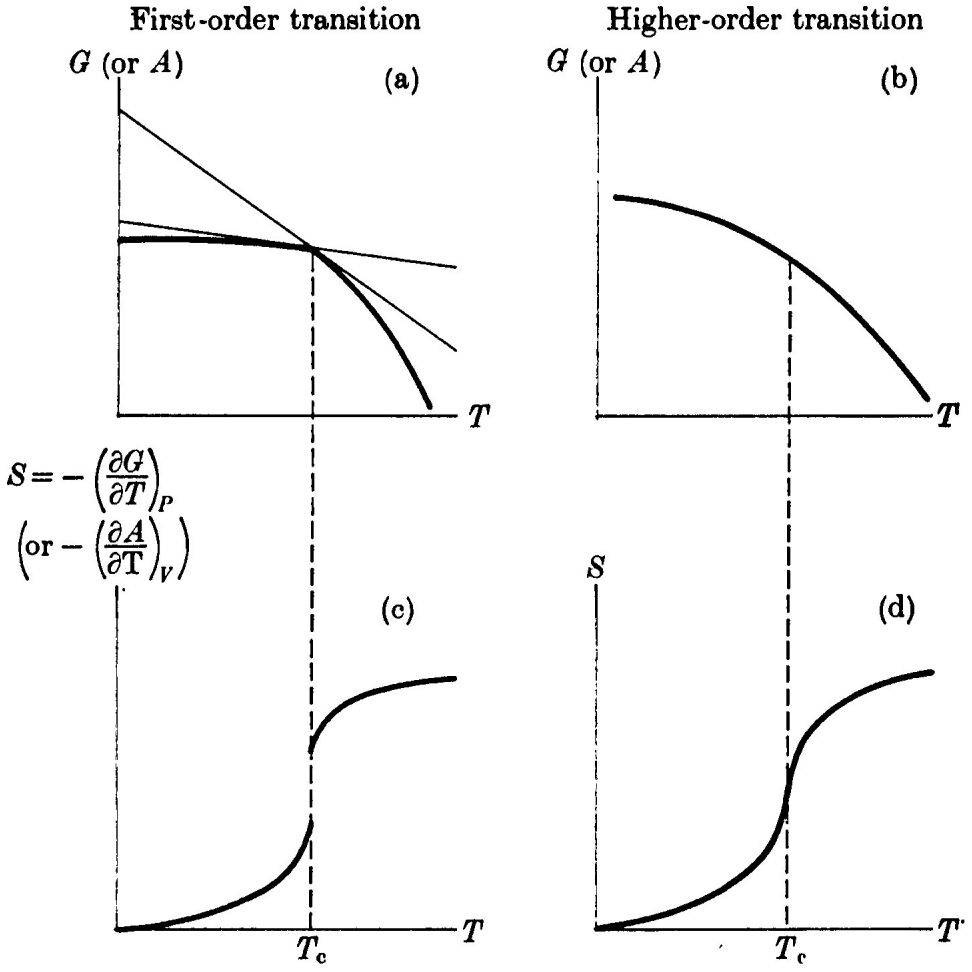

Figure 2.1: Schematic of 1st and 2nd order phase transitions, from Stanley [76]. The temperature dependence of the Gibbs free energy (G) at constant pressure (or equivalently the Helmholtz free energy (A) at constant pressure) is shown in a or b for a first or second order phase transition at $T = T_c$. The entropic response is shown in c and d. In both c and d, the specific heat $C \approx dS/dT$ diverges at T_c.

T is temperature and H is the applied magnetic field. The choice of $h = -\beta H$ is made to remain consistent with Stanley [76], it's physical ramifications are discussed in the references contained therein (particularly illustrative is Reif's treatment [60]). The expectation values are defined as:

$$
\begin{aligned}
< E > &= -\frac{\partial \ln(Z)}{\partial \beta} = \frac{1}{Z}\sum_{i,j} E_i e^{-\beta E_i - h m_j} = U \\
< P > &= \frac{-1}{\beta}\frac{\partial \ln(Z)}{\partial V} = \frac{1}{Z}\sum_{i,j} \frac{\partial E_i}{\partial V} e^{-\beta E_i - h m_j} = P \\
< m_j > &= -\frac{\partial \ln(Z)}{\partial h} = \frac{1}{Z}\sum_{i,j} h e^{-\beta E_i - h m_j} = M
\end{aligned} \tag{2.2}
$$

Where P, V, and T are pressure, volume and temperature. The complete derivative of $\ln(Z)$ is then:

$$
\begin{aligned}
d\ln(Z) &= \frac{\partial \ln(Z)}{\partial \beta} d\beta + \frac{\partial \ln(Z)}{\partial V} dV + \frac{\partial \ln(Z)}{\partial h} dh \\
&= -U d\beta + \beta P dV - M dh
\end{aligned}
$$

Add $d(\beta U + Mh)$ to both sides

$$
d(\ln(Z) + \beta U + Mh) = \beta dU + \beta P dV + h dM
$$

Rearranging for dU:

$$
\begin{aligned}
\beta dU &= d(\ln(Z) + \beta U + Mh) - \beta P dV - h dM \\
dU &= \frac{1}{\beta} d(\ln(Z) + \beta U + Mh) - P dV - \frac{h}{\beta} dM
\end{aligned} \tag{2.3}
$$

The infinitesimal internal energy is defined as $dU \equiv dQ - dW$. We can compare the result of Equation 2.3, knowing that $dQ = T dS$.

$$
\begin{aligned}
\frac{S}{k} &= \ln(Z) + \beta U + Mh \\
h &= -\beta H \\
S &= k\ln(Z) + \frac{U}{T} - \frac{MH}{T}
\end{aligned} \tag{2.4}
$$

Where Q, W, and S are heat, work, and entropy. We find the derivative of internal energy is:

$$dU = TdS - PdV + HdM \tag{2.5}$$

Stanley [76] presents the thermodynamic relationships of a magnetic system by replacing volume with volume with the negative of magnetization, and pressure with applied field in the infinitesimal expression of work, dW, and deriving the relevant relationships from this initial assumption. Naively this suggests that one may simply assume the expression given in Equation 2.5, the previous presentation demonstrates the validity of this intuitive assumption. For further confirmation, we can determine the Helmholtz free energy A using the definition $A = -\ln(Z)/\beta$, and recalling that A is a function of temperature, volume, and magnetic field, $A(T, V, H)$. This requires that we revisit the derivative of $\ln(Z)$.

$$\begin{aligned} d\ln(Z) &= \frac{\partial \ln(Z)}{\partial T}dT + \frac{\partial \ln(Z)}{\partial V}dV + \frac{\partial \ln(Z)}{\partial M}dM \\ &= \frac{1}{kT^2}UdT + \frac{1}{kT^2}MHdT + \frac{1}{kT}PdV - \frac{1}{kT}HdM \\ &= k\beta^2 UdT + k\beta^2 MHdT + \beta PdV - \beta HdM \end{aligned} \tag{2.6}$$

We can now use the expression for $\ln(Z)$ from Equation 2.4 and $d\ln(Z)$ from Equation 2.6 to find the free energy, $A(T, V, H)$.

$$\begin{aligned} A &= \frac{-1}{\beta}\ln(Z) \\ dA &= -\ln(Z)d\frac{1}{\beta} - \frac{1}{\beta}d\ln(Z) \\ \text{Let: } \ln(Z) &= S/k - \beta U - \beta MH \\ \text{And: } d\ln(Z) &= k\beta^2 UdT + k\beta^2 MHdT + \beta PdV - \beta HdM \\ dA &= (-S/k + \beta U + \beta MH)d\frac{1}{\beta} - \frac{1}{\beta}(k\beta^2 UdT + k\beta^2 MHdT + \beta PdV - \beta HdM) \\ &= -SdT + \beta Ud\frac{1}{\beta} - \beta MHd\frac{1}{\beta} - k\beta UdT - k\beta MHdT - PdV + HdM \\ \text{Let: } \beta &= \frac{1}{kT}, \text{ and so: } d\frac{1}{\beta} = kdT \\ dA &= -SdT + \frac{U}{T}dT + \frac{MH}{T}dT - \frac{U}{T}dT - \frac{MH}{T}dT - PdV + HdM \\ dA &= -SdT - PdV + HdM \end{aligned} \tag{2.7}$$

We can now write the thermodynamic potentials for a magnetic system, including the standard pressure, volume, temperature variables with the magnetic field and magnetization, by using the thermodynamic definitions given in Stanley [76]. Below are the internal energy (U), the Helmoltz free energy (A), the Gibbs free energy (G), and the enthalpy (E) [45, 60, 76, 72].

$$\begin{aligned} U &= Q - W \rightarrow dU = TdS - PdV + HdM \\ A &= U - TS \rightarrow dA = -SdT - PdV + HdM \\ G &= U - TS + PV - HM \rightarrow dG = -SdT + VdP - MdH \\ E &= U + PV - MH \rightarrow dE = TdS + VdP - MdH \end{aligned} \tag{2.8}$$

To derive the Maxwell relations, we require the lemma below for some function $df = u(x,y)dx + v(x,y)dy$ [76].

$$\begin{aligned} \left(\frac{\partial u}{\partial y}\right)_x &= \frac{\partial^2 f}{\partial x \partial y} = \left(\frac{\partial v}{\partial x}\right)_y \\ \text{And: } u(x,y) &= \left(\frac{\partial f}{\partial x}\right)_y \end{aligned} \tag{2.9}$$

In this case stated for $f(x,y)$, the generalization to $f(x,y,z)$ is intuitively obvious. We can then derive the Maxwell relations for this systems. Two of interest come from the Gibbs free energy and enthalpy.

$$\begin{aligned} \left(\frac{\partial V}{\partial T}\right)_{H,P} &= \left(\frac{\partial S}{\partial P}\right)_{H,T} \\ \left(\frac{\partial V}{\partial H}\right)_{T,P} &= \left(\frac{\partial M}{\partial P}\right)_{H,T} \end{aligned} \tag{2.10}$$

Also from the lemma above we gain two relationships which will be useful, both from the Gibbs free energy.

$$\begin{aligned} -S &= \left(\frac{\partial G}{\partial T}\right)_{H,P} \\ -M &= \left(\frac{\partial G}{\partial H}\right)_{T,P} \end{aligned} \tag{2.11}$$

With these tools, we can now examine the two main measurement techniques used in this work. Thermal expansion ($\alpha_{H,P}$) in a constant applied field and constant pressure can be written as [76, 86]:

$$\alpha_{H,P} = \frac{1}{V}\left(\frac{\partial V}{\partial T}\right)_{H,P} = -\frac{1}{V}\left(\frac{\partial S}{\partial P}\right)_{H,T} \tag{2.12}$$

Where we used the first relationship of Equation 2.10. Using the first relationship from Equation 2.11 thermal expansion can be related to the Gibbs free energy:

$$\alpha_{H,P} = \frac{1}{V}\frac{\partial^2 G}{\partial T \partial P} \tag{2.13}$$

Which shows that thermal expansion is related to the second derivative of the Gibbs free energy and so will act as a good probe of first or second order phase transitions. In both cases, the transition will appear as a discontinuity in thermal expansion (as the gradient of entropy diverges in Figure 2.1) as the system moves past the critical temperature. First order transitions could be distinguished from a second order transition by integrating thermal expansion and observing any discontinuous changes in volume. To relate thermal expansion to some other forms of measurement, we will make use of a second lemma [76].

$$-1 = \left(\frac{\partial x}{\partial y}\right)_z \left(\frac{\partial y}{\partial z}\right)_x \left(\frac{\partial z}{\partial x}\right)_y \tag{2.14}$$

Applying this lemma to $(\partial S/\partial P)_{H,T}$, we find:

$$-\left(\frac{\partial S}{\partial P}\right)_{H,T} = \left(\frac{\partial S}{\partial T}\right)_{H,P}\left(\frac{\partial T}{\partial P}\right)_{H,S} \tag{2.15}$$

Now we can use this in the right term of the expression for thermal expansion in Equation 2.12.

$$\begin{aligned} \alpha_{H,P} &= \frac{1}{V}\left(\frac{\partial S}{\partial T}\right)_{H,P}\left(\frac{\partial T}{\partial P}\right)_{H,S} \\ \alpha_{H,P} &= C_{P,H}(T)\gamma \\ \text{where: } C_{P,H}(T) &= T\left(\frac{\partial S}{\partial T}\right)_{H,P}, \gamma = \frac{1}{VT}\left(\frac{dT}{dP}\right)_{H,S} \end{aligned} \tag{2.16}$$

Where $C_{P,H}$ is the specific heat capacity at constant pressure, and γ is the Grüneisen parameter. In this case the partial derivative of temperature and pressure becomes a complete derivative; this arises from considering movement along a line of constant entropy in a static magnetic field [76]. The Grüneisen parameter can also be written as $\Gamma = [1/(VE^*)](\partial E^*/\partial P)$, where E^* is the relevant energy scale (ie: the Fermi energy in a metal) near a critical point[87, 33]. In a classical phase transition this is constant in each phase [44], so the thermal expansion will mimic the behavior of the specific heat. Near a quantum critical point the relevant energy scale vanishes, and so the Grüneisen parameter is divergent[87, 33]

Specific heat has been a common tool in identifying phase transitions in material, providing information regarding the entropy and the density of states in a material and being accessible both experimentally and theoretically. The advantage of using thermal expansion is that it is a much simpler measurement technique which is more readily adaptable to use in magnetic fields, as will be discussed in Section 3.0.1.

The second measurement technique used within this body of work is magnetostriction. The term 'magnetostriction' is used in this work to signify any change in volume of a material due to an applied field and hence covers both 'parastriction' (the change in volume of a paramagnetic material due to an applied field) and the alternative, stricter definition of 'magnetostriction' (the change in volume of a magnetically ordered material due to an applied field). Magnetostriction can be defined as:

$$\lambda = \frac{1}{V}\left(\frac{\partial V}{\partial H}\right)_{P,T} \tag{2.17}$$

And using the relationship listed in Equations 2.10 the magnetostriction can be related to the Gibbs free energy.

$$\lambda_{P,T} = \frac{1}{V}\left(\frac{\partial^2 G}{\partial P \partial H}\right)_{T} \tag{2.18}$$

Again, it is useful to relate the magnetostriction to other measurement techniques. We can

now use the second relationship in Equation 2.10 and apply the lemma in Equation 2.14 to $(\partial M/\partial P)_{H,T}$ to relate magnetostriction to other kinds of measurements. Magnetostrictive measurements are most easily performed at constant temperature, so we may begin by applying the lemma to $(\partial M/\partial P)_{H,T}$ while remaining at constant temperature throughout:

$$\left(\frac{\partial M}{\partial P}\right)_{H,T} = -\left(\frac{\partial H}{\partial P}\right)_{M,T}\left(\frac{\partial M}{\partial H}\right)_{P,T}$$
$$\text{Apply the lemma again: } \left(\frac{\partial H}{\partial P}\right)_{M,T} = -\left(\frac{\partial T}{\partial P}\right)_{H,T}\left(\frac{\partial H}{\partial T}\right)_{P,T} \tag{2.19}$$

Now we use these relationships in the definition of magnetostriction.

$$\begin{aligned}
\lambda_{P,T} &= -\frac{1}{V}\left(\frac{\partial M}{\partial P}\right)_{H,T} \\
&= \frac{1}{V}\left(\frac{\partial H}{\partial P}\right)_{M,T}\left(\frac{\partial M}{\partial H}\right)_{P,T} \\
&= \frac{1}{V}\left(\frac{\partial M}{\partial H}\right)_{P,T}\left(\frac{\partial T}{\partial P}\right)_{H,S}\left(\frac{\partial H}{\partial T}\right)_{M,P} \\
\lambda_{P,T} &= \frac{\chi_T \gamma}{\Gamma_H} \qquad (2.20) \\
\text{Where: } \chi_T &= \left(\frac{\partial M}{\partial H}\right)_{P,T}, \gamma = \frac{1}{VT}\left(\frac{dT}{dP}\right)_{H,S}, \Gamma_H = \frac{1}{T}\left(\frac{\partial T}{\partial H}\right)_{M,P}
\end{aligned}$$

Where χ_T is the magnetic susceptibility and Γ_H is the magnetocaloric effect. The magnetic susceptibility is another common measurement technique and has been useful in the study of spin ices and glasses [32]. The magnetocaloric effect is the measurement of a change in temperature with an adiabatic change in the applied magnetic field, H. The magnetocaloric effect can display a variety of behavior near a critical point[6], and is expected to diverge near a quantum critical point[87, 33]

In Equations 2.16 and 2.20 it has been shown that measurement of a change in volume while either temperature or applied field is varied is related to the second derivative of the Gibbs free energy. This indicates that either thermal expansion or magnetostriction will be useful tools in determining phase boundaries of first or second order phase transitions. In addition, useful relationships have been made which connect thermal expansion and magnetostriction to other measurement techniques and material properties. Prepared with this knowledge, we now move to a discussion of the method of measuring such volume changes.

Chapter 3

Apparatus

3.0.1 Capacitive Dilatometry

A major goal of this work has been to produce an accurate, useable tool to detect linear thermal expansion and magnetostriction in a variety of materials. Capacitive dilatometry has been used to detect a variety of effects, notably the identification of secondary superconducting phases in UPt_3 using thermal expansion [70], and lattice anomalies induced by a magnetic field in $CeCoIn_5$ using magnetostriction [22]. As shown in Chapter 2, thermal expansion is able to probe first or second order phase transitions and provide information on the Grüneisen parameter when coupled with specific heat measurements. This section will develop a simple picture of the function of the dilatometer used to measure thermal expansion in this work, and discuss details of using dilatometry to measure the thermal expansion or magnetostriction of an unknown sample. Further details regarding the type of materials used, fabrication, assembly, and use of the dilatometer can be found in Appendices A and B.

Capacitive dilatometry is a conceptually simple idea: by fixing the position of one plate of a capacitor and anchoring the other plate to a sample, accurate measurement of a change in length of the sample can be measured. In the case of a perfect parallel plate capacitor this capacitance can be converted to the plate separation using the expression $C = \frac{\epsilon_0 A}{g}$, where ϵ_0 is the permittivity of free space, A is area of a capacitor plate, and g is the separation between the capacitor plates. White [81] was the first to build a functioning dilatometer, and while there have been significant improvements in the measurement technology such as improvements in capacitance bridges and reference capacitors [1], the concept remains the same. The dilatometer used here is conceptually similar to that introduced by White [81] in making use of an ideally parallel plate capacitor. By varying the temperature of the sample the capacitance measurements can be used to compute changes in the gap g caused by the sample, which can then be used to determine the linear thermal expansion coefficient $\alpha(T) = \frac{1}{L}\frac{dL}{dT}$. Similarly, by varying an applied magnetic field the magnetostriction $\lambda(H) = \frac{\Delta L}{L}$ can be determined from capacitance measurements. In all of the

dilatometric measurements made throughout this thesis, thermal expansion or magnetostriction refers to the linear thermal expansion coefficient or linear magnetostriction.

3.0.2 Silver Compact Dilatometer

A photograph and a representative sketch of the dilatometer used in this work is shown in Figure 3.1. The dilatometer in this work is fabricated predominantly from 99.995% pure silver. The shell provides a ground plane around the capacitor plates, and maintains coaxial alignment of the components. The upper capacitor plate is fixed within a lock ring threaded at 3.14 turns/mm by an insulating sapphire washer. When the upper capacitor plate is in the desired position, a lock nut on the lock ring is tightened against the shell to hold the upper assembly (lock ring, sapphire washer, and capacitor plate) in place. The lower capacitor plate is fastened to an insulating sapphire cross. The sapphire cross is then pressed against the sample. The sapphire cross passes through a beryllium copper spring, which is depressed to maintain the contact between the lower capacitor plate and the sample. The sample is fastened to the sample holder using a silver paint, which provides mechanical stability and thermal contact. An uncalibrated resistance thermometer is fastened to the base of the sample holder and used to verify thermal stability of the sample. The sample holder sits inside the lower lock ring (also threaded at 3.14 turns/mm) which can be used to control the position of the sample holder. A lock nut is also used to maintain the position of the lower lock ring.

The lock rings and lock nuts are fabricated out of A316 medical grade stainless steel, the spring is made of hardened beryllium copper, the sapphire washer and cross are made of commercial Al_2O_3, all other components are fabricated of 99.995% pure silver. Silver was used for its desirable properties at ultra-low temperatures and high magnetic fields. In this regime pure silver (as opposed to copper) does not develop a large specific heat capacity and maintains high thermal conductivity [74]. A316 stainless steel was used to maintain a small magnetic response of the dilatometer after extended thermal cycling and exposure to high magnetic fields. In contrast to A304 stainless steel (the more common variety), A316 does not develop a ferromagnetic response after repeated thermal cycling and exposure to a strong magnetic field. Beryllium copper was used for the spring for its desirable hardness at cryogenic temperatures [56]. Sapphire components were used to provide electrical insulation and repeatable thermal expansion. Where necessary, Stycast 2850FT epoxy was used to fasten components together. This was done such that there was no Stycast epoxy along the central long axis of the dilatometer, and so would not contribute significantly to the thermal expansion of the dilatometer.

The dilatometer used in this work is made of paramagnetic materials which should all have very small magnetostrictive responses [25] (shown in Figure 3.2), and when compared to the magnetostriction of a responsive sample it may be possible to approximate the magnetostrictive response of the measurement cell to zero. As with the thermal expansion cell effect, the magnetostrictive cell effect should be considered and dealt with appropriately for all investigations.

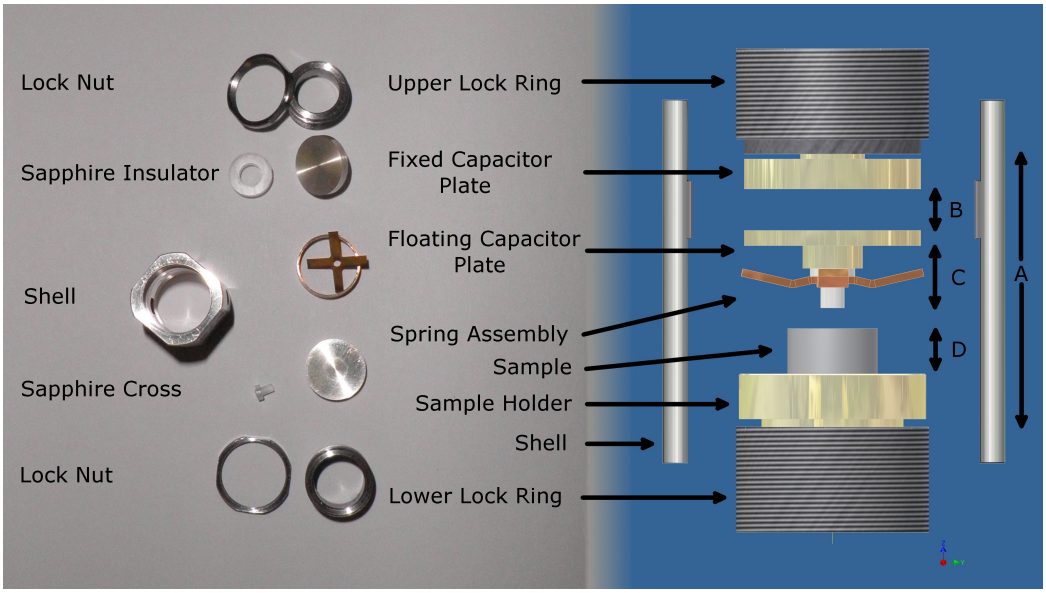

Figure 3.1: Left: A photograph of an unassembled capacitive dilatometer. Right: Schematic of the dilatometer. The shell is a silver rod in which a cylindrical bore through its length maintains coaxial alignment of all other components and provides a ground plane around the capacitor plates. Both ends of the shell are threaded at 3.14 turns per millimeter. The upper lock ring threads into the silver shell and controls the position of the upper capacitor plate. The lower capacitor plate is anchored to the spring via a sapphire cross. The sample is then pressed against the sapphire cross, depressing the spring to maintain contact between the sapphire cross and the sample. The sample is mounted to the sample holder via silver paint or silver epoxy. The sample holder is held in place with the lower lock ring. The lower lock ring threads into the silver shell. Ultimately, the lower lock ring can be threaded in or out of the shell to control the spring deflection and position of the sample.

3.0.3 Cell Effect

The importance of the cell effect depends largely on the goals of the measurement being performed. In the case of a first or second order phase transition (such as that in $LiHoF_4$, see Chapter 4), the goal is to identify the critical temperature or field at which the phase transition takes place. If the cell effect is significantly smaller than the measured signal, or featureless in the region of interest, then the feature which identifies the critical point will be distinguishable without removing the cell effect from the measured data. Alternatively if a quantitative measure of thermal expansion is desired or the cell effect exhibits a significant feature within the region of interest, then the cell effect must be accurately measured and taken into account using Equation 3.4 to calculate the linear thermal expansion coefficient. In all cases the relevance of the cell effect should be considered and the necessary analysis undertaken.

If detailed quantitative information is required it is important to understand the effects of the thermal expansion of the dilatometer itself and the effect this will have on the measured thermal expansion. To decouple the behavior of the sample from the measured capacitance changes two pieces of information are required: the behavior of the dilatometer with using a silver sample (known as the cell effect), and the behavior of the dilatometer with an unknown sample. To see this, consider increasing the temperature of the dilatometer; as temperature increases, the silver shell will expand. The position of the lock rings will be primarily determined by the expansion of the silver shell between them (labelled 'A' in Figure 3.1), and not their own thermal contraction since both lock rings are held in place via their threaded outer diameter. This expansion will push the extremal lock rings away from each other. If nothing else changes, increasing the separation of the lock rings would increase the separation of the capacitor plates.

Next consider the thermal expansion of the capacitor plates and the sample holder as the temperature is increased. When these components expand they will push the capacitor plates closer together, decreasing the plate separation. Since the sample holder and the capacitor plates are made of the same 99.995% pure silver as the shell, they will balance the effect of the shell on the separation between the capacitor plates. Thus, if the dilatometer is heated the expansion of the silver sample holder and the silver capacitor plates will balance the effect of the silver shell and will produce no change in capacitance due to these components.

The sections left to consider are those labelled B, C, and D in Figure 3.1. For these sections, we must consider both the expansion of the material within these lengths (which decreases the separation of the capacitor plates) and the expansion of the silver shell (which increases the separation of the capacitor plates). An important point is that we will consider the effect the thermal expansion of these components will have on the separation of the capacitor plates, and not their own absolute thermal expansion. In the following, capital letters (B, C, D) denote the length of the respective section. Thermal expansion of a material is noted by α_{Ag}, using Silver (Ag) as an example. The change in the capacitor gap in a given section is denoted by G_{B}, using section B for example.

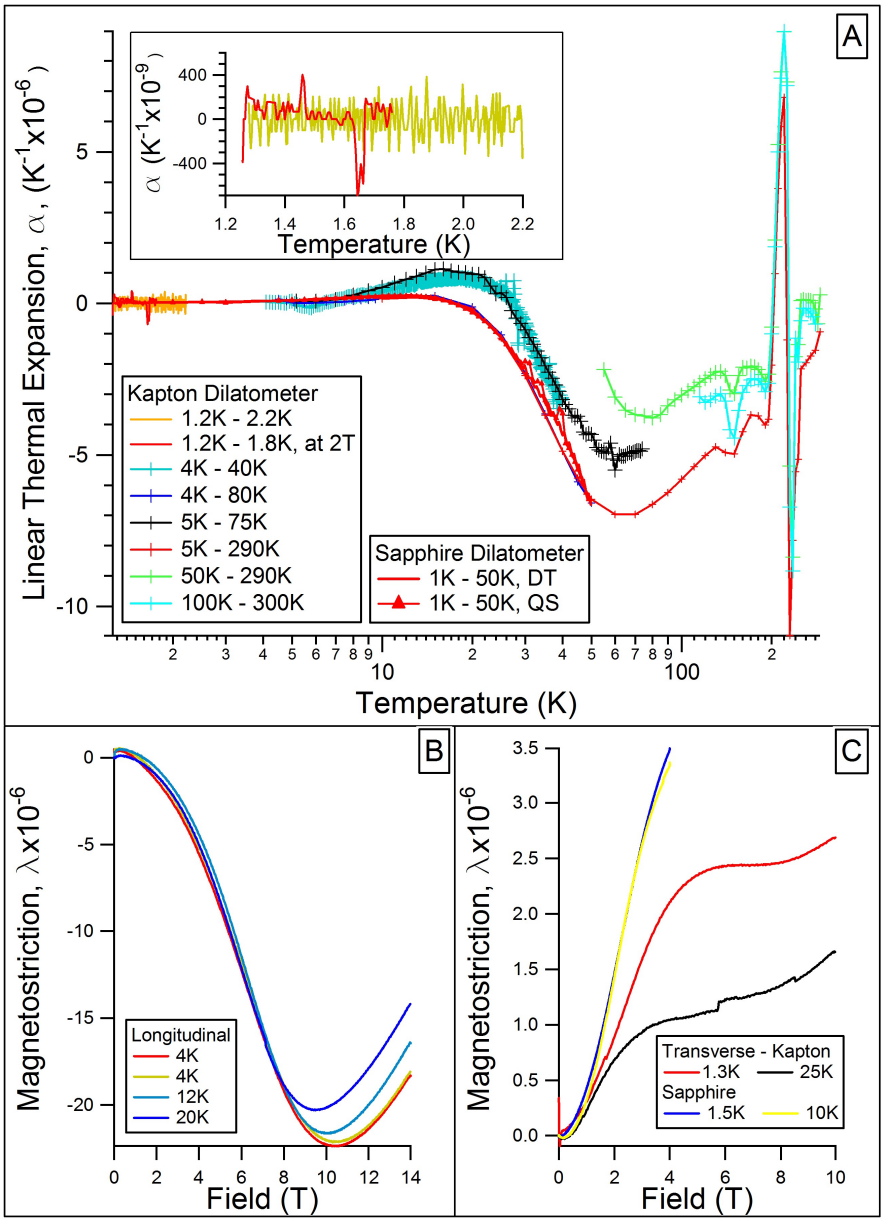

Figure 3.2: Top: Cell effect of dilatometers using Kapton or Sapphire, measured using thermal expansion showing slight differences in the high temperature behavior, but qualitatively reproducible response. Top inset: Thermal expansion of the Kapton dilatometer from 1.2K - 2.2K. Empirically, a large portion of the differences can be attributed to differing experimental parameters and temperature control, as discussed in text. Bottom: Cell effect of the Kapton dilatometer measured via magnetostriction ($\lambda(H) = \frac{\Delta L}{L}$) in the longitudinal (left) and with the Sapphire dilatomter in the transverse (right) orientations. All experiments made use of a silver sample 2.3 mm ± 0.05 mm. The Kapton data in all panels was taken using the same dilatometer as in the $LiHoF_4$ investigation.

In section B there is no material whose expansion counteracts that of the silver shell. The effect will therefore be to increase the separation of the capacitor plates by an amount $\frac{dG_B}{dT} = B\alpha_{Ag}$. Within section C, the expansion silver shell will work to increase the separation of the capacitor plates, while the expansion of the sapphire component will decrease the plate separation. The sum of these two expansions within section C will increase the separation of the capacitor plates by an amount $\frac{dG_C}{dT} = C\alpha_{Ag} - C\alpha_{Al_2O_3}$. Finally, section D contains the sample under investigation. By similar logic, this section will increase the capacitor plate separation by an amount $\frac{dG_D}{dT} = D\alpha_{Ag} - D\alpha_{Sample}$.

The measured thermal expansion will be the sum of each of these contributions.

$$\left.\frac{dB}{dT}\right|_{\text{Cell+Sample}} = \frac{dG_B}{dT} + \frac{dG_C}{dT} + \frac{dG_D}{dT} \tag{3.1}$$

$$\left.\frac{dB}{dT}\right|_{\text{Cell+Sample}} = (B + C + D)\alpha_{Ag} - C\alpha_{Al_2O_3} - D\alpha_{Sample} \tag{3.2}$$

We wish to isolate the linear thermal expansion of the unknown sample. Recognizing that if the sample in the dilatometer is silver, we can define the cell effect as Equation 3.2 where $\alpha_{Sample} = \alpha_{Ag}$. Rearranging, we find:

$$\alpha_{Sample} = \frac{-1}{D}\left[\left.\frac{dB}{dT}\right|_{\text{Cell+Sample}} - \left.\frac{dB}{dT}\right|_{\text{Cell+Ag}}\right] + \alpha_{Ag}\left(1 + \frac{B_{Sample} - B_{Ag}}{D}\right) \tag{3.3}$$

Where B_X is the capacitor plate separation when the silver or unknown sample is measured. Ideally, these two terms will cancel perfectly. In practice, the magnitude of this term can be estimated or measured and included in the analysis if necessary. Typically this term is small enough to ignore, and the relation between the measured thermal expansion, and the thermal expansion of an unknown is then:

$$\alpha_{Sample} = \frac{1}{L}\left.\frac{dL}{dT}\right|_{\text{Cell+Sample}} - \frac{1}{L}\left.\frac{dL}{dT}\right|_{\text{Cell+Ag}} + \alpha_{Ag} \tag{3.4}$$

Where D has been relabelled L and is the length of the sample, and dB, the change in the capacitor gap, as been replaced by $-dL$, the change in the sample length. Equation 3.4 provides the basis for measurement of linear coefficient of thermal expansion using a capacitive dilatometer.

The cell effect of two different version of dilatometer from 1K to 50K are shown in Figure 3.2. The dilatometer referred to as the Sapphire dilatometer is described in this chapter. The other dilatometer, referred to as the Kapton dilatometer is an earlier version used in both the $LiHoF_4$and $Tb_2Ti_2O_7$measurements. The Kapton dilatometer made use of Kapton polyimide film as an insulator between the spring and the floating capacitor plate, using Stycast 2850 epoxy as a bonding agent. This version of the dilatometer was found to have a settling time of several hours at millikelvin temperatures, and this was thought to arise from the use of Stycast and Kapton directly along the measurement axis. This is shown in Chapter 5, Figure 5.13.

Figure 3.2 also shows a lack of reproducibility in thermal expansion. This is most apparent at the high temperature regime, however it does propagate to lower temperatures. This lack of reproducibility, and consequently the accuracy of the thermal expansion measurements being made, was tested by measuring the thermal expansion of an oxygen-free high-conductivity (OFHC) copper sample. The thermal expansion of OFHC copper and pure silver between 1 and 7K are given in Equation 3.5, and can be seen to differ by a small amount [83].

$$\begin{aligned}\alpha_{\mathrm{Ag}} &= 10^{-10}\Big((1.9 \pm 0.2)T + (1.14 \pm 0.03)T^3 + (2 \pm 2)x10^{-4}T^5\Big)[K^{-1}] \\ \alpha_{\mathrm{Cu}} &= 10^{-10}\Big((2.1 \pm O.1)T + (0.284 \pm 0.005)T^3 + (5 \pm 3)xlO^{-4}T^5[K^{-1}]\end{aligned} \tag{3.5}$$

Not only are the thermal expansion coefficients of silver and copper small (for comparison, thermal expansion of $LiHoF_4$and $Tb_2Ti_2O_7$were both on the order to 10^{-6}), copper only differs from silver by 50% at 2K. This measurement provided a stern test of the accuracy of the dilatometer, which the Kapton dilatometer did not adequately meet (also shown in Figure 5.13). This led to the redesign of the dilatometer to remove Kapton film entirely, and to use Stycast such that it's contribution to measured thermal expansion was minimized. This was achieved by using Stycast to make radial bonds, as opposed to the bond along the long axis of the cylinder. A measurement of the thermal expansion of copper using the sapphire dilatometer is shown in Figure 3.5, and discussed further in Section 3.1.4.

In addition to the differences due to Kapton and Stycast epoxy, several experimental parameters differ between the experimental trials shown in Figure 3.2. The working capacitance was not kept constant, as were heating and cooling rates. Many of these trials took place before the importance of good temperature control was fully appreciated, and so may exhibit temperature fluctuations greater than one part in a thousand (See Section 3.1.2 for further detail). Despite these differences, the behavior of the dilatometer is qualitatively repeatable. Finally, the large spike in thermal expansion near 200K is due to Kapton film and is not observed in the Sapphire dilatometer.

3.1 Experimental Method

Access to the temperature and magnetic field regimes used throughout this work requires some infrastructure. This section will briefly outline the existing equipment used, and the methods used to collect data.

3.1.1 Capacitance Measurement

Capacitance is measured using a Andeen-Hagerling 2500A capacitance bridge, which can then be converted to the capacitor plate separation B using the expression $B = \frac{\epsilon_0 A}{C}$ for perfectly parallel plates. Realistically, capacitor plates are not perfectly parallel and the total capacitance of a tilted capacitor can be determined by integrating the capacitance over the surface of the plates [57]. Equation 3.6 (from [78]) can be used to determine the gap between the capacitor plates in the case of a tilted plate capacitor.

$$B = \frac{\epsilon_0 A}{C}\left[1 + \left(\frac{C}{C_{\max}}\right)^2\right] \tag{3.6}$$

Where ϵ_0 is the permittivity of free space, A is the effective capacitor plate area, $C_{\max}$ is the maximum measured capacitance before the capacitor plates short, and C is the measured capacitance. The first term of this expression provides the capacitor gap of ideal parallel plate capacitor, while the second term provides a correction for a tilted capacitor plate. The maximum capacitance (C_{max}, typically $\approx$ 50 pF) defines the position of the capacitor plates just before they electrically short (leading to C = 0 pF). The effective plate area, A, accounts for an offset of the capacitor plates in the plane of their faces. Together these two factors of $C_{\max}$ and A provide enough information to take into account the tilt and offset of the capacitor plates [71].

The two quantities can be independently measured. The maximum capacitance can be measured prior to beginning a measurement by using the sample to displace the floating capacitor plate until the capacitor plates electrically short. The final observed capacitance is then taken to be $C_{\max}$. The effect of varying $C_{\max}$ can be seen in the top of Figure 3.3. This plot shows the same data set (specifically, a test of $LiHoF_4$ done in zero field) analyzed using differing values of $C_{\max}$ as shown in the legend. Note that the qualitative features of linear thermal expansion remain the same, however the scale of these features varies by as much as 2 orders of magnitude as the $C_{\max}$ approaches the measured capacitance. This is due to the changing scale of the capacitor gap, B. As the working capacitance approaches $C_{\max}$, a small change in the plate separation will yield the same capacitance change as a much larger change in the capacitor gap of a perfect parallel plate capacitor. Compounding this effect, thermal expansion measures the gradient of the capacitor gap with respect to temperature, enhancing this effect.

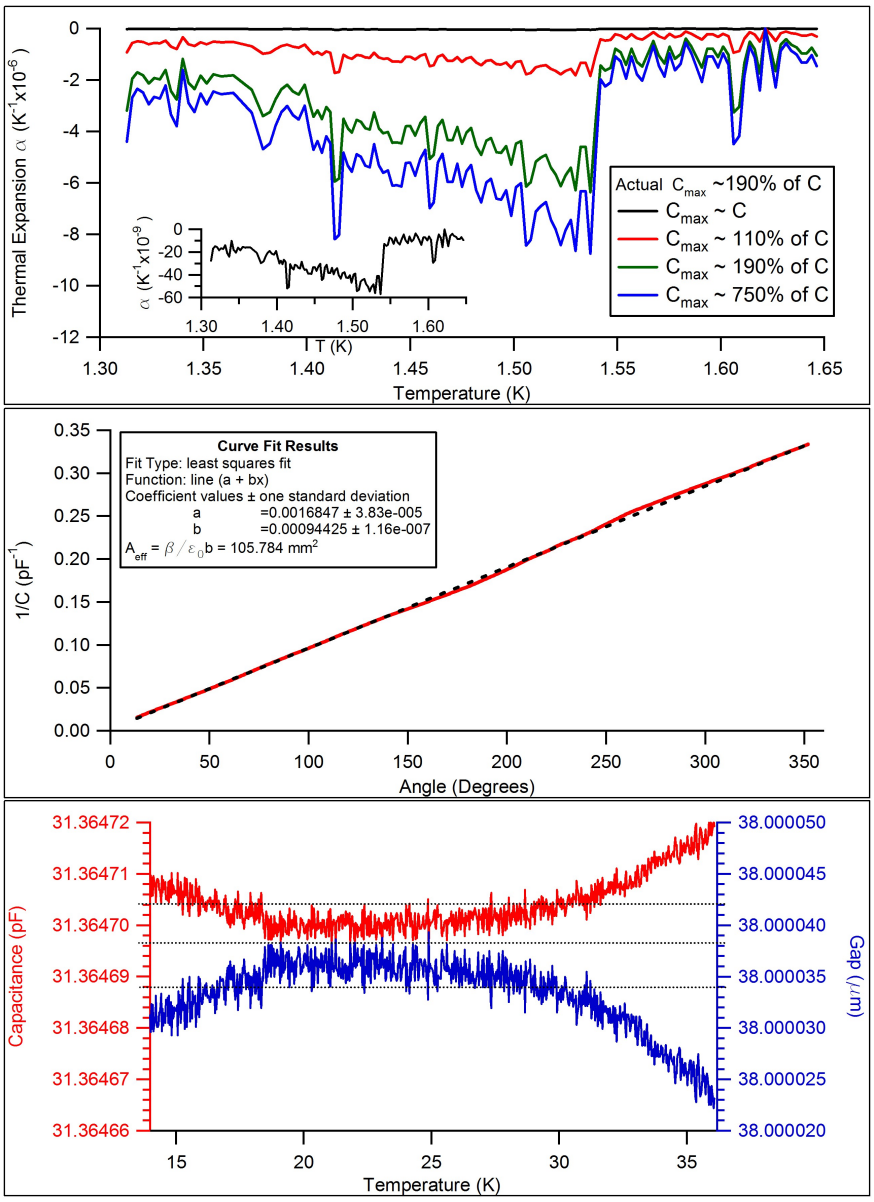

Figure 3.3: Top: The affect of the parameter $C_{\max}$ on analysis of measurements. The inset shows the behavior for $C_{\max} \sim C$. Note that the qualitative features do not change, however the overall scale of measurements can vary by orders of magnitude. The case of the ideal capacitor is indistinguishable from the case of $C_{\max} \approx C$ Middle: $\frac{1}{C}$ versus θ, the rotation of the fixed capacitor plate. The derivative is used to calculate A and should remain constant, see text. Bottom: Stability of the dilatometer, showing capacitance measurement (red) and the capacitor gap (blue) at a controlled temperature (10K) for approximately 20 minutes. The line width, which determines the resolution of the dilatometer without any averaging, is approximately 6aF, or 0.04 Å.

The effective plate area can also be easily measured, however it is less prone to change and does not need to be repeated every measurement. The position of the fixed capacitor plate can be adjusted by threading in or out the upper lock ring. By beginning with the capacitor plates shorted together, the capacitor plate separation can be adjusted by unscrewing the upper lock ring. The lock ring is threaded at 3.14 turns per millimeter, or β = 884 nm/degree and so the capacitor gap is $d = \beta\theta$. Using the expression for an ideal parallel plate capacitor we can now determine the prefactor A as:

$$\frac{1}{C} = \frac{\beta\theta}{\epsilon_0 A} \tag{3.7}$$

Taking the derivative of this line, we can find A. An example of this analysis is shown in the middle of Figure 3.3. The effective plate area of the sapphire dilatometer determined from this figure is 105mm^2, to compare to the actual surface area of the plate of 108.4mm^2. The bottom of Figure 3.3 demonstrates the long-time stability of the dilatometer while temperature is controlled, showing both the raw capacitance and capacitor gap. Once typical operating conditions are taken into account, length changes greater than 0.02 Å can be resolved, as shown in the bottom of Figure 3.3.

3.1.2 Thermal Expansion

A commercial pumped ^{4}He cryostat (provided from Desert Cryogenics) is used to cool a sample mounted in the dilatometer to approximately 1.2 K. The temperature of the pumped ^{4}He cryostat is controlled using a Lakeshore 331 or 332 Temperature controller and measured by a calibrated Cernox CX-1030 thermistor located on the cold stage of the pumped ^{4}He cryostat. Further details on the pumped ^4He system can be found in Somayyeh Rahimi's Masters thesis [59].

In order to access temperatures below the range of the pumped ^{4}He cryostat, an Oxford Instruments MX400 Dilution Refrigerator is used. The base temperature of the dilution insert is 13.4 mK, measured using a standard Oxford Instruments thermistor, with a standard curve calibration. Temperature control of the cold stage of the MX400 is performed using a Lakeshore LS370 AC resistance bridge and a calibrated M64 thermistor. Details regarding this system can be found in Issam Alkhesho's Masters thesis [4].

The level of noise in capacitance measurements differs significantly between the pumped ^{4}He cryostat and the dilution unit, due largely to the different communication lines used. The pumped ^{4}He cryostat uses coaxial cables from the AH2500A capacitance bridge to the dilatometer, totalling approximately 15 feet of coaxial communication lines between the bridge and the dilatometer. This setup requires little effort to achieve a capacitance reading at the limit of the

AH2500A's accuracy, one part in 10^{-7}. In comparison, the wiring in the dilution unit uses approximately 15-20 feet of coaxial cable to reach a breakout box. The wiring from the breakout box to the dilatometer mounted in the dilution unit consists of twisted pairs of copper or superconducting wire. By grounding one member of the twisted pair and using the other as a signal line, these twisted pairs serve as a proxy for coaxial communication lines. A 100kHz PI filter is used to reduce the electrical noise. Without the PI filter, this setup will yield a capacitance reading accurate to one part in 10^{-4}. Use of the PI filter allows measurement of capacitance to one part in 10^{-7}, bringing the inherent electrical noise in the dilution unit on par with the noise of pumped ^{4} probe.

Two types of temperature control have been used, either dynamic or quasi-static temperature control. A dynamic temperature sweep aims to sweep the temperature of the sample at a constant rate through a region of interest. For example, an experimental trial performed on $LiHoF_4$ consisted of a temperature sweep from approximately 1.3 K to 1.8 K at a rate of 7.5 mK/min. Increasing this rate led to an increase in the measured critical temperature indicating a lack of thermal equilibration, and is discussed further in Chapter 4. Quasi-static temperature control warms the dilatometer to a chosen setpoint, and allows thermal equilibration to take place over a chosen settling time. The investigation of thermal expansion of $Tb_2Ti_2O_7$ made use of quasi-static temperature control, starting at a setpoint of 50 mK and warming to 150 mK through a series of 2 mK steps. At each step, the dilatometer would be allowed to thermalize for a period of 35 minutes, then capacitance averaged for a period of 5 minutes and recorded. At temperatures below 100 mK the equilibration time of the dilatometer was found to be increase significantly, necessitating the use of quasi-static temperature control. These effects are discussed further in Chapter 5.

The advantage of a dynamic temperature sweep is the length of time required to complete an experimental trial. A temperature sweep through the region of interest of $LiHoF_4$ took approximately 1 hour to complete, whereas a quasi-static temperature sweep of comparable accuracy would take several hours to complete. The disadvantage to a dynamic temperature sweep is that at lower temperatures, the ramp rate must be decreased to ensure that thermal gradients are minimized over the length of the sample. The Lakeshore 331 or 332 temperature controllers minimum controllable ramp rate is also 0.1 K/min, which necessitates creative use of PID control parameters to dynamically sweep the temperature. It is likely that this temperature control contributed to the level of noise in this type of measurement. In addition, the number of points which are averaged is greatly reduced leading to less accurate measurement of thermal expansion. At temperatures above 1K where $LiHoF_4$ was studied thermal gradients were not an issue; a brief investigation of the response of the uncalibrated thermistor mounted to the sample holder demonstrated that the dilatometer reacted within 30 seconds to temperature changes up to 0.5 K. At temperatures below 100mK this response becomes significantly longer, reaching up to 2 hours (for example when cooling from 100 mK to 20 mK).

The reverse is true for a quasistatic trial. Given the long settling time, thermal equilibration

can be confirmed at the expense of speed. A disadvantage of the quasistatic temperature sweep is the long thermalizing time at millikelvin temperatures of the dilatometer, which is possibly due to slowly thermalizing Stycast epoxy or Kapton film. Stycast epoxy was used in previous versions of the dilatometer (see Chapter 5), and the version of the dilatometer tested below 1 K was found to have a very slow thermalization. This thermal expansion cell-effect was also found to be have some history dependence, possibly also due to the Stycast and Kapton film used in the version tested. This led to problems accurately reproducing data sets in all temperature regions, and the eventual redesign and removal Stycast and Kapton along the measurement axis of the dilatometer, and replacing these components with the sapphire pieces shown in Figure 3.1.

A Note on Temperature Control

The stability of temperature control is quite important, especially when performing quasistatic thermal expansion measurements. The standard expected for academic research is that temperature will be stable to one part in one thousand. Figure 3.4 demonstrates the effects of poor temperature control. Runs DT and QS #1 both had poor temperature control, while QS #2 satisfied the 1/1000 requirement. This trials used the sapphire dilatometer loaded with a silver sample and were done consecutively. The operating capacitance differed by 5pF, while the remaining difference was in the temperature control.

The relation between noise in temperature and noise in capacitance is presumably related through the thermal expansion coefficient of the material under study. Temperature fluctuations for a material with a large thermal expansion will obviously generate more significant noise in the capacitance measurement, leading to larger fluctuations in the capacitance and consequently larger noise in the thermal expansion measurements. The take-home message is that ideally, temperature will be stable within the accuracy of the measurement apparatus.

3.1.3 Magnetostriction

In order to measure magnetostriction, the strength of the magnetic field is increased at the desired rate until the maximum desired field strength is reached using an Oxford Instruments 14 T/16 T magnet. The effect of eddy current heating as the magnetic field varies was investigated using the uncalibrated thermistor mounted to the sample holder. The ramp rate was chosen such that no cooling was observed using the uncalibrated thermistor after the magnetic field reached its chosen value. This ensured that any eddy current heating was smaller than the resolution of temperature measurement at the applied field. Magnetostriction as a function of applied field, $\lambda(H) = \frac{\Delta L}{L}$, is simply calculated from Equation 3.6. The cell effect of the dilatometer is shown in the bottom of Figure 3.2. In the investigations undertaken to date the cell effect has been smaller by at least a factor of 10 than that of the sample and it has been possible to ignore its effects.

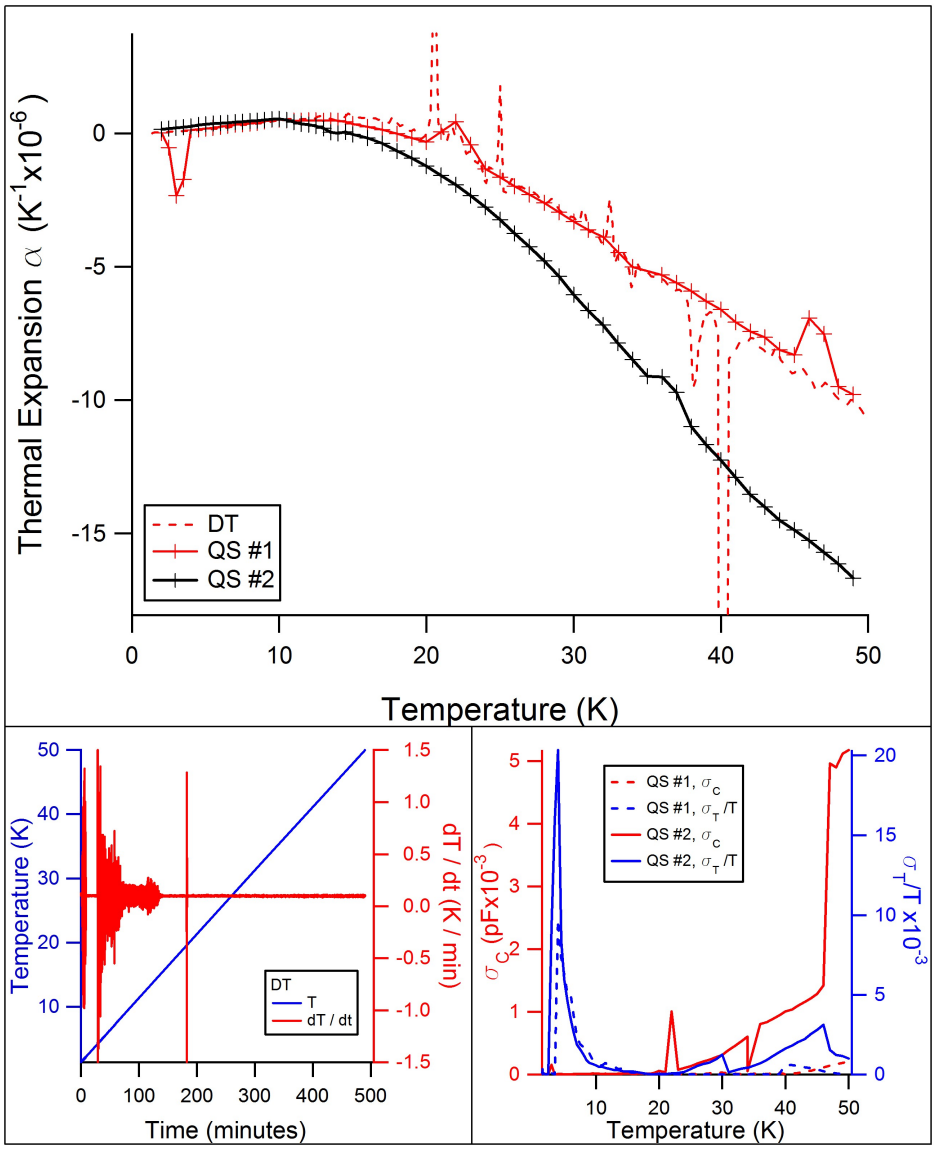

Figure 3.4: The effect of poor temperature control on thermal expansion measurements of silver. QS #2 (where QS indicates quasistatic temperature control) met the requirement of temperature stability to one part in one thousand, while DT (indicating dynamic temperature control) and QS #1 did not. Top: Thermal expansion from 1K to 50K. Bottom left: The temperature and rate of change temperature of DT plotted versus time. The line width at higher temperatures is ±10% of 0.1K, the desired heating rate. Bottom right: The standard deviation of capacitance (σ_C) and the standard deviation of temperature scaled by the average temperature (σ_T/T) versus the temperature. Operating capacitance of QS #1 was ≈17pF, QS #2 was ≈22pF.

3.1.4 Thermal Expansion of Copper

To understand the accuracy and reproducibility of the dilatometer, the thermal expansion of a 2 mm long cylinder of oxygen-free high-conductivity (OFHC) copper was measured. The thermal expansion of copper is well known [84, 82] and OFHC is used as a reference material [84, 82]. Silver and copper have a closely matched thermal expansion, which also served to test the resolution of thermal expansion measurements. The measured responses are shown in Figure 3.5.

Thermal expansion was determined using Equation 3.3. As shown in Figure 3.5, the measured thermal expansion of copper differs by approximately 50% from the accepted values found in [84, 82]. The author believes that this is due to poor temperature control between 4 K and 8 K, and slow thermalization of the dilatometer from 15 K to 30 K. Nevertheless, these experiments can be considered successful and a good indication of the accuracy possible using the capacitive dilatometer. A surprising feature of these results is that neither dynamic temperature control nor quasistatic temperature control clearly provides more accurate results, despite the quasistatic trials taking 2.5 times longer to complete. Examining the upper portion of Figure 3.5, improvements can be made during measurements to reduce noise in the measured response, for example by allowing longer settling time in the quasistatic runs or reducing rate of change of temperature in the dynamic runs.

A worthwhile point to make is that copper was chosen for this trial since it exhibits a small thermal expansion. As we will see in later chapters, the magnitude of the response in both $LiHoF_4$ and $Tb_2Ti_2O_7$ dwarfs the spread of these values, particularly at lower temperatures. The scale of Figure 3.5 is approximately 10^{-5} over 50K, whereas the scale of $LiHoF_4$is 10^{-5} over 1K, and $Tb_2Ti_2O_7$is $3x10^{-5}$ over the same range, and remains at or above this value over the entire temperature range. Especially notable is the minuscule magnitude of the cell effect at low temperatures, approaching 10^{-7} at 2K (seen in the top inset of Figure 3.2). While the thermal expansion of copper was not measured with exceptional accuracy, this uncertainty is a small effect compared to the thermal expansion of materials under study.

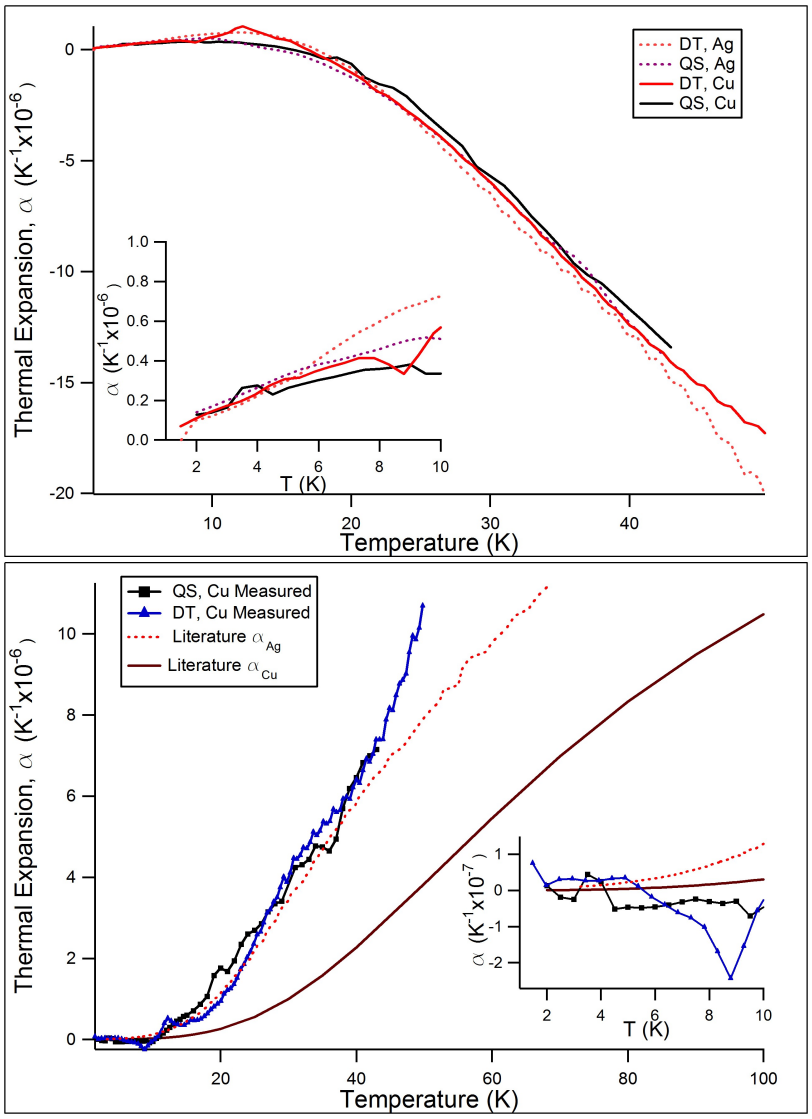

Figure 3.5: Thermal expansion measurements of OFHC copper. Top: Measured response of the dilatometer with a silver sample (cell effect) and the copper sample under question. Top inset: Thermal expansion of cell effect and copper sample below 10K. Bottom: Calculated thermal expansion of OFHC copper from the above measurements. Thermal expansion of silver was taken from [74], and copper from [84] and [82]. Oscillations are due to poor temperature control. DT indicates dynamics temperature control was used, QS indicates quasistatic temperature control was used.

Chapter 4

Dilatometric Study of $LiHoF_4$ In a Transverse Magnetic Field

This chapter discusses the experimental verification of the magnetic field versus temperature (B-T) phase line of $LiHoF_4$ using thermal expansion and magnetostriction techniques. This study was the first performed, using an early version of the dilatometer created for this project. Existing measurements [11] of the phase line of $LiHoF_4$ do not agree with the theoretical expectations [79] based on the transverse field Ising model. This study served to reinvestigate previous experimental measurements, and greatly improve the resolution of critical points in the low-field, high-temperature region of this phase boundary.

4.1 Introduction

Magnetic systems offer an excellent playground to test fundamental theories of matter. Being able to write a Hamiltonian which can (in principle) be solved and describes real materials accurately has allowed thorough quantitative testing these models. There are also numerous experimental techniques which can probe the fundamental properties of magnetic systems, such as neutron scattering, magnetic susceptibility, and thermal expansion. The accessibility of magnetic materials from both an experimental and theoretical footing has allowed for the two approaches to feed back into the other.

Magnetic systems also have the potential to provide significant insight into the study of so-called *quantum phase transitions*. A classical second order phase transition at finite temperature is driven by thermal fluctuations. As the correlation length near the critical point diverges the thermodynamic behavior is determined by regions which are much larger than the length scales on which quantum mechanical fluctuations are important. Thus at finite temperatures a second

order phase transition does not require consideration of quantum fluctuations. A quantum phase transition is driven by quantum fluctuations, and so can occur at zero temperature where thermal fluctuations do not exist. Such quantum phase transitions have been of great interest within the physics community lately [68, 75]. One of the simplest models which predicts a quantum phase transition is the transverse field Ising model [85, 67].

Ising systems have enjoyed continued study since their inception by Ernst Ising [85]. The Ising model is exactly solvable in 1 and 2 dimensions, and numerically solvable in 3 dimensions [54]. There also exist several materials which exhibit nearly ideal Ising behavior [85]. The ground state of an Ising system is one in which the magnetic spins are constrained to lie parallel or antiparallel to a chosen axis. At higher temperatures, thermal fluctuations destroy the order of the ground state and the system becomes a paramagnet. The Hamiltonian of a quantum Ising system is [67]:

$$H = -\sum_{i>j} J_{ij}\sigma_i^z\sigma_j^z \tag{4.1}$$

Where J_{ij} is the coupling between spins and σ_x^z are the Pauli matrices. Quantum mechanical fluctuations can be included in this system by the application of a transverse magnetic, giving the Hamiltonian of the transverse field Ising model.

$$H = -\sum_{i>j} J_{ij}\sigma_i^z\sigma_j^z + \Gamma\sum_i \sigma_i^x \tag{4.2}$$

Where Γ is a control parameter related to the applied magnetic field. If we set $\Gamma = 0$ there are no quantum fluctuations and the system can be understood classically [67, 54]. Quantum mechanical fluctuations can be introduced by allowing $\Gamma \neq 0$, which allows quantum mechanical tunnelling between the eigenstates of σ^z, $|\uparrow\rangle$ and $|\downarrow\rangle$.

An example of Ising behavior is found in $LiHoF_4$, which undergoes a second order paramagnetic to ferromagnetic phase transition at a Curie temperature of 1.53 K [20, 52]. The unit cell of $LiHoF_4$ is shown in Figure 4.1. The quantum spins in $LiHoF_4$ reside on the Ho^{3+} ions, which has a valency of $4f^{10}$. Following Hund's rules, this yields a ground state multiplet $^5I_8$. The Ising constraint is provided by a strongly anisotropic crystalline electric field within the unit cell of $LiHoF_4$, which forces the Ho^{3+} ions to point along the crystallographic c-axis ([001] or easy axis). This anisotropic crystalline electric field splits the low-lying multiplet of Ho^{3+}, creating a ground state doublet ($|\uparrow\rangle$ and $|\downarrow\rangle$) and an excited state ($|\eta\rangle$) some 10 K above [38]. While there has been discussion regarding the exact crystal field parameters [15, 61], the general form of the ground state doublet and the first excited state has been agreed upon since the initial susceptibility measurements performed by Hansen *et al.* [38], given in Equation 4.3. The crystal

field Hamiltonian, H_{cf}, is conveniently expressed in terms of angular momentum operators J_z and $J_\pm$ [38, 15]. The low-energy eigenstates of H_{cf} are expressed in terms of $|m\rangle$, the eigenstates of the J_z operator.

$$\begin{aligned} |\uparrow\rangle &= A|7\rangle + Be^{-\beta i}|3\rangle - Ce^{-\gamma i}|-1\rangle - De^{-\delta i}|-5\rangle \\ |\downarrow\rangle &= A|-7\rangle + Be^{\beta i}|-3\rangle - Ce^{\gamma i}|1\rangle - De^{\delta i}|5\rangle \\ |\eta\rangle &= -Ee^{\epsilon i}|6\rangle - Fe^{\zeta i}|2\rangle - Fe^{-\zeta i}|-2\rangle + Ee^{-\epsilon i}|-6\rangle \end{aligned} \tag{4.3}$$

Where $|\uparrow\rangle$ and $|\downarrow\rangle$ are the (suggestively labelled) degenerate ground states, $|\eta\rangle$ is the excited state and the remaining terms are constants which can be found in References [38, 15]. Note that the $|m\rangle$ states of $|\downarrow\rangle$ are related to the $|m\rangle$ states of $|\uparrow\rangle$ by a sign change. The important feature of the ground states $|\uparrow\rangle$ and $|\downarrow\rangle$ is that they cannot be connected through a linear application of J_x, J_y, J_+, or J_-. More precisely, the matrix elements of these operators vanish within the ground state manifold.

$$\langle\uparrow|J_x|\uparrow\rangle = \langle\uparrow|J_x|\downarrow\rangle = \langle\uparrow|J_y|\uparrow\rangle = \langle\uparrow|J_y|\downarrow\rangle = 0 \tag{4.4}$$

From the above states, we see that at low temperatures where the ground state manifold are the only occupied states, $LiHoF_4$ will behave like an Ising ferromagnet. At finite temperature where the excited state $|\eta\rangle$ is appreciably occupied, $LiHoF_4$ will become a paramagnet. This behavior is a well-understood second order phase transition, driven by thermal fluctuations [67]. The upper critical dimension of the transverse field Ising model and system dimension of $LiHoF_4$ are both 3, leading to measurable logarithmic corrections to the mean-field critical exponents [52].

To fully understand the physics at work in $LiHoF_4$, we should write down a Hamiltonian which represents the system. In addition to a contribution due to the crystalline electric field the important interactions in $LiHoF_4$ are the dipole-dipole interaction, the Heisenberg exchange interaction, and the hyperfine coupling [79, 15]. The dipole-dipole interaction is the effect of the magnetic field of a single Ho^{3+} ion on all other ions, and is inherently a long-range interaction. The Heisenberg exchange interaction is the antiferromagnetic exchange interaction of nearest neighbor Ho^{3+} ions. The hyperfine interaction is due to the interaction of the orbiting electronic moments with the nuclear moment, which in the rare-earth series of elements can be large [53]. Of these three the dipole-dipole interaction will turn out to be the most important, while the Heisenberg interaction is considered to be weak and isotropic and the hyperfine coupling only becomes important near the quantum critical point [79, 15, 11]. This work presented in this thesis is interested in the region of the phase diagram near the zero-field critical point where the hyperfine coupling does not play an appreciable role. These contributions to the $LiHoF_4$ Hamiltonian

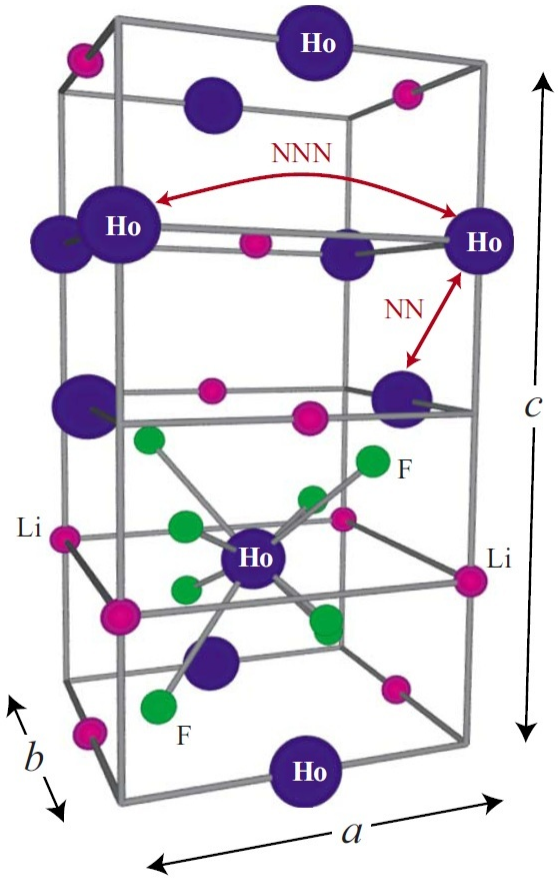

$$a = b = 5.176 \text{ Å}$$

$$c = 10.75 \text{ Å}$$

Figure 4.1: From [79], the unit cell of $LiHoF_4$. $LiHoF_4$ crystallizes into a scheelite lattice. The crystalline electric field constrains the magnetic moment of the Ho^{3+} to point parallel or antiparallel to the crystallographic c-axis.

are [79, 15]:

$$
\begin{aligned}
H_{\text{dipole}} &= \frac{1}{2}(g_{\text{L}}\mu_{\text{B}})^2 \sum_{i\neq j}\sum_{\mu,\nu} L_{ij}^{\mu\nu} J_i^{\mu} J_j^{\nu} \\
\text{Where: } L_{ij}^{\mu\nu}(\mathbf{r}_{ij}) &= \frac{\delta^{\mu\nu} \mid r_{ij} \mid^2 - 3r_{ij}^{\mu} r_{ij}^{\nu}}{\mid r_{ij} \mid^5} \\
H_{\text{Heisenberg}} &= \frac{1}{2} J_{\text{exch}} \sum_{i,NN} \mathbf{J}_i^{\mu} \cdot \mathbf{J}_j^{\nu} \\
H_{\text{Hyperfine}} &= A \sum_i \mathbf{I}_i \cdot \mathbf{J}_j
\end{aligned}
\tag{4.5}
$$

Where g_L is the Landé g-factor, μ_B is the Bohr magneton, $\mathbf{r}_{ij}$ is the vector from position i to j, and A is the hyperfine constant (39 mK for Ho^{3+} [11, 79, 15]), and $\mathbf{I}_i$ is the total angular momentum vector of the Ho^{3+} ion at site i. Assuming that the temperature is low enough that the first excited state is not appreciably occupied and the statement made in Equation 4.4 is true, then the moments within $LiHoF_4$ are strongly Ising-like and we can rewrite these interactions as [79]:

$$
\begin{aligned}
H_{\text{dipole}} &= \frac{1}{2}(g_{\text{L}}\mu_{\text{B}})^2 \sum_{i\neq j} L_{ij}^{zz} J_i^z J_j^z \\
\text{Where: } L_{ij}^{zz} &= \frac{\mid r_{ij} \mid^2 - 3z_{ij}^2}{\mid r_{ij} \mid^5} \\
H_{\text{Heisenberg}} &= \frac{1}{2} J_{\text{exch}} \sum_{i,NN} J_i^z J_j^z \\
H_{\text{HF}} &= A_{\parallel} \sum_i I_i^z J_i^z
\end{aligned}
\tag{4.6}
$$

Quantum effects can be introduced into $LiHoF_4$ by application of a magnetic field transverse to the easy (or Ising) axis, which introduces the Zeeman splitting term into the Hamiltonian, and splits the ground state doublet of $LiHoF_4$. This contribution is:

$$
H_{\text{Zeeman}} = -g_L \mu_B \sum_i \mathbf{H} \cdot \mathbf{J}_i \tag{4.7}
$$

Writing the crystal field effects as H_{cf}, we can now write down a Hamiltonian which is thought to represent $LiHoF_4$ accurately at low temperatures in an applied transverse field as [11,

79, 15]. In the region of the phase diagram being studied in this work the hyperfine interaction is not important, and can be dropped from the expression.

$$
\begin{aligned}
H &= H_{\mathrm{cf}} + H_{\mathrm{dipole}} + H_{\mathrm{Heisenberg}} + H_{\mathrm{HF}} - H_{\mathrm{Zeeman}} \\
H &= \left[H_{\mathrm{cf}} + \frac{1}{2}(g_{\mathrm{L}}\mu_{\mathrm{B}})^2 \sum_{i \neq j} L_{ij}^{zz} J_i^z J_j^z + \frac{1}{2} J_{\mathrm{exch}} \sum_{i,NN} J_i^z J_j^z \right] \\
&\quad - g_L \mu_B \sum_i \mathbf{H}_\perp \cdot \mathbf{J}
\end{aligned} \tag{4.8}
$$

The terms within the square braces will contribute only J^z terms, and contain all the classical physics discussed. The applied transverse field, $\mathbf{H}_\perp$ splits the ground state doublet of the Ho^{3+} ions through the Zeeman interaction, and allows quantum mechanical tunnelling between the Ising states through introduction of a J_x term in the Hamiltonian of $LiHoF_4$. Increasing the magnitude of the applied transverse magnetic field suppresses the Curie temperature of $LiHoF_4$. Ultimately at some critical field H_c this leads to a zero-temperature quantum phase transition [11] where the ferromagnetic order is destroyed. A schematic of this behavior is shown in Figure 4.2. From the arguments presented here, it is evident that $LiHoF_4$ is a good realization of the transverse field Ising model Hamiltonian, presented in Equation 4.2. $\mathbf{H}_\perp$ and Γ are related by projecting $\mathbf{H}_\perp$ onto the subspace being considered — for example, in this discussion $\mathbf{H}_\perp$ would be projected onto the ground state manifold.

4.2 Existing work on $LiHoF_4$

Considerable amounts of attention have been paid to quantum phase transitions within the physics community recently [75]. The transverse field Ising model is among the simplest theoretical models which exhibits such fascinating and topical physics. While the quantum critical regime of $LiHoF_4$ is well described by the transverse-field Ising model [15, 61] there exists a significant discrepancy between the experimentally measured and the theoretically predicted phase line in the predominantly classical regime close to the zero-field transition temperature [79, 15, 61]. An accurate description of the physics in this regime requires a complete understanding of thermal effects on quantum fluctuations. In order to describe quantum fluctuations in real systems at finite temperatures, this may be the most relevant physics [19].

The classical phase transition in $LiHoF_4$ had been identified as early as 1975 in the initial susceptibility measurements by Hansen *et al.* [38] as well as other susceptibility work by Cooke *et al.* [20]. Both of these works identified $LiHoF_4$ as an ideal Ising system, while Hansen *et al.* reported a critical temperature was 1.3 K and Cooke *et al.* reporting the currently accepted

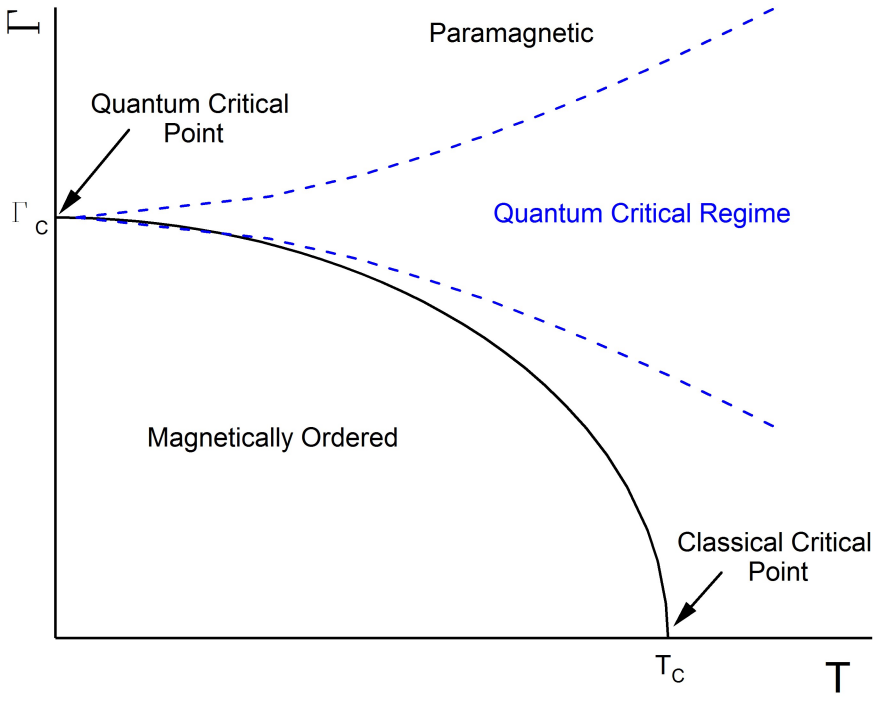

Figure 4.2: A schematic phase diagram of the transverse field Ising model where T is the temperature and Γ is the effective transverse field parameter. The solid line separates the magnetically ordered phase from the paramagnetic phase. The critical points T_c and Γ_c indicate the classical (zero-field) and quantum (zero-temperature) critical points, respectively.

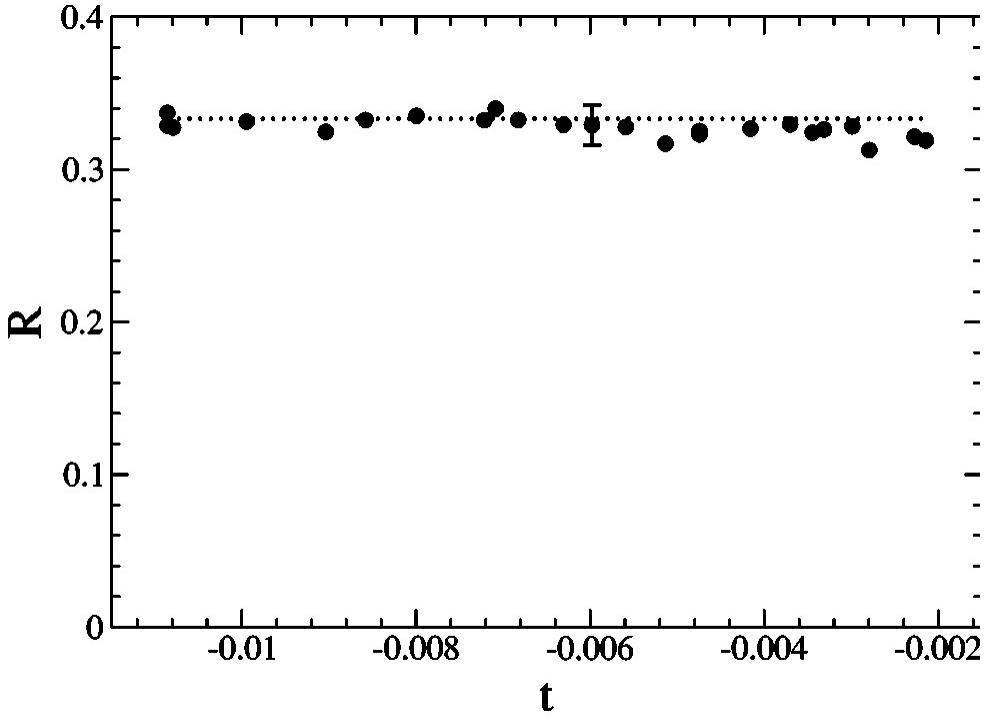

Figure 4.3: From [52], a test of a universal prediction of renormalization group theory as applied to a dipolar Ising ferromagnet, $LiHoF_4$.

1.53 K [11, 52, 62]. More recently, the classical transition has been reinvestigated using high-resolution specific heat capacity by Nikkel *et al.* [52]. Combining previous magnetization [36] and susceptibility [8] measurements, Nikkel *et al.* tested the relationship $R := t^2 C_p \chi T_c / M^2 = \frac{1}{3}$ (where $t = \mid (T - T_c)/T_c \mid$, C_p is the specific heat, χ is the magnetic susceptibility, and M is magnetization) near the critical regime ($t \leq 0.34$), predicted by renormalization group theory [3]. This relationship is a universal relation derived from the renormalization amplitudes, applied to the transverse field Ising model. The results of this test are shown in Figure 4.3, demonstrating excellent agreement between the universal prediction of renormalization group theory and the experimental realization of the dipolar Ising ferromagnet $LiHoF_4$ in the critical region.

Bitko *et al.* were the first to report on the phase line separating the ferromagnetic and paramagnetic states of $LiHoF_4$ in a transverse magnetic field, using magnetic susceptibility measurements [11] shown in the top of Figure 4.4. As can be seen in Figure 4.4, at the critical temperature the real susceptibility $\chi'(T)$ diverges and there is a sharp discontinuity in $\chi''(T)$. The sharp discontinuity in $\chi''(T)$ is due to the onset of ferromagnetic behavior and is used as the identifying feature of the critical temperature. In this thesis, this is interpreted as the first deviation from

the paramagnetic high-temperature behavior of $LiHoF_4$. Bitko *et al.* also presented a mean-field solution of the single-ion Ho^{3+} Hamiltonian self-consistently:

$$H = H_{\text{cf}} - g_{\perp}\mu_B H_{\perp}\hat{J}_x + A(\hat{I}\cdot\hat{J}) - 2J_0\langle\hat{J}_z\rangle\hat{J}_z \tag{4.9}$$

Bitko *et al.* found a solution for Equation 4.9 by fixing $H_{\perp}$, the solving for $\langle\hat{J}_z\rangle$ self-consistently. By decreasing temperature in small steps, a spontaneous magnetization is observed at the critical temperature. Through adjustment of two parameters (the Landé g-factor $g_{\perp}$, and the effective dipole coupling strength, J_0) Bitko *et al.* were able to present a reasonable fit of the data using this mean-field approach. Shown in the bottom of Figure 4.4, two solutions of the Hamiltonian in Equation 4.9 are shown. The dashed line shows the self-consistent mean-solution neglecting the hyperfine interaction (ie: $A = 0$ in Equation 4.9), while the solid line uses a finite hyperfine interaction ($A = 39$ mK). The adjustment of $g_{\perp}$ was later found to be inappropriate for $LiHoF_4$ [15], causing concern regarding the validity of this approach.

Recognizing the possibility for improvement on the theoretical treatment provided by Bitko *et al.*, Chakraborty *et al.* [15] developed a full microscopic Hamiltonian which aimed to capture all of the physics of $LiHoF_4$ as a transverse-field Ising system, in particular the effects of quantum fluctuations and the domain structure of the ferromagnetic state. Beginning from Equation 4.8, Chakraborty *et al.* begin by projecting the J_i operators from the full $(2J+1)(2I+1) = 136$ dimensional Hilbert space to the ground state manifold. This necessitates rescaling all interactions, magnetic field, and temperature but results in a Hamiltonian which is both qualitatively identical and mathematically rigorous. Shown below, it is straightforward to identify the crystal field, the applied transverse field, the dipole-dipole interaction, and the Heisenberg exchange. In the regime near the classical transition, neglecting the hyperfine interaction the Hamiltonian derived is:

$$H_{\text{eff}} = \frac{1}{2}\sum_{i\neq j}\left(\frac{g_{\parallel}\mu_B}{2}\right)^2 L_{ij}^{zz}\sigma_i^z\sigma_j^z + \frac{1}{2}\sum_{i,NN}\left(\frac{g_{\parallel}\mu_B}{2}\right)^2\frac{J_{exch}}{a^3}\sigma_i^z\sigma_{NN}^z - \frac{\Delta(B_x)}{2[\epsilon(B_x)]^2}\sum_i\sigma_i^x \tag{4.10}$$

Where $a = 5.175$ Å is the length of the unit cell of $LiHoF_4$ in the basal plane, and the functions $\epsilon(B_x)$ and $\Delta(B_x)$ rescale the effect of the applied transverse field, brought about by the projection from the full 136 state Hilbert space. All other terms maintain their previous definitions. Results from spectroscopic [18] and susceptibility [38] measurements were used where possible in order to fix any free parameters. The only remaining parameter was the antiferromagnetic Heisenberg exchange coupling J_{exch}, used to explain the overestimation of the quantum

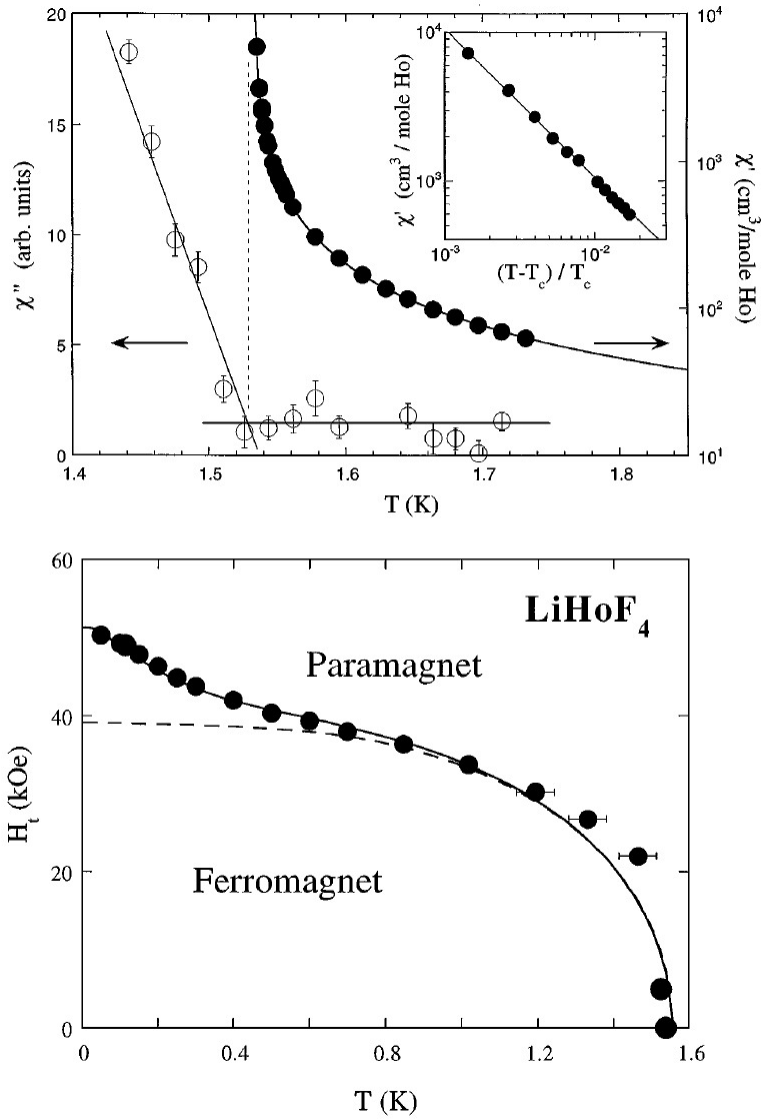

Figure 4.4: From [11], susceptibility measurements of $LiHoF_4$ in the absence of an applied field (top). The filled circles are the real part of magnetic susceptibility, while the open circles are the imaginary part of susceptibility. Inset of top demonstrates the mean field critical behavior of $\chi\prime \propto t^{-\gamma}$, with $\gamma = 1.00 \pm 0.09$. Bottom shows the measured phase line (filled circles) of $LiHoF_4$ in an applied transverse field. The dashed line is a mean field solution of the $LiHoF_4$ Hamiltonian neglecting the hyperfine interaction and the solid line includes the hyperfine interaction. In both fits, the Landé g-factor and effective dipole coupling are used as fitting parameters, see text.

Monte Carlo value calculated from the microscopic Hamiltonian derived [15]. To determine critical points Chakraborty *et al.* used the reaction field method, considering a small sphere inside a larger needle shaped domain within a macroscopic sample. Experimental evidence exists which suggest that needle shaped domains occur in the ferromagnetic state of $LiHoF_4$ [20]. Mean field and quantum Monte Carlo techniques were used to determine a phase line. Critical temperatures were determined by calculating the magnetic susceptibility (χ_{sph}) inside the sphere. Using Equation 4.11, derived in the work by Chakraborty, when the susceptibility reaches its ferromagnetically ordered value of $\chi_{\text{sph}} = 3/4\pi$ Equation 4.11 will diverge. The temperature at which the susceptibility of the sphere diverges is then the critical temperature.

$$\chi = \frac{1}{\chi_{\text{sph}}^{-1} - \frac{4\pi}{3}} \tag{4.11}$$

The mean field approach calculated χ_{sph} approximately, finding a zero-field Curie temperature of $T_c = 2.41$ K and a zero-temperature critical field of $B_c = 4.11$ T. The experimentally determined values of these critical points are $T_c = 1.53$ K and $B_c = 4.9$ T [11]. The nature of a mean field solution disregards fluctuations, so the overestimation of the zero-field Curie temperature is expected. The mean field calculation neglected the hyperfine interaction, which is acknowledged to be important near the quantum critical region in this work. The underestimation of the critical field B_c demonstrates both the inadequacy of a perturbative treatment of the effects of an applied field near the quantum critical point and the necessity of including the hyperfine interaction at temperatures well below the zero-field transition of 1.53 K.

The quantum Monte Carlo treatment calculated χ_{sph} exactly, and treated all spins outside the sphere in a mean-field fashion. This method provided a zero-field Curie temperature of $T_c = 2.03$ K and a critical field $B_c = 3.77$ T. The Heisenberg exchange interaction was used as a tuning parameter in order to match the mean field and quantum Monte Carlo zero-field Curie temperatures with results from experiment [11]. The hyperfine interaction was included using a similar method as that described above, by projecting from the full 136 dimensional Hilbert space to the ground state manifold. These two adjustments improved the overall agreement between the theoretically determined phase line from Chakraborty *et al.*'s work and existing experiments by Bitko *et al.* however a discrepancy remained near the zero-field transition temperature. it was argued that this discrepancy was due to the uncertainties in the crystal-field parameters of $LiHoF_4$.

Rønnow *et al.* [61] presented further theoretical work regarding $LiHoF_4$ as a transverse-field Ising system, addressing primarily neutron scattering spectra [62] and the phase line measured in earlier susceptibility work [11]. This theoretical work derived crystal-field parameters from spectroscopic measurements of Ho-doped $LiYF_4$ [69, 46, 18], which showed good agreement with previous values [38] and with details of electron paramagnetic resonance measure-

ments [46]. Similar to the work of Bitko *et al.* and Chakraborty *et al.*, the hyperfine interaction was included via exact diagonalization of the single-ion Hamiltonian. Using an effective-medium approach and the newly derived crystal field values, Rønnow *et al.* used a Hamiltonian identical to Equation 4.8 to calculate a phase line which agreed well with the work by Chakraborty *et al.* [15]. This suggested that the uncertainty of the crystal-field parameters is most likely not the origin of the overestimation of the phase line of $LiHoF_4$ at low transverse fields.

Most recently Tabei *et al.* [79] presented a significant effort that attempted to reconcile the experimental and theoretical bodies of work. In recognizing that quantum mechanical effects will be small at low transverse fields, Tabei *et al.* introduced these quantum effects perturbatively into a classical Hamiltonian. Using a classical Monte Carlo approach which was simpler and distinct from previous quantum Monte Carlo calculations, Tabei *et al.* separated the possible sources of error into those which were of computational origin, and those which resulted from inadequacies in the model Hamiltonian. Similar to the other work discussed here, Tabei *et al.* began with a complete Hamiltonian of $LiHoF_4$, then projected this Hamiltonian to the ground state manifold to expose the transverse field Ising behavior of $LiHoF_4$. The stated goal of the report by Tabei *et al.* is to investigate the high-temperature region of the $LiHoF_4$ phase diagram, where the fluctuations introduced by the applied magnetic field are small. As such, they write the $LiHoF_4$ Hamiltonian as $H = H_0 - H_1(B)$, where $H_1(B)$ contains the Zeeman interaction and the quantum behavior of $LiHoF_4$. H_0 is the classical Hamiltonian containing the crystal field potential, the dipole-dipole interaction and Heisenberg exchange interaction. The hyperfine interaction is neglected since it does not have an appreciable effect at the high temperatures considered in this work.

Tabei *et al.* then used the perturbative Hamiltonian to perform classical Monte Carlo simulations which compared the effects of the reaction field method versus the Ewald summation method on the calculated phase diagram of $LiHoF_4$. The reaction field method was used by Chakraborty *et al.* [15], described above. Essentially, the reaction field method considers a finite sized volume (a sphere in [15]) inside a macroscopic bulk sample. The macroscopic bulk is treated using a mean field method then the spins inside the small volume react to this external field. The Ewald summation method begins with some simulation volume, then creates periodic copies of the simulated volume. The interactions between the real spins within the original volume can be calculated directly, and the interactions between real spins and virtual spins can be convergently summed over all periodic replicates. Tabei *et al.* used the reaction field method to simulate a sphere inside a long needle shaped domain (as in the work by Chakraborty *et al.*), the Ewald summation method to simulate a needle-shaped sample, and a combination of reaction field and Ewald summation methods to simulate a sphere inside of a long needle shaped sample. As in other theoretical work, the Heisenberg exchange interaction is used as a free parameter to reduce the zero-field critical temperature to that determined in experiment, and was found to vary depending on the method and sample size used in the simulation.

To demonstrate the validity of the perturbative method used they also performed a quantum Monte Carlo simulation using the reaction field method. The results of these simulations are

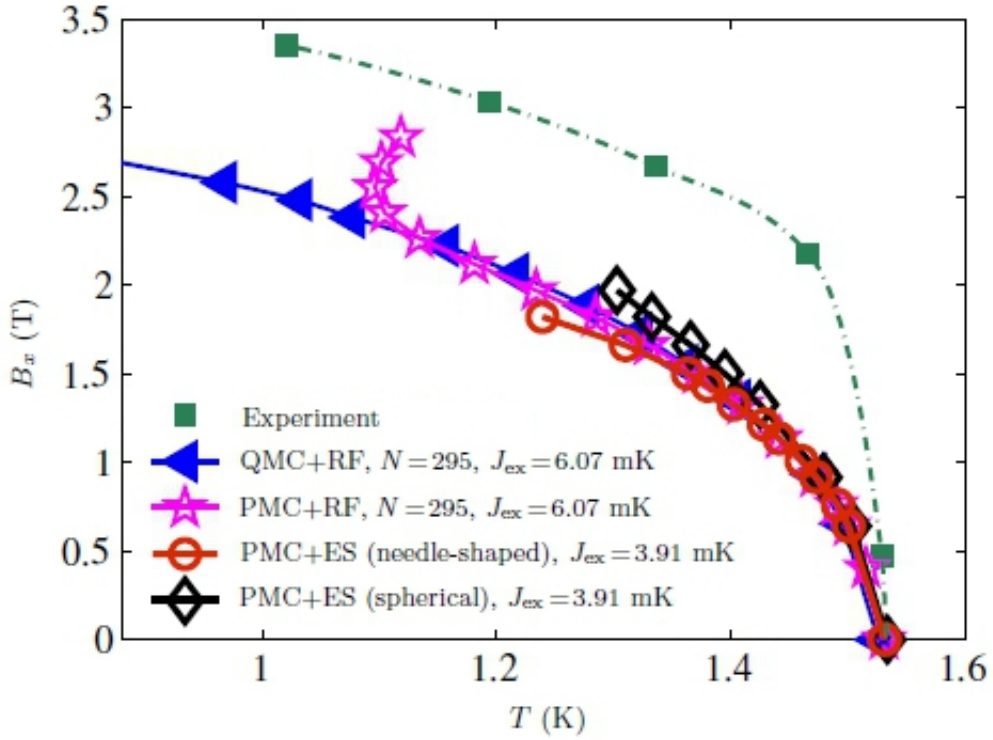

Figure 4.5: Phase diagram of $LiHoF_4$ in a transverse magnetic field determined by Tabei *et al.* [79]. The filled boxes are the experimental critical points determined by Bitko *et al.* [11]. The legend indicates the simulation methods used: QMC represents quantum Monte Carlo, PMC is perturbative Monte Carlo. RF indicates that the reaction field method was used, while ES indicates use of an Ewald summation. The Heisenberg interaction J_{ex} is indicated for each simulation.

shown in Figure 4.5. Tabei *et al.* also used an alternate set of crystal field parameters from Reference [73] to calculate the critical points of $LiHoF_4$ (not shown). This simulation agreed well with the other simulations undertaken in this work. The authors were able to conclude that the discrepancy did not stem from the computational techniques used, or from the uncertainty of the crystal-field parameters. Tabei *et al.* concluded that the source of the discrepancy was most likely due to inadequacies of the model Hamiltonian (Equation 4.2). They also suggested that the experimental determination of the phase line be revisited, providing substantial motivation for the work presented here.

As discussed, there has been a several attempts from the theoretical community [79, 15, 61] to improve the theoretical understanding of $LiHoF_4$. Less experimental effort has been presented to repeat the initial measurements of the phase diagram of $LiHoF_4$. The the rest of this chapter

will discuss a detailed experimental study of the phase line of $LiHoF_4$ using thermal expansion and magnetostrictive measurements. The focus of this study has been on the high temperature, low transverse field regime where previous experimental work [11, 62] has presented the lowest resolution of data, and where the discrepancy between theory and experiment is largest. The remaining portions of this chapter will discuss the experimental technique used, the analysis used to determine critical points, and finally the results of this investigation. The work presented shows good agreement with existing experimental work [11], which suggests that there is further theoretical work to be done.

4.3 Experimental Method

Previous experimental investigations have made use of magnetic susceptibility [11], neutron scattering [62] and specific heat [52] (zero-field only) to determine critical points in the phase diagram of $LiHoF_4$. For the study reported here, capacitive dilatometry has been used to measure the thermal expansion and magnetostriction of a $LiHoF_4$ sample. A detailed description of this device is presented in Chapter 3.

The $LiHoF_4$ sample is taken from a commercially produced single crystal [2] and is shown in Figure 4.6. It is shaped as a roughly semi-circular plate, where the easy axis [001] of $LiHoF_4$ is oriented approximately 25° from the flat edge of the semi-circle. The sample is approximately 1 mm thick, 5.5 mm tall, and about 3.5 mm at its widest point. The easy [001] axis of the $LiHoF_4$ sample was determined to within ±1° using a commercial Laué diffraction setup, and the ends of the crystal subsequently polished to be orthogonal to this easy axis (within ±5°). When placed in the dilatometer, length changes along the [001] axis were measured as temperature and magnetic field were varied.

This experiment made use of the pumped ^{4}He cryostat, which was used to cool the dilatometer to approximately 1 K. The temperature was controlled using a Lakeshore 331 Temperature controller and measured by a calibrated Cernox CX-1030 thermistor located on the cold stage of the pumped ^{4}He cryostat. An experimental trial consists of a temperature sweep through the region of interest (≈ 1.2 K to 1.8 K) at a rate of 7.5 mK/min.

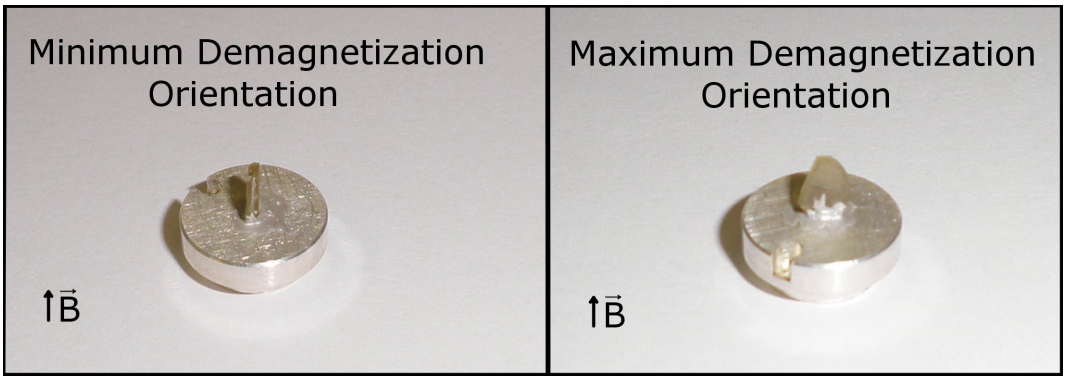

Figure 4.6: Photograph of the $LiHoF_4$ sample mounted on a silver sample holder, showing the minimum (left) and maximum (right) demagnetization orientation if the field is applied roughly into the page. The Ising axis (c-axis) is oriented orthogonal to the surface of the sample holder, the magnetic field is applied perpendicular to the Ising axis.

4.4 Results & Discussion

4.4.1 Thermal Expansion

Zero Field: Figure 4.7 shows the thermal expansion of $LiHoF_4$ without an applied transverse magnetic field. As temperature is lowered, the transition from the high temperature paramagnetic state to the low temperature ferromagnetic state shows a sudden jump in thermal expansion coefficient, typical of a second order phase transition. The critical temperature, T_c, is defined as the first deviation from paramagnetic behavior as temperature is reduced to be consistent with previous experimental [11] and theoretical [15] work. This critical point was determined from the intersection of a quadratic fit of the high-temperature paramagnetic behavior and a linear fit of the steepest section of the thermal expansion coefficient, similar to that shown in Figure 4.8. Increasing the order of either fit made no appreciable difference in T_c. The uncertainty of this analysis was determined by varying the range of the fitted curve by up to ± 0.05 K, 10% of the temperature range, and observing the range of resultant critical temperatures. A plot of these critical temperatures is shown in the lower plot of Figure 4.8.

Applying the analysis shown in Figure 4.8 to the zero-field data yields a transition temperature of $T_c = 1.532 \pm 0.005$ K. The inset of Figure 4.7 shows high resolution specific heat data [52] plotted with the thermal expansion coefficient. As discussed in Chapter 3, we can relate specific heat (C_v) and the thermal expansion coefficient using the Grüneisen parameter (γ) and the bulk modulus (B): $\alpha(T) = (\gamma/3B)\, C_v(T)$. If we assume that the Grüneisen parameter and the bulk modulus are roughly temperature independent, then discontinuities in the specific heat data should be reproduced in thermal expansion data. The inset of Figure 4.7 shows this comparison:

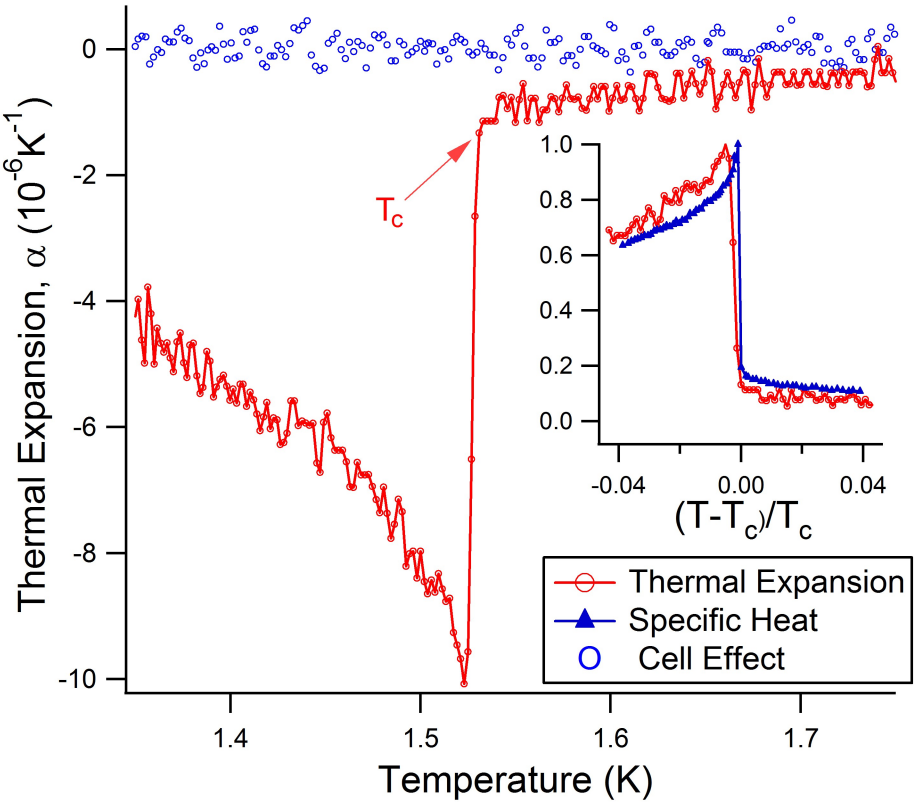

Figure 4.7: Zero-field measurement of the thermal expansion coefficient, α, of $LiHoF_4$ and the cell effect as a function of temperature. The critical temperature, T_c is indicated, being the first deviation from the paramagnetic state. Inset: Normalized thermal expansion coefficient and specific heat measurements [52] as a function of reduced temperature.

both specific heat and thermal expansion data are normalized to their peak value, and plotted against reduced temperature with respect to their individual transition temperatures. The thermal expansion measurement has also been inverted. Qualitative agreement between the two measurements is excellent. Quantitatively, there is a small discrepancy between absolute transition temperatures (1.532 ± 0.005 K and 1.5384 K for thermal expansion and specific heat respectively) and the width of the critical region is larger by 4.4 mK in the thermal expansion measurement. These effects can be attributed to the dynamic temperature control method used to gather the thermal expansion data.

Another effect of the dynamic temperature control used is a shift in the observed critical temperature. As the temperature is swept at a higher rate a larger thermal gradient forms between the thermistor used to measure temperature and the sample. This leads to a measurable shift in the critical temperature. By comparing critical points determined from experimental trials which swept temperature at different rates we can quantify this shift. This analysis is shown in Figure 4.9. The inverse reduced temperature (defined in the caption) is plotted versus the rate of change of temperature, using the critical temperature from Nikkel and Ellman's work [52] to calculate the reduced temperature.

Transverse Magnetic Field: The thermal expansion of $LiHoF_4$ in applied transverse fields is shown in Figures 4.10 and 4.11, showing the evolution of the critical region as the strength of the applied transverse field is increased. In both figures, curves have been offset for clarity. There are three noteworthy qualitative features in these data sets. First, the thermal expansion in the ferromagnetic phase is concave downwards in zero field and low applied field, changing to concave upwards above 1 T. Secondly, the gradient of thermal expansion is small and positive at zero field, changing to a slightly larger negative gradient at an applied transverse field of 1 T, returning to a small positive gradient by 2 T. In order to accommodate these variations in thermal expansion, the critical region evolves from a step downward entering the ferromagnetic state at 0 T to a step upwards at fields of 1 T and larger. The width of the critical region broadens significantly as field is increased. This broadening can be understood as moving across the phase line of $LiHoF_4$ at differing angles of incidence in the B-T phase space.

Identical analysis as shown in Figure 4.8 has been carried out on each of the curves at finite applied fields. As such, the transition temperature has been defined as the deviation from the monotonic behavior considered to be the paramagnetic phase. As the critical region broadens the uncertainty (calculated as shown in Figure 4.8) in the transition temperature increases.

Small Transverse Field: The uncertainty of the critical points in Figure 4.10 would allow for a reentrant phase line. A reentrant phase line would be manifest by moving along an isotherm just above the zero-field critical temperature and increasing the applied field. $LiHoF_4$ would begin in the paramagnetic state, then undergo a phase transition to a ferromagnet, then back to a paramagnet. This behavior is not predicted from the transverse field Ising model, and indeed evidence of a reentrant critical region would demonstrate clearly that the theoretical treatment of $LiHoF_4$ has been missing some aspect of the physics at work in this system. To confirm or deny

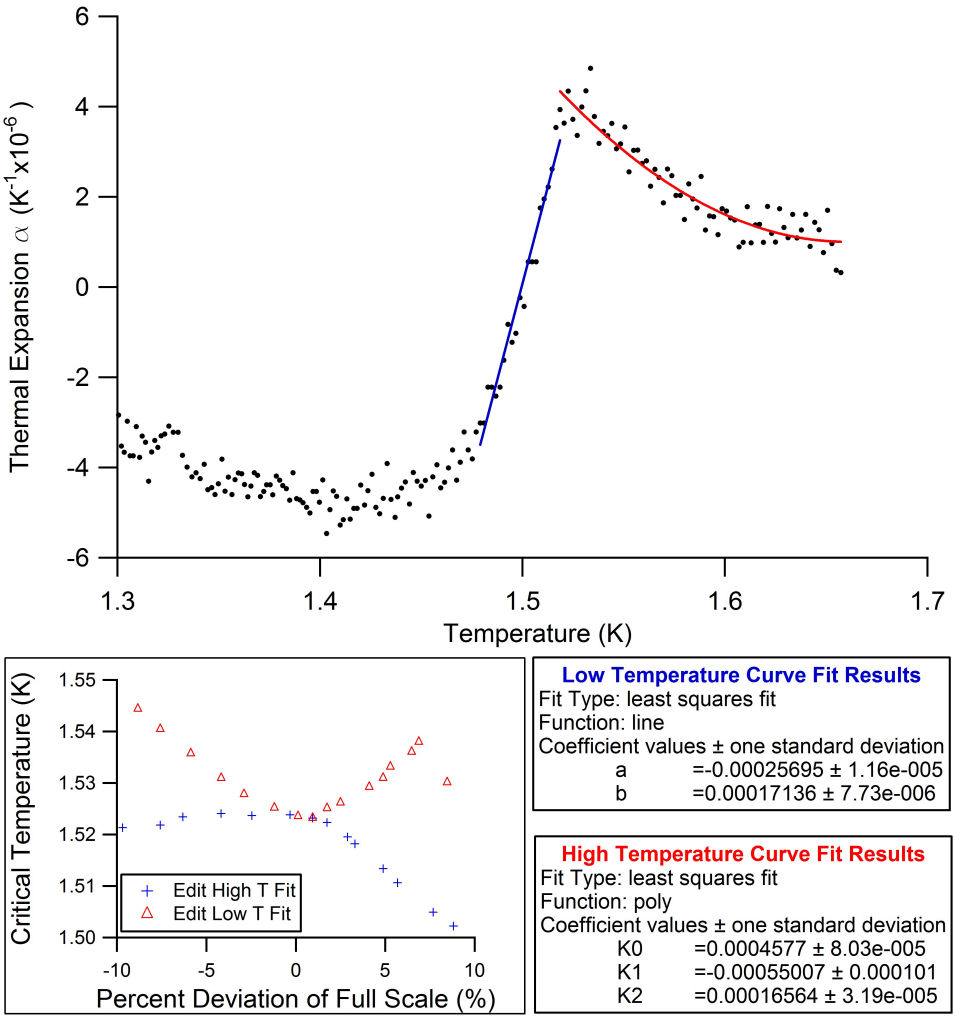

Figure 4.8: Example of the analysis used to determine T_c from thermal expansion measurements on $LiHoF_4$, shown for thermal expansion in an applied field of 1 T. Top: Fitting curves used. The right most blue curve is a quadratic fit of the high-temperature paramagnetic region, while the central red curve is a linear fit of the steepest section of the curve. The intersection of these two curves is T_c. Bottom: Determination of error bounds of T_c, determined by varying the range of the fitted curves up to 10 % of the domain, ±0.005 K. The range of this plot is the uncertainty of T_c.

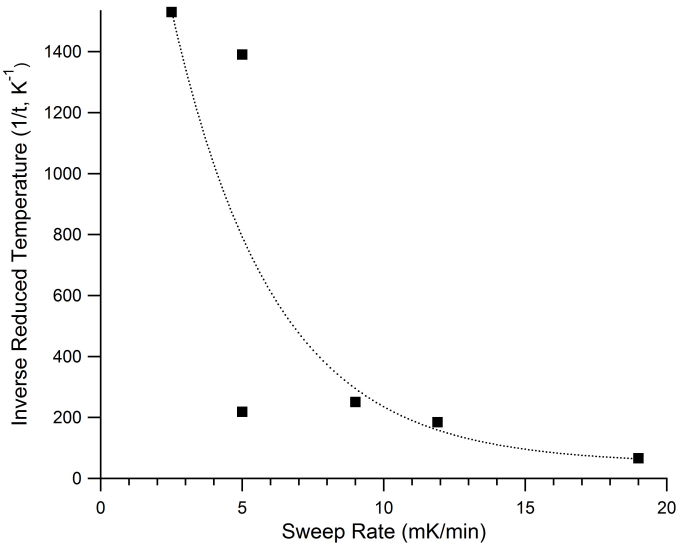

Figure 4.9: The effect of varying the sweep rate on the observed critical temperature of $LiHoF_4$. The reduced critical temperature $t = \frac{|T-T_c|}{T_c}$ was calculated using the critical point from Nikkel and Ellman's high resolution specific heat work [52].

this possibility, the thermal expansion at low transverse fields was investigated. These results are shown in Figure 4.12.

The data gathered in Figure 4.12 made use of a different calibrated CX-1030 thermistor, which had a significantly smaller magnetoresistance correction than the thermistor used to gather the data presented in Figures 4.10 and 4.11 [12]. The magnetoresistance correction applied to temperature made use of the scheme presented in Reference [12]. The $LiHoF_4$ sample was oriented in the minimum demagnetization orientation. The spring used for this investigation was a factor of 10 softer than previously, and a design with allowed much greater horizontal deflection than in the earlier $LiHoF_4$ work. The horizontal flexibility of the spring allows significantly greater torque effects than the spring used in the earlier $LiHoF_4$ work. The author believes that the changed orientation and the softer spring is the cause of the different qualitative behavior of the critical region, however there were no thermal expansion measurements done in a negative applied field to confirm this. In this orientation, the critical point was chosen as the minimum point of the thermal expansion curve. This agrees more closely with the discontinuity expected (as discussed in Chapter 2) and from the relationship ($\alpha = \gamma C_v$) to specific heat. As seen in Figure 4.12, there is no evidence of a reentrant phase line in this investigation. The convolution of torque effects and a changed sample orientation leave some doubt as to the veracity of this statement.

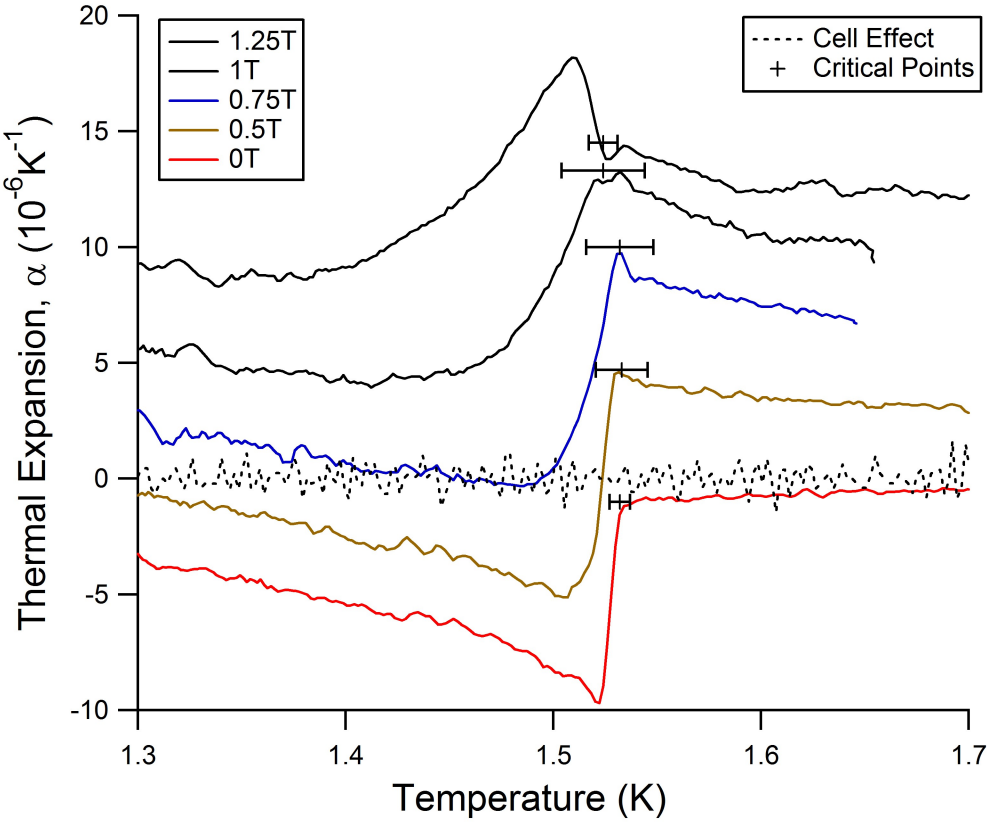

Figure 4.10: Measurement of the thermal expansion coefficient, α, for $LiHoF_4$ up to an applied transverse field of 1.25 T. The critical temperature at each field is indicated, determined as the first deviation from the paramagnetic high-temperature behavior. The curves at different field strengths are offset by $3 \cdot 10^{-6}$ per curve.

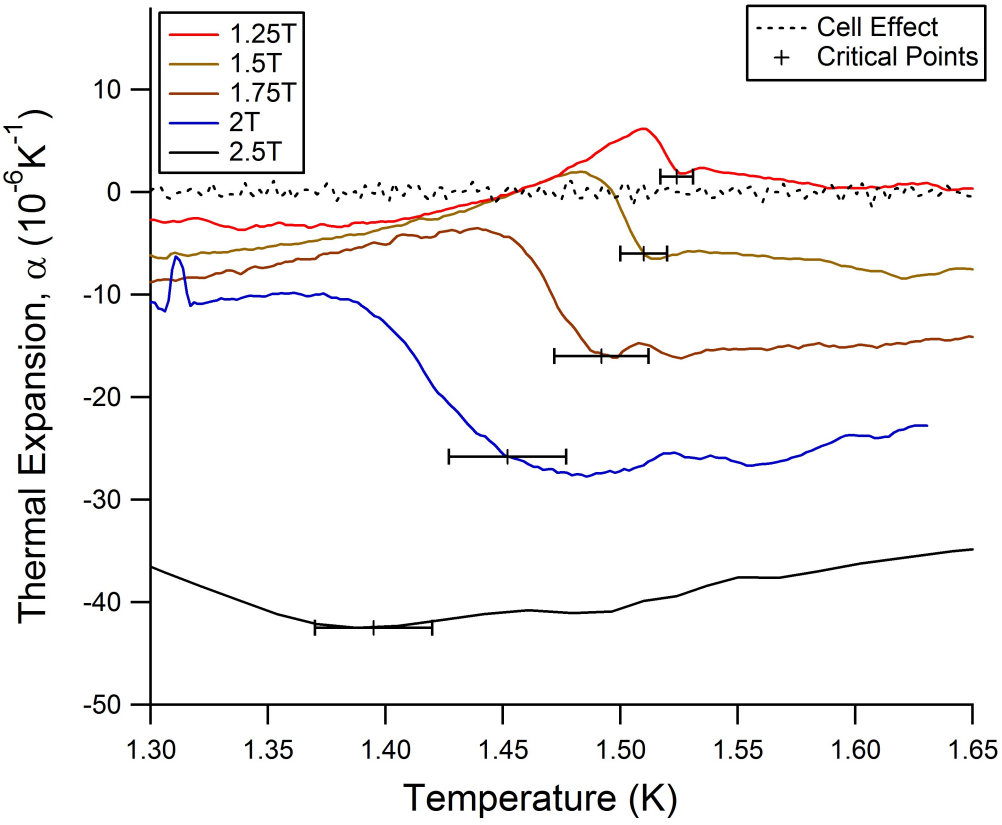

Figure 4.11: Measurement of the thermal expansion coefficient, α, for $LiHoF_4$, from 1.25 T to 2.75 T. The critical temperature at each field is indicated, determined as the first deviation from the paramagnetic high-temperature behavior. The curves at different fields are offset by $-5 \cdot 10^{-6}$ per curve.

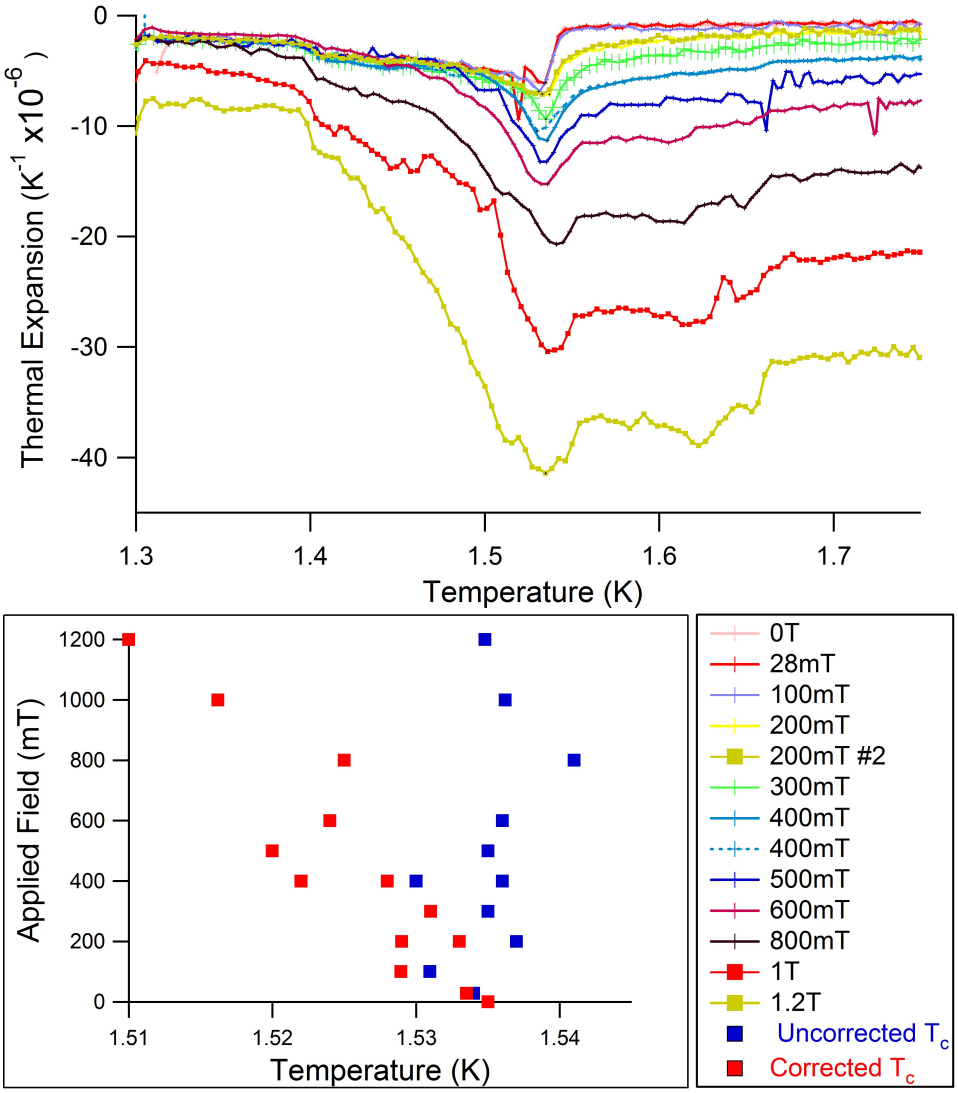

Figure 4.12: Top: Measurement of the thermal expansion coefficient, α, for $LiHoF_4$, from 0 T to 1.25 T. This measurement was performed in the minimum demagnetization orientation. Curves have not been offset. Bottom: Critical points, and the correspondingly corrected critical points to account for the magnetoresistance of the CX-1030 thermistor used. Uncertainty was determined by the difference of repeated measurements (ie: the separation of points at 400 mT) to be ±6 mK and are not shown for clarity.

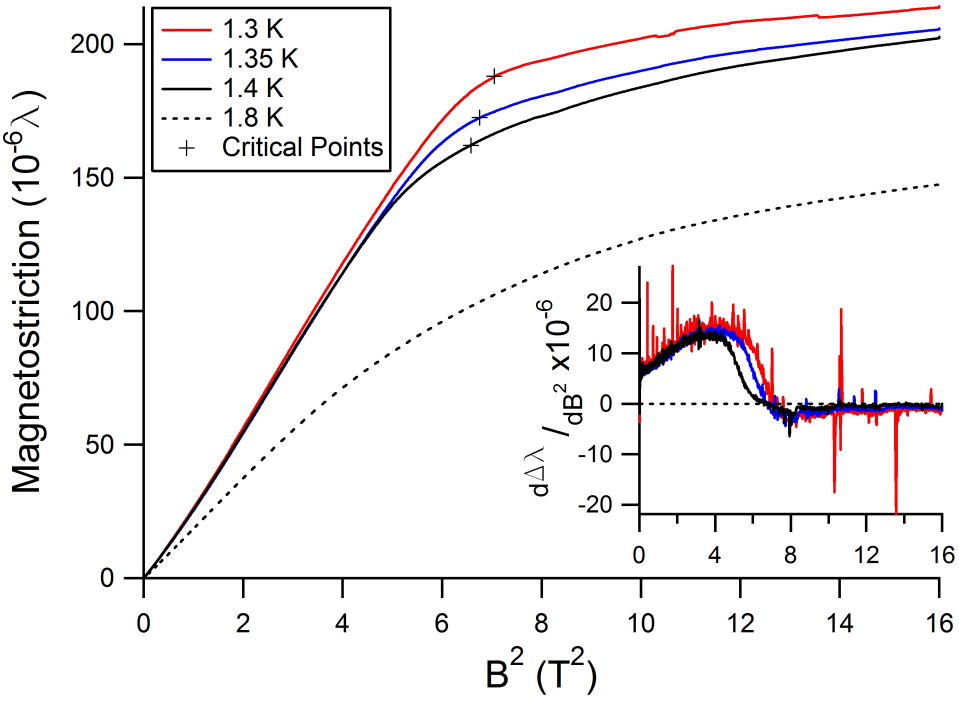

Figure 4.13: Magnetostriction, $\lambda = \frac{\Delta L}{L}$, as a function of transverse field squared, B^2 measurements performed on $LiHoF_4$, in the minimum demagnetization orientation. Inset: $\frac{d\Delta\lambda}{dB^2}$ as a function of B^2. The critical field is the determined when the derivative equals zero.

4.4.2 Magnetostriction

The change in length of a material in response to an applied magnetic field is defined as the magnetostriction, $\lambda = \Delta L/L$. Figure 4.13 shows the magnetostriction of $LiHoF_4$ measured at T = 1.3, 1.35, 1.4 and 1.8 K plotted versus the square of the applied transverse field, B^2. The magnetostriction of $LiHoF_4$ at 1.8 K is entirely within the paramagnetic region, so subtracting this from the lower-temperature response curve (call this $\Delta\lambda = \lambda_T - \lambda_{1.8K}$) we expose the magnetic response of $LiHoF_4$ more clearly. The raw magnetostrictive response $\Delta\lambda$ does not show a sharp feature as was observed in the thermal expansion measurement, however the first derivative of $\Delta\lambda$ with respect to applied field shows a distinct change in behavior which is interpreted as the onset of the paramagnetic state as field is increased. The critical field is therefore determined as the point at which the first derivative equals zero. This derivative ($d\Delta\lambda/dB$) is plotted in the inset of Figure 4.13. The uncertainty of this critical point is dominated by the uncertainty of the magnetoresistance of the thermistor used to control the temperature.

4.4.3 Demagnetization Effects

Due to the irregular shape of the $LiHoF_4$ sample used in this study, an accurate calculation of the demagnetization factor due to uncompensated spins on the surface of the sample is difficult. However, it is still possible to assess the impact of demagnetization effects on the results presented here by orienting either the semi-circular face or the thin edge perpendicular to the applied transverse field. The semi-circular face of the crystal perpendicular to the applied field represents the maximum demagnetization orientation, while orienting the thin edge of the crystal perpendicular to the applied field represents the minimum demagnetization orientation. Following is an estimate of the magnitude of the difference of the demagnetization factor between these two orientations.

The demagnetization correction can be written as $H_{\text{Internal}} = H_{\text{Applied}} - GM$, where H is either the internal or applied magnetic field, G is the geometric factor resulting from the crystal geometry, and M is the sample magnetization. As a first approximation, we can assume that the difference between H_{Internal} and H_{Applied} of each orientation will be determined by G, if the only experimental change is the orientation of the sample and the magnetization is assumed to be the same. A scheme for the magnetostatic mapping of shapes to their equivalent ellipsoid has been proposed by Beleggia *et al.* [9], for which the calculation of the demagnetization factor is greatly simplified. Following Beleggia *et al.*, we can estimate the demagnetization factors of the $LiHoF_4$ sample used in this work by a rectangular prism with dimensions L_x = 1 mm, L_y = 2.1 mm, and L_z = 5.5 mm.

Making use of the Mathematica code provided in Beleggia *et al.*'s work, the demagnetization factors have been found to be $G_x = G_{\text{max}} = 7.55$, $G_y = G_{\text{min}} = 1.68$, and $G_z = -0.32$. The demagnetization correction in the maximum demagnetization orientation will therefore be approximately 4.5 times larger than in the minimum demagnetization orientation. Through repeating the same experiments using each of the maximum and minimum demagnetization orientations, we can compare the effects of demagnetization in each orientation. As expected, the critical temperature in zero applied field for both orientations is identical and occurs at $T_c = 1.532 \pm 0.005$ K.

The results of such an investigation are shown in Figure 4.14, for an applied field of H = 2.5 T. The most obvious feature apparent in these tests is the qualitative difference in the temperature dependence of the thermal expansion coefficient between each orientation. The critical temperatures extracted for each case are shown by crosses in Figure 4.14, and are $T_c(\text{max}) = 1.35 \pm 0.03$ K and $T_c(\text{min}) = 1.37 \pm 0.03$ K. Despite a demagnetization correction approximately 4.5 times larger in the maximum demagnetization orientation, there is a small difference in the critical temperature extracted from the thermal expansion measurements. Thus, the demagnetization correction will lead to changes in T_c that are (at most) within current uncertainty estimates.

The analysis above assumed that the sample forms a single domain. The presence of multiple domains makes calculation of the demagnetisation factor far more complicated [51, 24]. Even with a magnetic domain structure, we would expect some orientation dependence of the

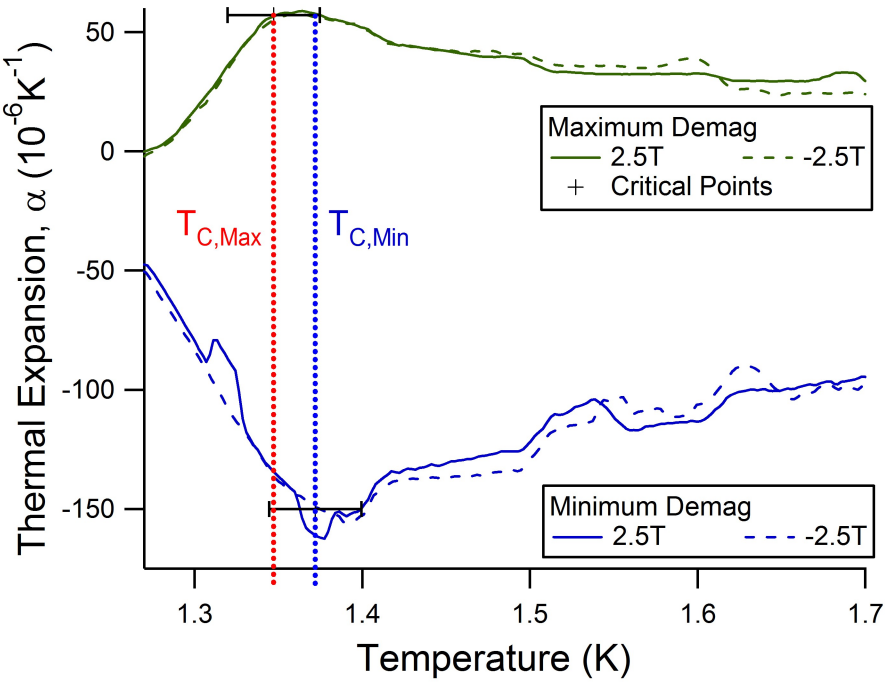

Figure 4.14: Measurement of α for $LiHoF_4$ at ± 2.5 T in the maximum (solid lines) and minimum (dashed lines) demagnetization orientations. Crosses show the calculated critical temperatures. The red (blue) dotted line indicates the critical temperature determined from the maximum (minimum) demagnetization orientation, identical within error.

demagnetization factor for the sample used. The empirical evidence from this study shows that this correction is small. Biltmo and Henelius have presented a theoretical analysis of the domain structure in $LiHoF_4$ [10]. Our speculation is that the orientation dependence of the domain structure may explain the observed qualitative differences in the thermal expansion. Lacking a better understanding of the microscopic origin of the thermal expansion coefficient and domain structure in the critical region, it is not reasonable to present conjecture on the origin of this observation.

4.4.4 Torque Effects

If the sample were to be slightly misaligned within the transverse magnetic field, it may lead to a torque on the sample which may rotate or bend the sample *in situ*. This rotation or bending could lead to a signal indistinguishable from thermal expansion or magnetostriction. To verify that such an effect was not distorting our ability to accurately measure the phase transition of $LiHoF_4$, the thermal expansion was measured in positive and negative applied field in the minimum and maximum demagnetization orientations.

The results of this investigation are shown in Figure 4.14. The thermal expansion in either field direction is identical, leading to the conclusion that there is no significant rotation or bending of the sample due to any putative torque. This conclusion is also consistent with a small sample magnetic moment due to magnetic domains.

4.5 Discussion & Conclusions

Collecting the critical points determined from thermal expansion and magnetostrictive measurements produces the phase diagram shown in Figure 4.15. The broadening of the error bars as the critical field increases reflects the broadening of the critical region and the increased difficulty in assigning a critical point rather than an intrinsic loss of precision in the measurement technique used. The critical points from earlier magnetic susceptibility work by Bitko *et al.* [11], neutron scattering by Rønnow *et al.* [62], and the latest numerical simulation by Tabei *et al.* [79] are also plotted on Figure 4.15. The agreement between experimental data from this study and the magnetic susceptibility work by Bitko *et al.* is excellent, thereby confirming the discrepancy with the current theoretical simulations. In a qualitative sense, what occurs is that the critical temperature of $LiHoF_4$ is initially insensitive to the applied field. Once the field is stronger than approximately 1 T (approximately 25% of the field required to completely suppress the ferromagnetic behavior at zero temperature) the transition temperature begins to be suppressed. This initial insensitivity to the applied transverse field is unknown and does not appear to be realized in the transverse field Ising model (Equation 4.2 which is used to describe $LiHoF_4$ [79, 61, 15]. The important issue to address now is whether this is due to the simplified nature of the transverse

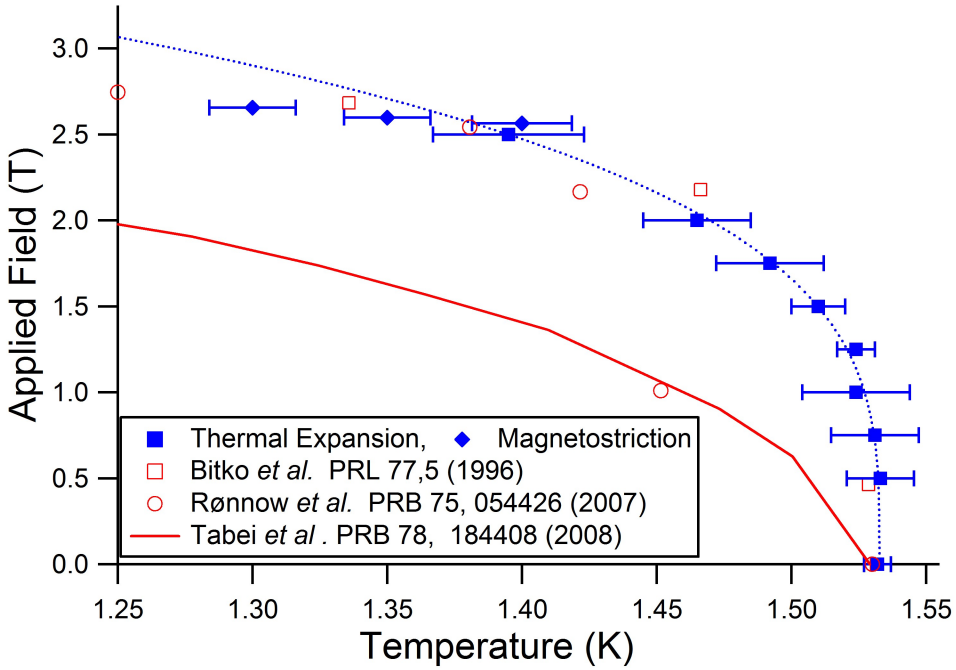

Figure 4.15: Transverse field versus temperature phase diagram of $LiHoF_4$, as measured by this study using thermal expansion (squares) and magnetostriction (circles) data. Also plotted is previous experimental [11, 62] and theoretical Monte Carlo [79] work. (Dotted line is a guide to the eye.)

field Ising model as applied to $LiHoF_4$, or if this reveals a more generic lack of understanding of the impact of quantum fluctuations at finite temperatures.

Earlier theoretical work has suggested that one physical aspect unique to $LiHoF_4$ is the effect of magnetoelastic coupling on the antiferromagnetic or quadrupolar exchange parameters [61, 79]. In principle, the competition between these couplings and the ferromagnetic coupling could affect the transition temperature. Rønnow *et al.* [61] estimated that a strain, $\epsilon_{13} \sim 10^{-4}$ would be required to produce a noticeable effect in the transition temperature due to the quadrupolar interactions. The measurements of magnetostriction presented here are along the c-axis, and are of overall magnitude $\lambda \sim 10^{-6}$. Unless the magnitude of in-plane magnetostriction is larger by approximately 2 orders of magnitude or more, the in-plane magnetostriction would likely not compensate for the effects of quantum fluctuations. To provide a more complete picture, measurements of magnetostriction along the a-axis would be required. Investigation of the qualitative behavior of magnetostriction very close to $T_c(0)$ would be informative.

A qualitative change in the behavior of the thermal expansion near the critical region has been

observed near the field scale of 1 T, shown in Figures 4.10, and 4.11. A detailed microscopic theory describing the origin of the features observed would be necessary to assess whether this phenomenon is related or coincidental. As discussed, experimental work to complement existing theoretical descriptions of the motion of domain walls [10] would be illuminating. Further observation of the critical region using any other experimental probe could also provide additional insight.

Finally, invaluable insight may be gained from identifying whether the discrepancy observed in $LiHoF_4$ is particular to this system, or is a more general feature. Investigation of $Ho(OH)_3$ and $Dy(OH)_3$ as proposed by Stasiak *et al.* could indicate whether the discrepancy which exists between theoretical and experimental work is unique to $LiHoF_4$, or is a generic feature of the transverse field Ising model in real systems[77].

In conclusion, the phase diagram of $LiHoF_4$ in an applied transverse field has been mapped using thermal expansion and magnetostriction measurements. This study has focussed on the low-field regime close to the zero-field phase transition where the effect of quantum fluctuations is small. The observed phase line separating the low-temperature ferromagnetic phase from the high-temperature paramagnetic phase agrees well with existing experimental reports [11] and disagrees with current theoretical work based on the transverse field Ising model [15, 79]. The important issue to address is whether this disagreement is due to some subtlety of $LiHoF_4$ or whether it is a more generic feature demonstrating a lack of understanding of the effect of quantum fluctuations at finite temperatures.

Chapter 5

Dilatometric Study of $Tb_2Ti_2O_7$ in an Applied Longitudinal and Transverse Fields

This chapter discusses a dilatometric investigation of $Tb_2Ti_2O_7$. Unlike $LiHoF_4$, $Tb_2Ti_2O_7$ does not order down to 50 mK [31] and the physics at work is not well understood. This chapter begins with a brief summary of the existing work on $Tb_2Ti_2O_7$, attempting only to describe the state of affairs as they stand at the time of writing. Following this description preliminary experimental work on $Tb_2Ti_2O_7$ is presented, and future avenues of investigation are outlined.

5.1 Introduction

In the case of $LiHoF_4$ an ordered-to-disordered transition was observed, where the symmetry of the high-temperature disordered state was broken to form the ordered low-temperature Ising ferromagnetic phase. A natural question is to ask is whether this type of well-ordered ground state is universal: do all materials possess an ordered ground state? While it is initially tempting to state that the ground state of a system must be a pure state of zero entropy, we can construct an ideal system which does not order.

To create a disordered ground state, we must focus on the pairwise interactions and introduce the idea of frustration. Frustration arises when all the interactions in a system cannot be simultaneously satisfied. A simple example occurs if we place nearest-neighbor antiferromagnetically coupled Ising spins on the corners of a equilateral triangle, as shown in the top of Figure 5.1. For any combination of spins there is at least 1 bond which cannot be satisfied. If we then create a 2 dimensional triangular lattice of these spins the ground state will be frustrated, creating a

macroscopic number of degenerate states which may be inhabited. We can extend this idea to 3 dimensions if we place nearest-neighbor antiferromagnetically coupled Heisenberg spins on the corners of a tetrahedra to come to a similarly macroscopically degenerate ground state [80]. An illustration of this is also shown in Figure 5.1 The inability to satisfy all interactions due to the geometry of a system is known as *geometric frustration*.

A physical realization of this *geometric frustration* is found in the magnetic pyrochlore oxides, materials of the form $RE_2TM_2O_7$. RE is a rare earth ion and TM is a transition metal. The pyrochlore lattice consists of two interpenetrating sublattices of corner-sharing tetrahedra, where the rare-earth ions reside on one sublattice and the transition metals on the other. Figure 5.1 shows a magnetic sublattice, where magnetic spins obey a local Ising constraint (pointing towards or away from the center of a tetrahedra) with antiferromagnetic interactions. Figure 5.1 shows the magnetic spins obeying the "two-in two-out" spin-ice rules. The thick grey line of Figure 5.1 is an excitation loop - flipping all spins on this line leads to degenerate spin-ice state. Populating one or both of these sublattices with Heisenberg spins with nearest-neighbor antiferromagnetic spins gives rise to a highly frustrated ground state[32].

Study of these pyrochlore oxides has provided an abundance of novel physics at low temperatures. The review by Gardner *et al.* [32] presents a summary of this large body of work. In several cases, subtle effects destroy the degeneracy of the ground state to create a long-ranged ordered ground state. In other cases the dynamics become very slow at low temperature and the spins remain randomly oriented, leaving the spins disordered and frustrated. This behavior is termed a *spin glass*. Another ground state configuration occurs when the spins freeze in place, known as a *spin ice* for its relationship with the Pauling ice rules (ie: a divergence free structural unit) and the recovery of $(Nk_B/2)\ln(3/2)$ residual entropy at the lowest temperatures studied [32, 55]. A third disordered state predicted is the *spin liquid* or *cooperative paramagnetic* phase, where spins remain dynamic and disordered to the lowest temperatures studied. $Tb_2Ti_2O_7$ is a candidate spin liquid, and will be the focus of the discussion presented in the remainder of this chapter.

5.1.1 Existing work on $Tb_2Ti_2O_7$

The body of work on the magnetic pyrochlore oxides is significant, and no attempt is made here to present a complete review of literature available. The interested reader is directed to the review by Gardner *et al.* [32]. This section will discuss a subset of the experimental and theoretical work which exists on $Tb_2Ti_2O_7$ in order to illuminate the difficulty in describing the underlying physics of $Tb_2Ti_2O_7$. As of this writing there has not been a description of the physics of $Tb_2Ti_2O_7$which reproduces all experimental observations.

Anti-ferromagnetic coupling of Heisenberg [80] spins or ferromagnetically coupled local Ising spins [5, 39] on a pyrochlore lattice have been predicted to lack long range order at finite temperature. Magnetic susceptibility measurements of $Tb_2Ti_2O_7$ indicate a Curie-Weiss temperature of $\theta_{cw} = -19$ K, implying antiferromagnetic coupling [35] in $Tb_2Ti_2O_7$. Muon spin

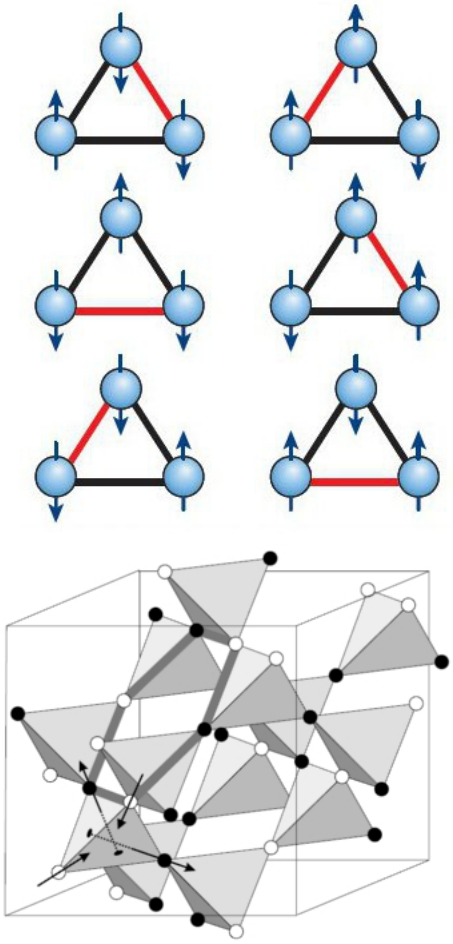

Figure 5.1: Top: A simple example of frustration in 2 dimensions. Ising spins with antiferromagnetic coupling are placed on an equilateral triangle. One of these bonds can never be satisfied (shown in red), leaving the system in a frustrated state. The 6 different states shown are degenerate. In the thermodynamic limit for a system of a large number of spins this frustration leads to a macroscopic number of potential ground states. Bottom: The pyrochlore lattice from [34], a 3-dimensional analogue of the 2-D triangular lattice. Dots indicate the location of spins: black dots indicate a spin pointing out of a downward tetrahedra, white dots indicate a spin pointing into a downward tetrahedra. In this diagram spins are antiferromagnetically coupled and obey a local Ising constraint; the state shown obeys the "two-in two-out" spin ice rules, and the thick grey line indicates an excitation loop. Flipping all spins on the loop results in a degenerate spin-ice ground state. Notice this lattice is frustrated — the two white spins shown are connected by one vertex of a tetrahedra and are not antiferromagnetic coupling.

relaxation and neutron scattering measurements have shown that $Tb_2Ti_2O_7$ remains disordered to 50 mK [31, 28, 42]. Presenting a microscopic theory which is consistent with experimental results has proven challenging, apparent from 20 years of study without resolution.

As in the discussion of $LiHoF_4$ presented in Chapter 4, we begin the discussion of $Tb_2Ti_2O_7$ by examining the low-lying energy states of the Tb^{3+} ions and the dominant interactions in $Tb_2Ti_2O_7$. The valency of Tb^{3+} is $4f^8$, providing a ground state of $^7F_6$. The free-ion moment would be expected to be $9.72\mu_B$, however dc susceptibility measurements and polarized neutron scattering measurements indicate the it is in fact much smaller [35, 13]. The crystalline electric field splits the degeneracy of the $(2J+1) = 13$ low-lying states of Tb^{3+} [35, 47]. The first excited state of $Tb_2Ti_2O_7$ is 19 K above the ground state, the second excited state at 87 K, and the third at 120 K. The ground state and first excited state were found to be doublets, shown below in Equation 5.1 [35].

$$\begin{aligned} |\pm\rangle &= -0.97|\pm 4\rangle \pm 0.14|\pm 1\rangle \mp 0.13|\mp 5\rangle \\ |E_\pm\rangle &= -0.91|\pm 5\rangle \pm 0.28|\pm 2\rangle \mp 0.14|\mp 4\rangle \end{aligned} \tag{5.1}$$

Where $|\pm\rangle$ is the ground state, and $|E_\pm\rangle$ is the first excited state at 19 K. Mirebeau *et al.* presented inelastic neutron scattering results in 2007, from which they calculated crystalline electric field parameters which agree well with the above energy states [47]. These parameters accurately reproduced the neutron scattering spectra observed, as well as previous susceptibility and magnetization measurements. Chapuis *et al.* [17] have recently reported evidence of a singlet ground state in $Tb_2Ti_2O_7$ and the related compound $Tb_2Sn_2O_7$, presenting a competing model of the low energy structure of $Tb_2Ti_2O_7$. The low energy manifold thus remains an open question.

In the case of $Tb_2Ti_2O_7$, the crystalline electric field aligns the spins along a local $\langle 111\rangle$ axis, forcing the spins of the Tb^{3+} ions to point towards or away from the center of the tetrahedra. More rigorously stated, the matrix elements of the angular momentum ladder operators (J_+ and J_-) vanish within the ground state manifold. This is stated in Equation 5.2 below.

$$\langle \pm|J_x|\pm\rangle = \langle \pm|J_y|\pm\rangle = \langle \pm|J_x|\mp\rangle = \langle \pm|J_y|\mp\rangle = 0 \tag{5.2}$$

Where J_i are the usual angular momentum operators. In the rare-earth pyrochlores, the dominant interaction is the Heisenberg nearest-neighbor antiferromagnetic interaction [32] and the dipolar interaction is secondary. In the case of $Tb_2Ti_2O_7$ the hyperfine interaction becomes important below approximately 500mK [14]. These interactions are shown in Equation 5.3

$$H_{\text{dipole}} = \frac{1}{2}(g_{\text{L}}\mu_{\text{B}})^2 \sum_{i \neq j} L_{ij}^{zz} J_i^z J_j^z$$

$$\text{Where: } L_{ij}^{zz} = \frac{\mid r_{ij} \mid^2 -3zij^2}{\mid r_{ij} \mid^5}$$

$$H_{\text{Heisenberg}} = \frac{1}{2} J_{\text{exch}} \sum_{i,NN} J_i^z J_j^z$$

$$H_{\text{HF}} = A_{\parallel} \sum_i I_i^z J_i^z \tag{5.3}$$

Where symbols retain the same meaning as in Chapter 4, but applied to $Tb_2Tb_2O_7$ and the magnetic Tb^{3+} ions. The model Hamiltonian which incorporates these interactions on the pyrochlore lattice with an Ising constraint is known as the dipolar spin ice model, $H_{\text{dsim}} = H_{\text{dip}} + H_{\text{Heis}}H_{\text{HF}}$. Gingras *et al.* [35] presented a convincing report which measured dc susceptibility, neutron scattering, and specific heat capacity of $Tb_2Ti_2O_7$. From these measurements, summarized in Figure 5.2 Gingras *et al.* found a Curie-Weiss temperature of $\theta_{\text{cw}} \approx -19\ K$, indicating antiferromagnetic correlations in $Tb_2Ti_2O_7$. Naively the Curie-Weiss temperature also indicates that $Tb_2Ti_2O_7$ may order at a temperature on the order of 10K, we will see that theoretical work indicates a transition temperature near 1K [23], and experimentally no ordering is observed in $Tb_2Ti_2O_7$ at temperatures as low as 50mK [31]. The contribution from the crystalline electric field was found to be $\theta_{\text{cf}} \approx -6K$ from susceptibility measurements of dilute $Tb_2Ti_2O_7$, where 98% of terbium ions were substituted with yttrium ions. Factoring in estimates for the strength of the nearest neighbor dipolar interaction yields a range of $\theta_{\text{dip}} \approx [1.2, -2.4]$K. The dipolar interaction, θ_{dip}, is straddling the ferromagnetic-antiferromagnetic (ie: positive-negative) crossover. dc susceptibility measurements indicated that the moment of Tb^{3+} is approximately $9.6\mu_B$, close to the value expected of the free ion. The neutron scattering measurements provided the energy level scheme presented in Equation 5.1.

Hamaguchi *et al.* measured the specific heat, susceptibility, and residual magnetization of single crystal samples of $Tb_2Ti_2O_7$ in attempting to determine the low temperature magnetic state of $Tb_2Ti_2O_7$ [37]. Hamaguchi *et al.* observed a history dependant susceptibility and magnetization behavior in $Tb_2Ti_2O_7$. Luo *et al.* measured dc susceptibility of $Tb_2Ti_2O_7$, and also observe differences in field cooled and zero field cooled susceptibility measurements in addition to an ordering transition near 70mK [27]. Luo *et al.* interpret the anomaly at 70mK as $Tb_2Ti_2O_7$ moving into a spin glass state. The susceptibility and magnetization measurements of Hamaguchi *et al.* and Luo *et al.* are shown in Figure 5.3.

The results of Hamaguchi *et al.* and Luo *et al.* are at odds with previously published muon spin resonance, neutron spin echo and neutron scattering measurements by Gardner *et al.* in 1999 [28], Gardner *et al.* in 2003, and Keren *et al.* in 2004. Gardner *et al.*'s 2003 report also

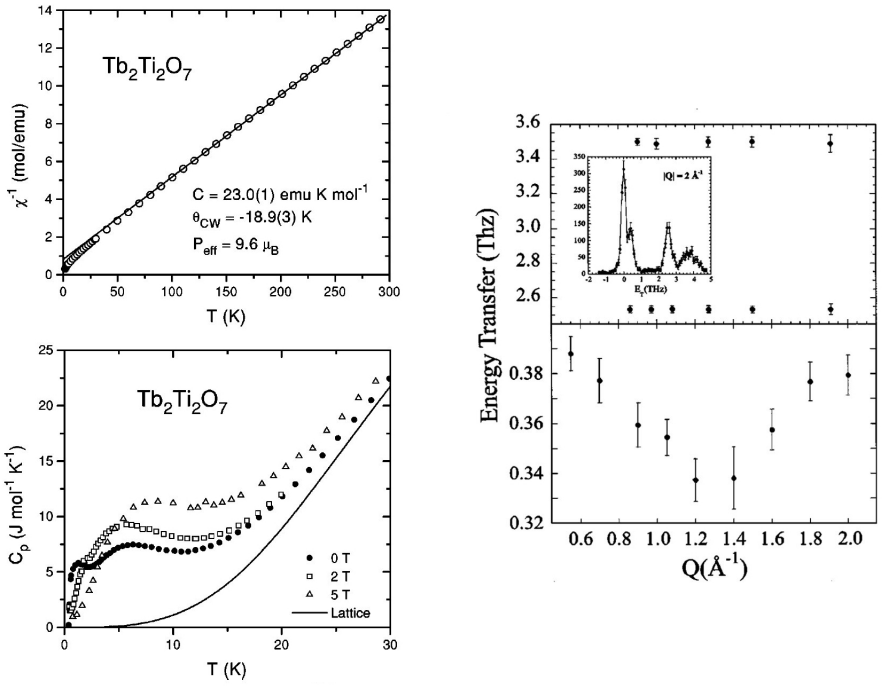

Figure 5.2: Measurements from Gingras *et al.* [35] used to determine the energy landscape of $Tb_2Ti_2O_7$. Top left: dc susceptibility measurements showing a Curie-Weiss temperature of -19 K. Bottom left: Specific heat measurements showing evolution with the application of a magnetic field. The solid line is the lattice contribution to specific heat, estimated from the isostructural nonmagnetic $Y_2Ti_2O_7$. Right: Inelastic neutron scattering measurements at 12 K from Gingras *et al.*, showing excitations at 0.36 THz (≈ 18 K), 2.5 THz (≈ 120 K), and 3.5THz (≈ 168 K).

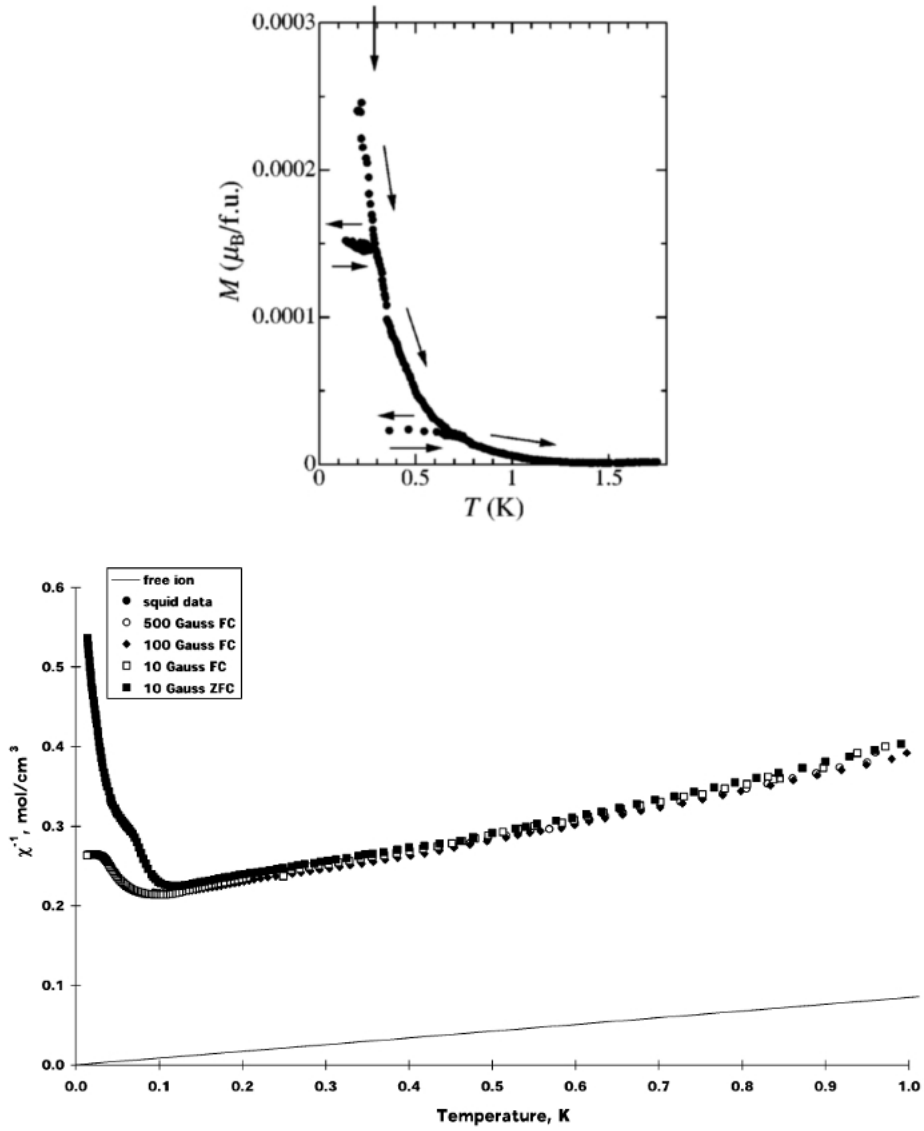

Figure 5.3: Top: Magnetization measurements from Hamaguchi *et al.* [37]. Bottom: Susceptibility measurements of Luo *et al.* [27]. Both show history dependence, Luo *et al.* observe an ordering feature near 70mK. This was interpreted as $Tb_2Ti_2O_7$ entering a spin glass state.

observed the glassy behavior in susceptibility seen by Luo *et al.*. However when coupled with the neutron scattering and spin echo measurements they concluded that this transition was due to defects in the crystal, and that the majority of spins within $Tb_2Ti_2O_7$ remained dynamic at these temperatures.

Hamaguchi *et al.* also repeated specific heat and susceptibility measurements of $Tb_2Ti_2O_7$ in 2004 [37]. While Gingras *et al.* measured specific heat from 400mK to 30K, Hamaguchi *et al.* investigated the region from ≈100mK to 6K, shown in Figure 5.4. Above 500mK there is good qualitative agreement, however Hamaguchi *et al.* observe a large peak at 370mK, which they interpret as a second order phase transition. This is compared with the results of Chapuis, discussed below.

Chapuis suggests that the differing specific heat results presented above are due to sample defects or differences in preparation [16]. Chapuis performed specific heat measurements on 4 different samples grown under various conditions. Samples were grown using a floating zone technique. Samples A and B were grown by mixing TiO_2 and Tb_4O_7, grown in an Argon atmosphere at 8mm/h. Sample C was grown by mixing TiO_2 and Tb_2O_3, grown in an Oxygen atmosphere at 7mm/h. Sample D was grown by mixing TiO_2 and Tb_4O_7, grown in an Argon atmosphere at 3mm/h for half the sample, and 8mm/h for the other. These results are shown in Figure 5.4. The sample from Crystal D grown at 3mm/h is the only sample which repeats the specific heat anomaly observed by Hamaguchi *et al.*, shown in Figure 5.2. As can been seen from the results of Chapuis, this specific heat anomaly is dependant on the growth conditions and may be sample specific.

Chapuis *et al.* also presented a manuscript based on the results shown in Figure 5.4 which suggests that the ground state of $Tb_2Ti_2O_7$ is actually a singlet, with a small gap ($\delta \leq 2$K) to an excited singlet [17]. While they acknowledge the need for further experimental and theoretical work to verify this, it is worth mentioning that the ground state manifold is not completely certain.

The theoretical community has been working in tandem throughout the experimental investigations discussed above. In 2000, den Hertog *et al.* performed Monte Carlo simulations using the dipolar spin-ice model on rare earth pyrochlores to investigate the effect and experimental signatures of variations in the exchange and dipolar coupling [23]. Using the estimates of the relative strength of the dipolar interaction presented by Gingras *et al.* [35] for $Tb_2Ti_2O_7$ above ($\theta_{\text{dip}} \approx [1.2, -2.4]$K), this investigation states that the ground state of $Tb_2Ti_2O_7$ is close to the boundary between a spin-ice state, or an ordered antiferromagnetic state of all spins pointing in or out of their tetrahedra.

In 2003 Kao *et al.* [41] used the low-energy states $|\pm\rangle$ and $|E_\pm\rangle$ above to perform random phase approximation calculations which allows excitations out of the ground state to describe $Tb_2Ti_2O_7$. While this work was able to qualitatively reproduce the neutron spectra observed by Gardner *et al.* [29], the calculations predicted an ordered all-in/all-out ordered antiferromagnetic ground state.

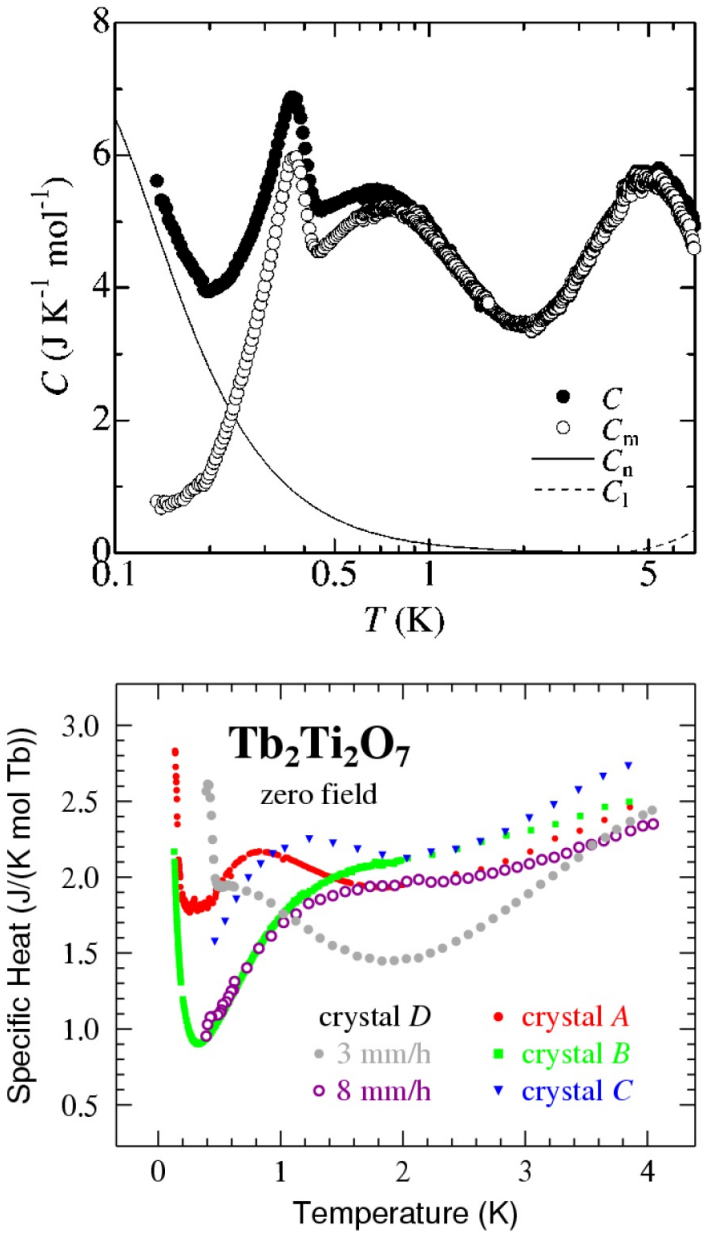

Figure 5.4: Top: Specific heat measurements performed by Hamaguchi *et al.* [37], showing a large spike near 370mK which is interpreted as an ordering transition. Bottom: Specific heat measurements by Chapuis [16]. See text for different conditions of growth of the samples used by Chapuis. Note the specific heat anomalies are dependant on the sample studied.

Following this in 2004, Enjalran *et al.* [26] focussed exclusively on $Tb_2Ti_2O_7$ and the neutron diffraction spectra observed by Gardner *et al.* in 2001 [29]. Using mean-field theory Enjalran *et al.* confirmed the predicted ordering of den Hertog *et al.*'s 2001 report. Albeit somewhat qualitative, the comparing neutron scattering spectra predicted from theoretical mean-field theory and the observation demonstrated that the magnetic spins within $Tb_2Ti_2O_7$ could not be described by a localized $\langle 111 \rangle$ Ising model. Better agreement was found by modelling $Tb_2Ti_2O_7$ as an anisotropic Heisenberg system and allowing the spins of $Tb_2Ti_2O_7$ to cant away from the Ising direction. This model was unable to explain the spin-liquid ground state of $Tb_2Ti_2O_7$, so further theoretical work remained.

Recently, Molavian *et al.* have presented two reports which introduce a scheme to allow virtual excitations in and out of the excited states of $Tb_2Ti_2O_7$ in an attempt to explain the absence of ordering [50, 49]. By allowing for virtual excitations the necessary relaxation of Ising spins is reached, allowing the spins to tilt away from the Ising axis. This scheme also qualitatively reproduces the neutron scattering spectra observed by Gardner *et al.* in 2001 [29], as shown in Figure 5.5. This agreement does support the scheme presented by Molavian *et al.*, however the neutron scattering spectra are somewhat insensitive to these interactions. Further, the interactions in $Tb_2Ti_2O_7$ are not well known so this may not be a 'smoking gun' experiment.

As seen in the bottom of Figure 5.5 Molavian *et al.* present a prediction of the diffuse neutron scattering as a function of the nearest neighbor exchange energy J_{exch} at 400mK and 40mK. This provides a possible test of the proposed virtual excitations. Molavian *et al.*'s 2009 report [49] also presents a prediction of the correlations the crystal field excitations produce based on the exchange interaction, shown in Figure 5.6. The error bar indicates the uncertainty in the exchange energy of $Tb_2Ti_2O_7$. It is notable that the $\mathbf{q}$=0 wavevector of the long-range spin ice ($LRSI_{000}$ in the figure) is caused by the virtual excitations scheme presented by Molavian *et al.*, and is the ordering wavevector observed in the closely related compound $Tb_2Sn_2O_7$ [47].

As of this writing, this represents a small subset of the work on $Tb_2Ti_2O_7$ but illustrates the difficulty in describing this novel magnetic system. The ground state of $Tb_2Ti_2O_7$ is still debated, and the exact mechanism which prevents ordering at the lowest temperatures measured is not understood. Simply stated more work to understand the role and origin of fluctuations in $Tb_2Ti_2O_7$ is required.

Before $Tb_2Ti_2O_7$ became a hot topic of magnetically frustrated systems it was interesting due to its other properties. Aleksandrov *et al.* performed a series of studies on $Tb_2Ti_2O_7$ which measured specific heat, magnetization, and magnetostriction [40]. The magnetostriction measurements are shown in Figure 5.7, and showed that $Tb_2Ti_2O_7$ exhibits giant magnetostriction at low temperatures. Aleksandrov *et al.* assumed that magnetostriction would be isotropic. Aleksandrov *et al.*'s analysis assumed a simpler energy level structure of $|\pm\rangle = a|\pm 5\rangle - b|\mp 1\rangle$ and $|E_\pm\rangle = a'|\pm 4\rangle - b'|\mp 2\rangle$ and was able to qualitatively reproduce specific heat and magnetization measurements, and quantitatively reproduce magnetostriction measurements. These results were based on single-ion interactions. More recent results (such as the lack of ordering well below the

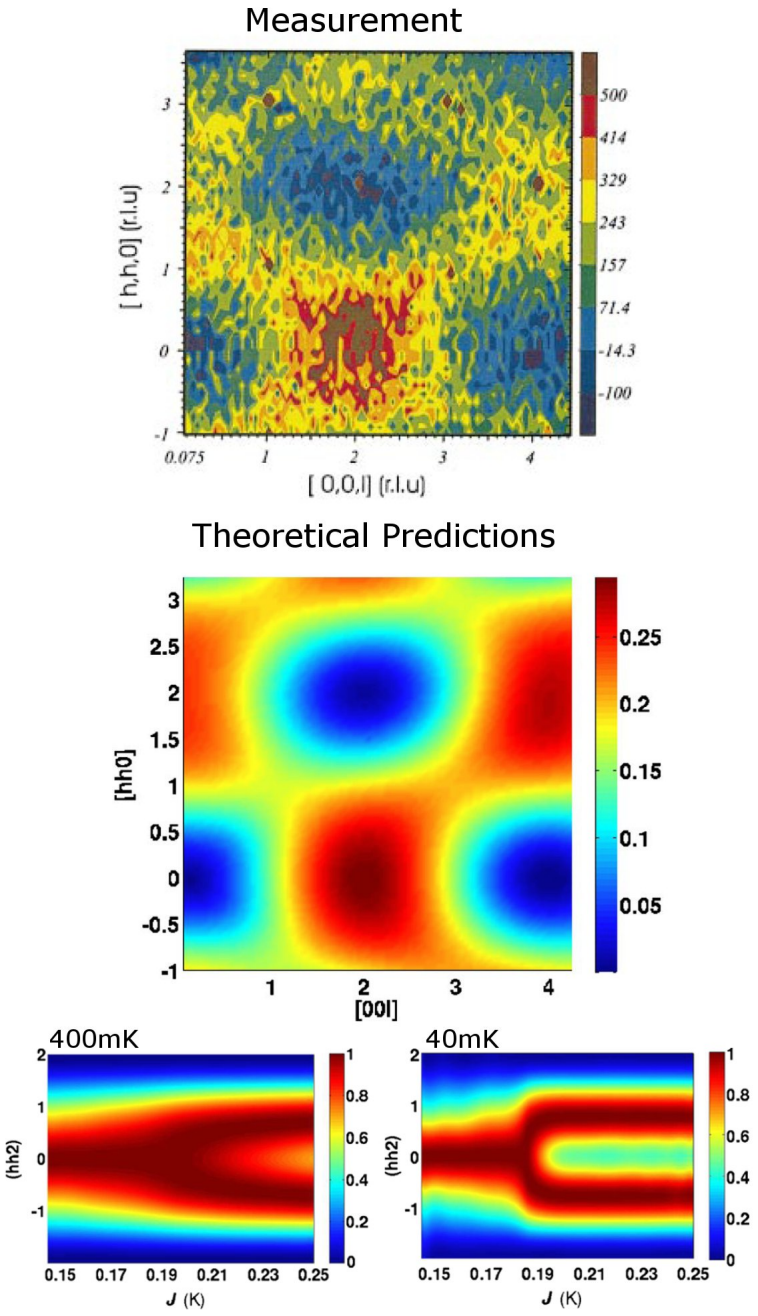

Figure 5.5: Diffuse neutron scattering spectra of $Tb_2Ti_2O_7$. Top: Measurements by Gardner *et al.* [29]. Middle: Prediction of spectra by Molavian *et al* [50]. Bottom: Prediction of diffuse neutron scattering along (hh2) as a function of the nearest-neighbor interaction strength, J_{exch}, at temperatures 400mK and 40mK.

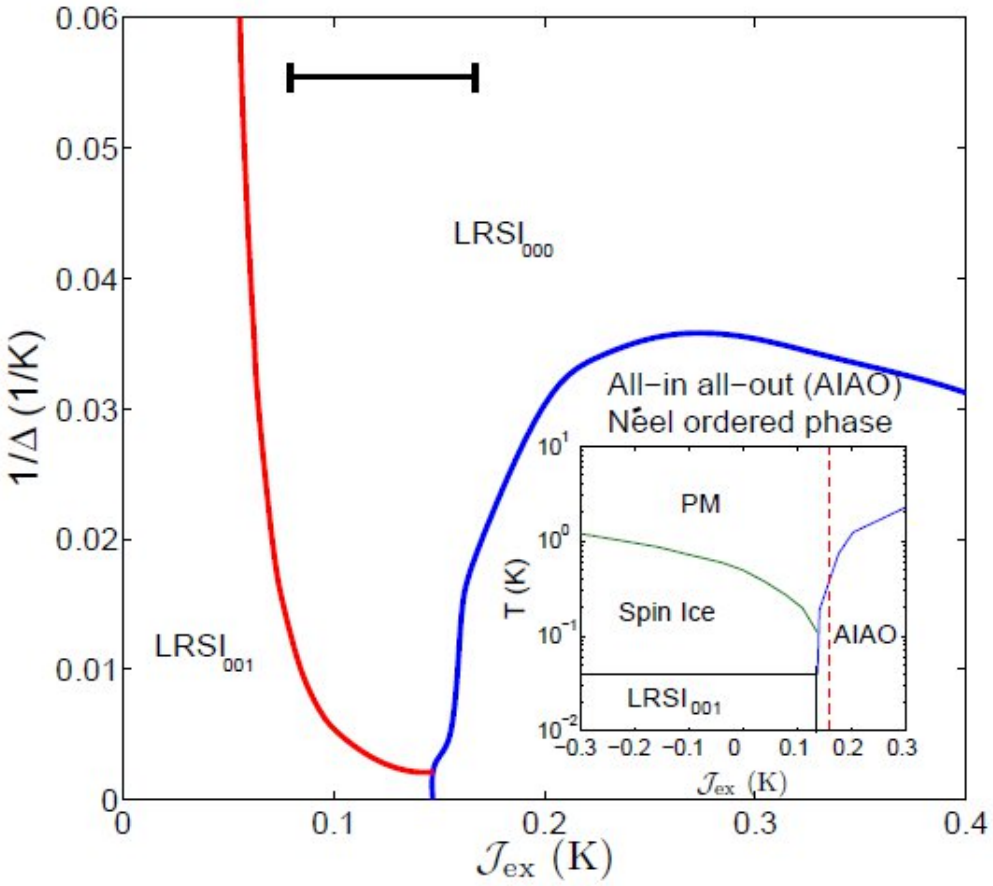

Figure 5.6: Theoretical phase diagram of $Tb_2Ti_2O_7$ as a function of the exchange energy from Molavian *et al.* [49]. The gap between the ground state doublet and the first excited doublet is set to 18 K and the dipolar exchange set to J_{dip} = 0.0315 K, appropriate for $Tb_2Ti_2O_7$. The error bar shows the uncertainty in the exchange energy in $Tb_2Ti_2O_7$. Inset shows the phase diagram plotted as temperature versus the exchange energy. At J_{exch} = 0 the ground state is predicted to be a long range spin ice state with an ordering vector $\mathbf{q}$ = (001) ($LRSI_{001}$), as temperature is increased changes to a spin ice state.

Curie-Weiss temperature) demonstrate that while agreement may be reached using a single-ion approach, it cannot capture all of the physics at work within $Tb_2Ti_2O_7$ [50, 49, 32, 28].

Ruff *et al.* investigated the giant magnetostrictive response using X-ray scattering [64] in a transverse pulsed magnetic field. These measurements are shown in the top of Figure 5.8. Interestingly when the magnetostriction is scaled by temperature, Ruff *et al.* noted that for curves at 20K and above the magnetostriction corresponds to a squared Brillouin function. This is in agreement with the expectation for a simple paramagnet that the magnetostriction should correspond to the square of the magnetization [25], where magnetization can in turn be described by a Brillouin function. At 4.5K this response changes to power-law behavior which could be due to the onset of a spin liquid behavior.

Anisotropy in the magnetostrictive response was also observed by Ruff *et al.* (shown in box b) of Figure 5.8), in stark contrast to the assumptions of Aleksandrov *et al.*. Ruff *et al.* applied a magnetic field along the [110] and [100] axes and measured expansion along the [001] axis of $Tb_2Ti_2O_7$. They found that the response of this transverse magnetostriction (where expansion is measured perpendicular to the applied field) was suppressed when the field was applied along the [100] axis as shown in box c) of Figure 5.8. To explain this observation, we refer to box (d) of Figure 5.8. This shows a subset of the Tb^{3+} spins within $Tb_2Ti_2O_7$, where all spins point along their local Ising easy axis. Blue spins have a component of spin transverse to [110], while red spins do not. When the magnetic field is applied, the blue spins (with a component transverse to [110]) must work more strongly against the crystalline electric field constraints before they are fully polarized. This could lead to a greater distortion of the oxygen cage surrounding Tb^{3+} ions than is required to polarize the red spins, leading in turn to a greater magnetostrictive response. This explanation assumes that spins point along their local Ising axis. While arguments for relaxation of a strict local Ising condition have been presented above, Molavian *et al.* [49] also investigated the effects of the restored isotropy and suggest that this may be a small effect, on the order of a few degrees. We may thus consider that spins remain Ising-like, and the above explanation remains valid.

Ruff *et al.* have also reported anomalous thermal expansion of $Tb_2Ti_2O_7$ below 20K [63]. Using X-ray scattering they observed a contraction of the lattice constant $\Delta a/a$ as temperature was lowered from 300K to 20K, then anomalous expansion below 20K. This response is compared to the nonmagnetic isostructural $Y_2Ti_2O_7$ in Figure 5.8. This expansion was by Ruff *et al.* interpreted as the onset of cubic to tetragonal structural fluctuations which precede a Jahn-Teller phase transition, based on the similarity in the splitting of the Bragg peaks with other instances of Jahn-Teller phase transitions. This proposed transition does not fully develop (which would be observed by a splitting of the (12,0,0) Bragg peak) above 300mK, the lowest observed temperature.

Both of the anisotropic magnetostriction and anomalous thermal expansion results presented by Ruff *et al.* indicate unexpected effects at low temperatures and in an applied magnetic field, which could be investigated further using capacitive dilatometry. Such measurements could sig-

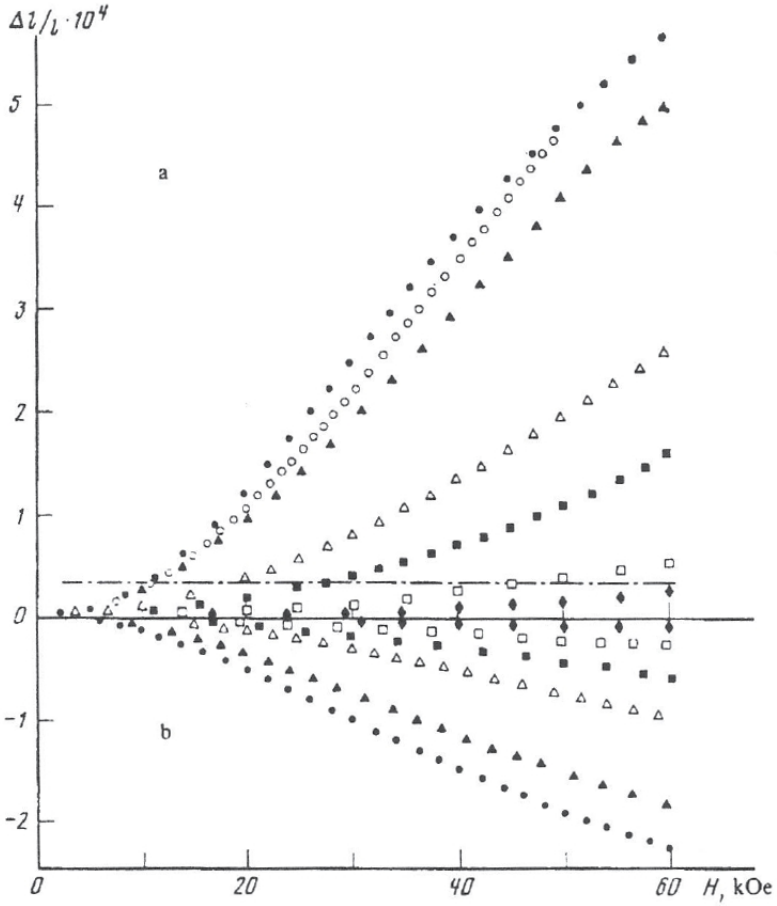

Figure 5.7: Magnetostriction measurements of $Tb_2Ti_2O_7$ performed by Aleksandrov *et al.* [40]. The positive curves in the plot are longitudinal magnetostriction, negative curves are transverse magnetostriction. Polycrystalline measurements were performed at: ● 4.2K, ▲ 8K, △ 16K, ■ 25K, □ 50K, ◆ 78K. ○ are single crystal measurements at 4.2K, with the field applied parallel to [111].

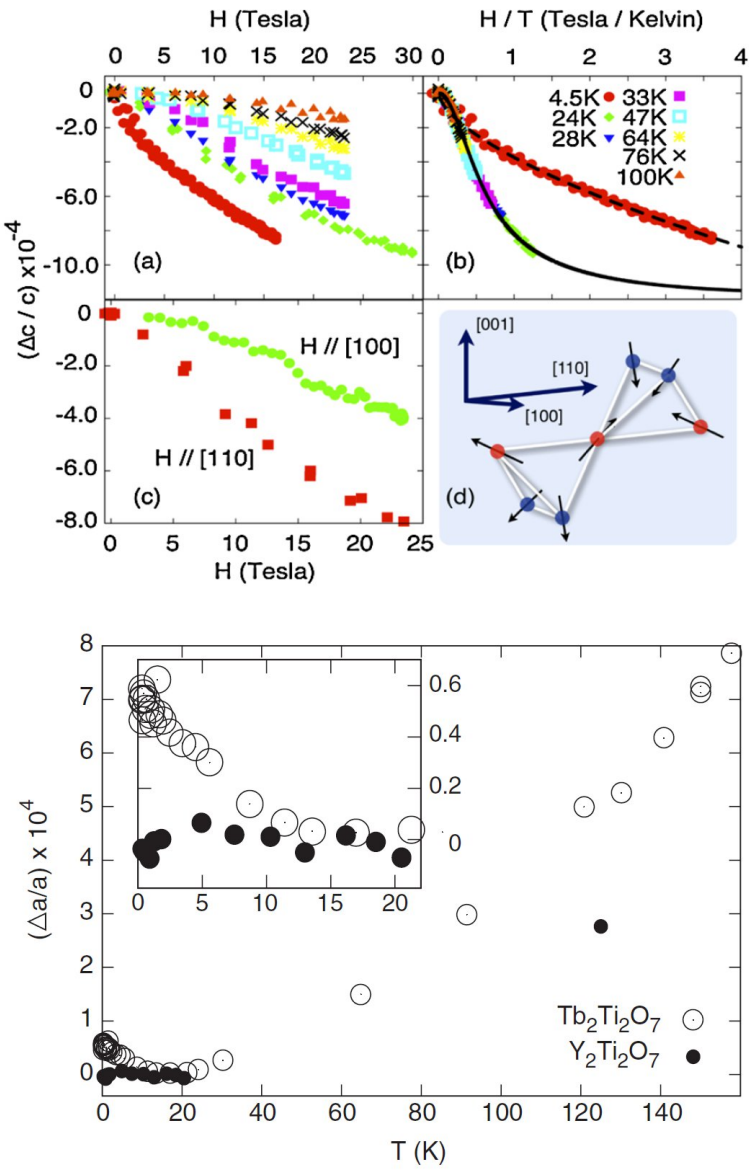

Figure 5.8: Top: Transverse magnetostriction of $Tb_2Ti_2O_7$measured using X-ray scattering in a pulsed magnetic field from Ref [64]. Top left (a) shows the magnetostriction, while b) shows the magnetostriction scaled by temperature. Note the different form of the 4.5K sweep (red dots) compared to other measurements. c) demonstrates the anisotropy of response at 20K. d) is a subset of spins in $Tb_2Ti_2O_7$. Blue spins have easy-axis transverse to [110] while red spins have some component of their spin along [110]. Bottom: Thermal expansion of the crystal lattice $(\Delta a/a)$ from Ref. [63]. Inset: Response below 20K.

nificantly improve the resolution of the available information, hopefully providing further information regarding the onset of the proposed transitions.

In addition to the proposed zero-field transition of Ruff *et al.*, Mirebeau *et al.* [48] observed an ordering transition with the application of pressure, Rule *et al.* [66] and Cao *et al.* [13] observed a similar transition with an applied magnetic field. The pressures required to induce a phase transition at 1.4K were on the order of GPa, far above the pressure applied to the $Tb_2Ti_2O_7$ samples in the dilatometric work which will be presented in the following sections. Since the facility to test a transition with the application of pressure is not available using the dilatometer, the transition due to an applied pressure will not be discussed further.

Rule *et al.* [66] used time-of-flight neutron scattering, while Cao *et al.* [13] used polarized and unpolarized neutron diffraction. Both applied a magnetic field parallel to [110] to induce ordered phases in $Tb_2Ti_2O_7$, as shown in Figure 5.9. Contributions from two ordered phases have been observed in the scattering patterns: a spin-ice like ferromagnetically ordered state with an ordering vector **k**=(000), shown in the top of Figure 5.9, and an antiferromagnetically ordered spin ice state with **k**=(001) which supports spin wave excitations, shown in the middle of Figure 5.9. The **k**=(000) is a "2-in 2-out" spin ice state as in to $Tb_2Sn_2O_7$, wherein each unit cell assumes a finite magnetization which yields a bulk ferromagnetic ordering. The **k**=(001) is also a "2-in 2-out" state, however two of the four tetrahedra have a net magnetization which directly opposes the other two tetrahedra. Both states exhibit modulated moments, where the α-chain Tb^{3+} ions take on a moment of $5.7\mu_B$ and the β-chain Tb^{3+} ions 1-$2\mu_B$. In the absence of an applied field the spin liquid or cooperative paramagnetic phase is observed. The **k**=(000) state exists at all applied fields and temperatures measured (where the weakest applied field was 1T at 300mK). For fields stronger than 2T the **k**=(000) and **k**=(001) coexist, while the **k**=(001) state has a correlation length of approximately 70Å.

The above studies demonstrate interesting anisotropic magnetostrictive effects and a rich phase diagram for $Tb_2Ti_2O_7$ in an applied magnetic field. Further magnetostrictive measurements below 20K would indicate the onset of power-law behavior. An investigation, such as dilatometry, which can probe the onset of the ordered states observed by Cao *et al.* [13] and Rule *et al.* [66] could add further detail to the phase diagram of $Tb_2Ti_2O_7$.

5.2 Experimental Method

In light of the extremely brief review given in the previous section, there are many avenues of investigation available. This section describes the thermal expansion and magnetostriction measurements performed in the hopes of confirming the observations of Ruff *et al.* [64, 63] regarding the anomalous thermal expansion below 20K and giant magnetostrictive behavior. Verification of the ordering transition observed by Rule *et al.* [66] and Cao *et al.* [13] was also attempted. A thorough dilatometric investigation of $Tb_2Ti_2O_7$ with an applied magnetic field along [100],

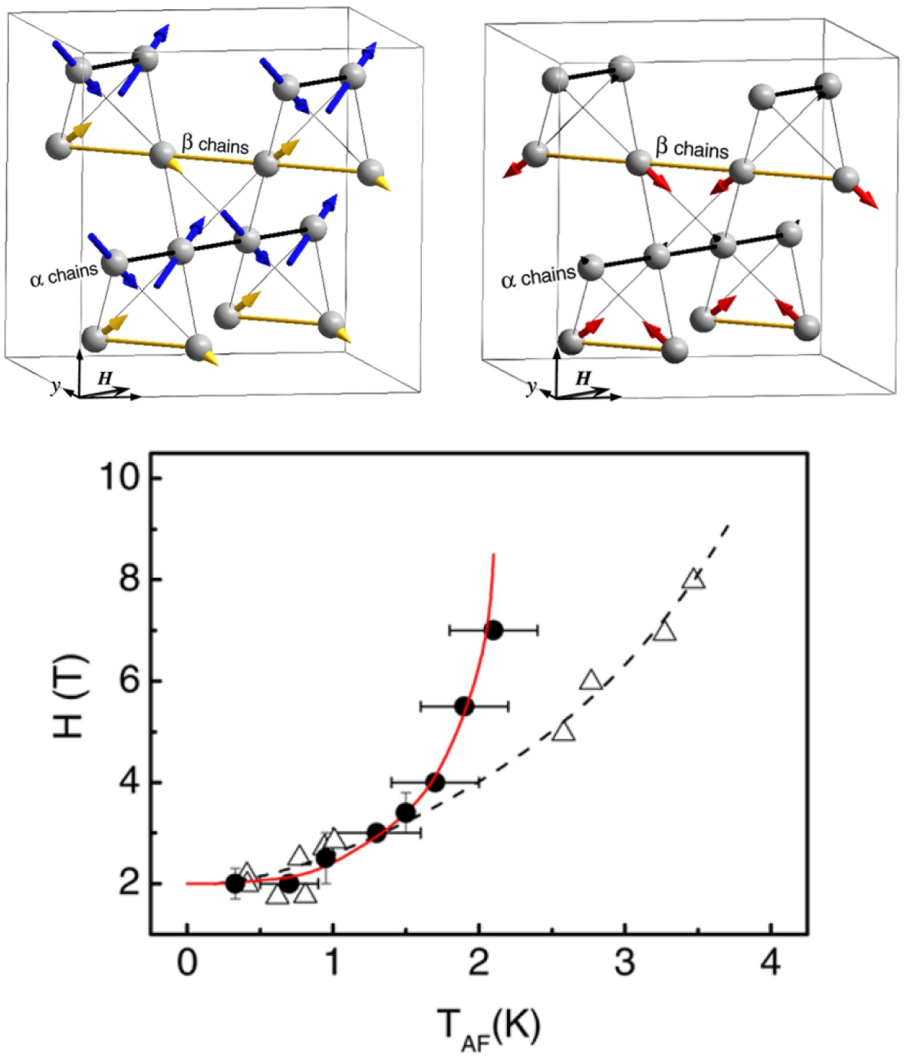

Figure 5.9: Field-induced ordered phases in $Tb_2Ti_2O_7$, from Cao *et al.* [13]. Top left: Ferromagnetically ordered **k**=(000) phase. Each tetrahedra has a net magnetic moment, these moments are aligned. Arrows indicate the relative size of induced moments on Tb^{3+} ions. Top right: Antiferromagnetically ordered **k**=(001) phase. Each tetrahedra again has a moment, however they are antiparallel such that the unit cell has a net zero magnetization. Bottom: H-T phase diagram of these states. ● are critical points determined by Cao *et al.*, △ are from Rule *et al.* [66]. Lines are guides to the eye. Critical points indicate the onset of contributions from the antiferromagnetic **k**=(001) phase observed in the neutron scattering spectra, contributions from the ferromagnetic **k**=(000) phase exists for all applied fields.

[110], and [001] was intended. Due to time constraints and experimental difficulties, much less was achieved. This section ends with a long list of experiments left to be done.

The $Tb_2Ti_2O_7$ sample used was provided by B. Gaulin's group at McMaster university, and was part of the same batch used in measurements performed by Ruff *et al.*. Details of the crystal growth are provided in Reference [30].

Thermal expansion was measured using the pumped ^{4}He probe described in Chapter 3 to reach temperatures as low as $\approx$ 1.2K. To reach lower temperatures, the Kelvinox MX400 dilution refrigerator was used. In the MX400 an uncalibrated RuO_2 thermistor and a thermal link made of annealed silver wire was pressed against the bottom of the sample holder. The silver wire was also pressed directly against the bottom of the mixing chamber. The dilatometer was mounted to the bottom of the mixing chamber using an oxygen free high conductivity copper mount with a large surface area clamped around the shell of the dilatometer, providing contact on approximately half of the total outer surface area of the shell. The OFHC copper clamp was then bolted to the mixing chamber. All surfaces were polished using acetone and a abrasive pad before mounting the dilatometer to the mixing chamber to improve thermal contact between components.

The dilatometer used in this investigation is similar to that described in Chapter 3, however in place of a sapphire pin separating the spring from the floating capacitor plate was a Kapton sheet and layers of Stycast 2370 epoxy to bind the floating capacitor plate to the spring. The upper capacitor assembly also used a combination of Kapton and Stycast in to bind the fixed capacitor plate to the lock ring.

5.3 Results and Discussion

5.3.1 Thermal Expansion

The low temperature thermal expansion measurements performed in the dilution unit are shown in Figure 5.10. The dilatometer was fitted with an uncalibrated RuO_2 thermistor in order to verify the temperature stability of the sample. Unfortunately cold break in the V- line of the 4-wire measurement rendered this thermistor unusable for the duration of the experiment. In addition to this, the capacitance measurement was found to create significant heating of the communication lines within the dilution refrigerator. These two issues cause concern regarding the actual temperature of the sample. In order to remove the heating in the communication lines future experiments should make use of available superconducting twisted pairs. This necessitates performing the low-temperature thermal expansion again before attempting serious interpretation of the results below.

The $Tb_2Ti_2O_7$ sample used in thermal expansion measurements in the dilution unit was a needle-shaped sample approximately 2.3 mm long, with a 0.46x0.74 mm cross-section. It was

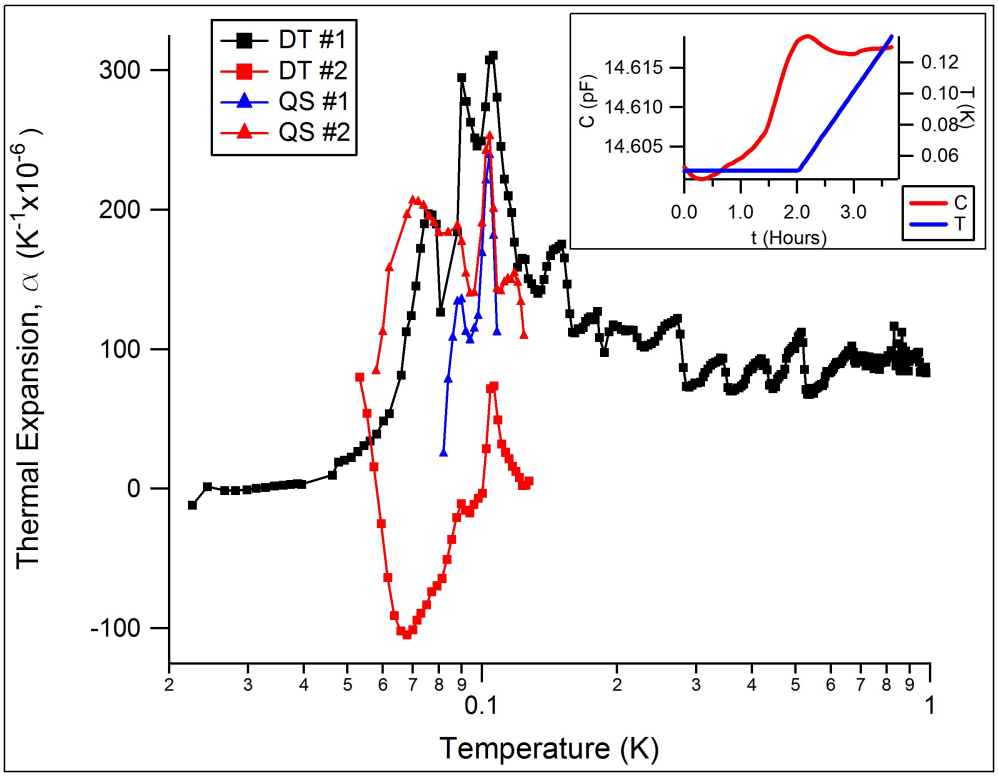

Figure 5.10: Thermal expansion measurements of $Tb_2Ti_2O_7$ from 20 mK to 1 K. The legend indicates the method of temperature control used, DT indicating dynamic temperature control, QS indicating quasi-static control. The effect of poor thermalization (inset) is shown by DT #2. The steep decrease in DT #2 from 50 mK to 70 mK and the overall offset are thought to be effects of slow thermalization. The oscillations and discontinuities in DT #1 arise from changing PID values and poor temperature control. Inset: Data of DT #2. Capacitance is in red, temperature in blue and both plotted again time in hours. Note the lack of equilibration, leading to the effects shown in the main plot.

mounted in a sample holder with an appropriately sized slot and held in place using silver paint. The silver paint also provided extra thermal contact between the $Tb_2Ti_2O_7$ sample and the sample holder.

Thermal expansion was measured using both quasi-static and dynamic temperature sweeps. As can be seen in Figure 5.10, if the system was not allowed to equilibrate before a dynamic temperature sweep then thermal expansion was offset (shown in DT # 2, where DT indicates dynamic temperature control was used). Capacitance was monitored before starting other trials and allowed to stabilize. The inset of Figure 5.10 shows the measured capacitance and temperature plotted versus time of the run DT #2 shown in the main figure. At the lowest temperatures the dilatometer was found to have a long settling time (on the order of several hours), as shown inset. By process of elimination, it was thought that this effect was due to the Kapton and Stycast used in the dilatometer during this experiment. Long thermalization times could be due to two effects: a comparatively large heat capacity, or low thermal conductivity at very low temperatures. A very small amount of Kapton and Stycast were used, so a large heat capacity is unlikely to be the cause. In contrast, Stycast and Kapton are known to have thermal conductivities orders of magnitude smaller than silver in the temperatures studied [56, 65]. Stainless steel, silver, and beryllium copper are all commonly used materials in cryogenic physics applications and do not exhibit such poor thermal conductivity or large heat capacity. This lead to a redesign of the dilatometer which removed Kapton and reduced the use of Stycast. Finally, the oscillations and discontinuous jumps in the curve labelled 'DT #1' in Figure 5.10 above 100mK arise from changes in the PID temperature control settings and overall unsatisfactory temperature control. See Appendix A for further details on temperature control.

With the above caveats, both the quasi-static and dynamic temperature control exhibited a significant repeatable feature around 100 mK, in agreement with Luo *et al.*'s 2001 report [27]. The origin of this peak is mysterious although it could relate to a low temperature phase transition. Luo *et al.* suggest that the feature observed is a transition to a spin glass state. Gardner *et al.* [31] later used neutron spin echo measurements which showed that a small fraction of spins become quasistatic, while the vast majority remained dynamic down to 50mK. Gardner *et al.* interpret this as a small fraction of spins freezing near crystal defects, and suggest that this is the origin of the peak observed by Luo *et al.*. Chapuis [16] have also found significant sample dependence in the specific heat capacity and magnetization which could completely remove this feature. Further analysis of this low-temperature feature will be performed upon successful completion of this experiment.

In thermal expansion and magnetostriction measurements performed on the pumped ^{4}He probe a thin plate sample was used. The dimensions of plate were approximately 1.9x1.8x0.5 mm, with the normal of the large surface parallel to the crystallographic [001] axis, and the edges along [110] and $[\bar{1}10]$. The plate was used to allow for both the large response in magnetostriction and a small response in thermal expansion to be measured in the same experimental setup. The $Tb_2Ti_2O_7$ plate was held in place using a small amount of vacuum grease as the dilatometer

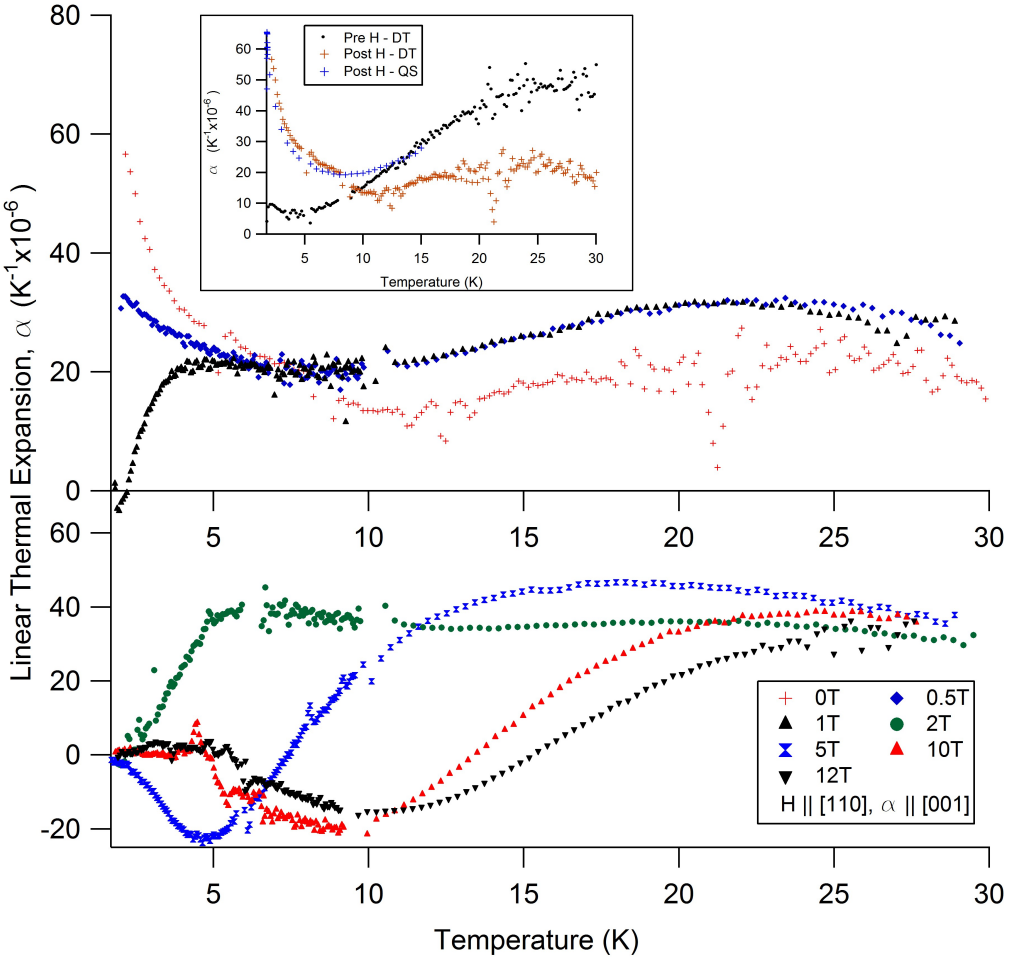

Figure 5.11: Top: Thermal expansion measurements along the [001] axis of $Tb_2Ti_2O_7$ from 1.2 K to 30 K and in a magnetic field applied along [110]. The top panel contains thermal expansion of $Tb_2Ti_2O_7$ with an applied field between 0T and 1T. The bottom panel contains thermal expansion measurements with an applied field between 2T and 12T. The low temperature peak in the 0T thermal expansion data approaches the value of the thermal expansion coefficient observed in Figure 5.10. This peak appears to be suppressed from its low temperature value and moved to higher temperature as the applied field is increased. Inset: Differences in thermal expansion before (Pre-H) and after (Post-H) $Tb_2Ti_2O_7$ has been exposed to a magnetic field. This could indicate either a history dependant thermal expansion, or a shift in the position of the sample.

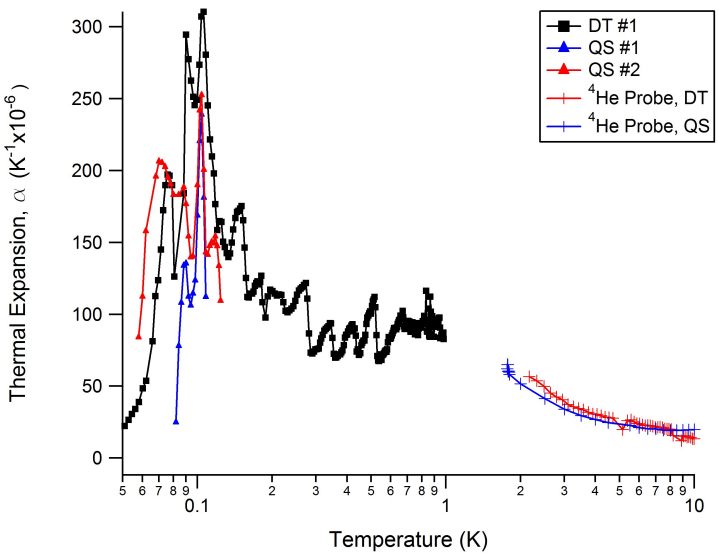

Figure 5.12: Thermal expansion measurements along the [001] axis of $Tb_2Ti_2O_7$ from 50mK to 10K. The peak observed near 1K using the pumped ^{4}He probe appears to approach the plateau observed using the dilution unit.

was assembled.

The higher temperature regime demonstrated interesting evolution with the application of a magnetic field. In the absence of an applied field, we see thermal expansion dropping from a peak which is beyond the low temperature range of the pumped probe. It is encouraging to note that the peak observed near 1K in the pumped probe is similar in magnitude to the plateau observed in Figure 5.10. This is shown clearly in Figure 5.12, which shows a subset of zero-field thermal expansion data from 50mK to 10K.

As larger fields are applied, this peak moves to higher temperature, similar to the specific heat behavior observed by Gingras *et al.* [35] (shown in Figure 5.2) and Cornelius *et al.* [21]. Both the investigation by Gingras *et al.* and Cornelius *et al.* made use of powder samples. Beyond this very rough qualitative comparison, agreement with previously published specific heat data is poor.

Discrepancies are reported between the gathered data and the thermal expansion of Ruff *et al.* [63] collected using x-ray scattering, shown in Figure 5.8. Ruff *et al.* observed anomalous expansion of the lattice parameter as temperature was lowered below 20 K, which would manifest as negative thermal expansion in Figure 5.11. This is not seen in any of the thermal expansion measurements done here. The inset of Figure 5.11 shows three thermal expansion trials, one done before any magnetostriction experiments, and two performed after magnetostriction trials.

As will be seen below, transverse magnetostriction measurements could not be performed due to a lack of reproducibility. The differences shown in the inset could be due to history dependant thermal expansion of $Tb_2Ti_2O_7$, similar to the history dependence observed in susceptibility measurements by Luo *et al.* [27], or in magnetization measurements of Hamaguchi *et al.* [37], or to the sample shifting in an applied field.

Finally, the investigation of $Tb_2Ti_2O_7$ in the pumped ^{4}He probe led to a more thorough study of the accuracy of the dilatometer being used. To remind the reader, the dilatometer used in the measurements of $Tb_2Ti_2O_7$ contained layers of Kapton film and Stycast epoxy directly along the measurement axis. After the lack of agreement with Ruff *et al.*'s anomalous negative thermal expansion coefficient below 20K, it was decided to investigate the repeatability and accuracy of the dilatometer in use by attempting to measure the thermal expansion of an oxygen-free high-conductivity copper sample. This measurement would test the resolution of the dilatometer: thermal expansion of copper and silver differ by a small amount, so the signal measured would not be significantly larger than the cell effect. This used the analysis presented in Chapter 3, the results of which are shown in Figure 5.13.

As can be readily seen, the agreement is very poor and strongly dependant on the method of temperature control used. The quasistatic trial maintained fluctuations below one part in one thousand for temperatures below 4K, and above 15K. The heating rate dynamic temperature sweep fluctuated by approximately 10% of the desired rate below 4K, and above 12K. In both cases, outside of the stated regions temperature control was poor. However even within the regions of acceptable temperature control the measured thermal expansion of copper does not agree between trials, and does not show consistent agreement with published values[83]. This motivated a redesign of the dilatometer such that Kapton was removed, and Stycast used in such a way to minimize its affect on measurements. The design in use is presented in Chapter 3, and shows a significantly improved determination of the thermal expansion of copper.

5.3.2 Magnetostriction

Magnetostriction measurements were carried out exclusively on the pumped ^{4}He probe. The same setup, sample and mounting method as in the thermal expansion measurements were used for magnetostriction measurements. The magnetic field was applied both parallel and perpendicular to the [001] direction. These measurements are shown in Figure 5.14 and compared with the results of Aleksandrov *et al.* [40].

Three issues are immediately apparent on comparing the measured response to previously published values. The first, and most notable, is a sign difference between the longitudinal magnetostrictive (shown top of Figure 5.14) measurements done in this work and in Aleksandrov *et al.*'s work [40]. A longitudinal magnetostrictive 'loop' is shown bottom right, the small shift in magnetostriction is caused by removal of a discontinuous jump in capacitance which occurred

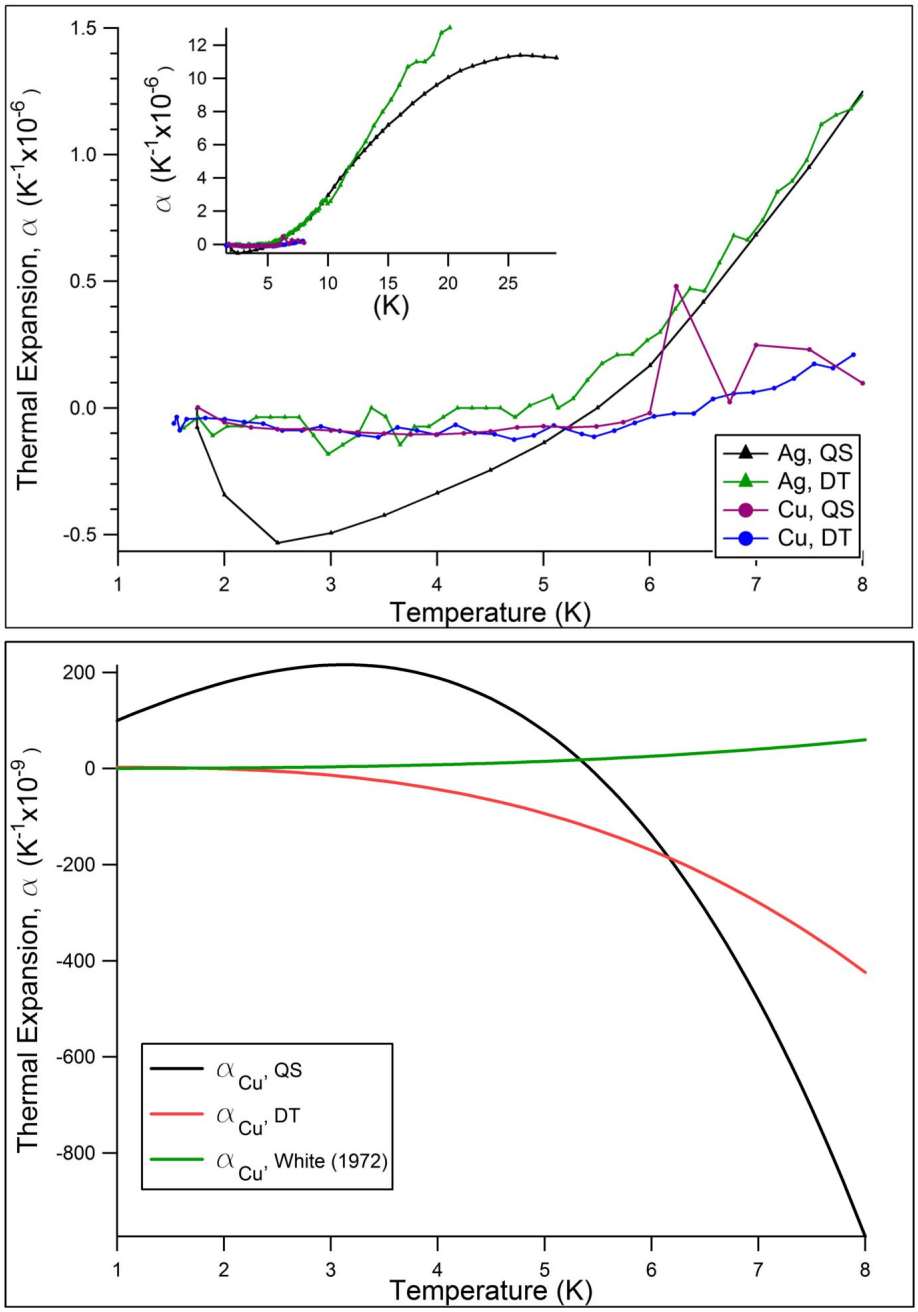

Figure 5.13: Top: Lack of reproducibility of thermal expansion in the pumped ^{4}He probe using copper and silver samples. Experiments used quasistatic (QS) or dynamic (DT) temperature control. Top inset: Thermal expansion of main figure over a larger temperature range. Bottom: Calculated thermal expansion of copper from measured data in bottom left, compared to White's 1972 work [84]. This discrepancy lead to the severe reduction of Stycast epoxy and removal Kapton film in the construction of the dilatometer.

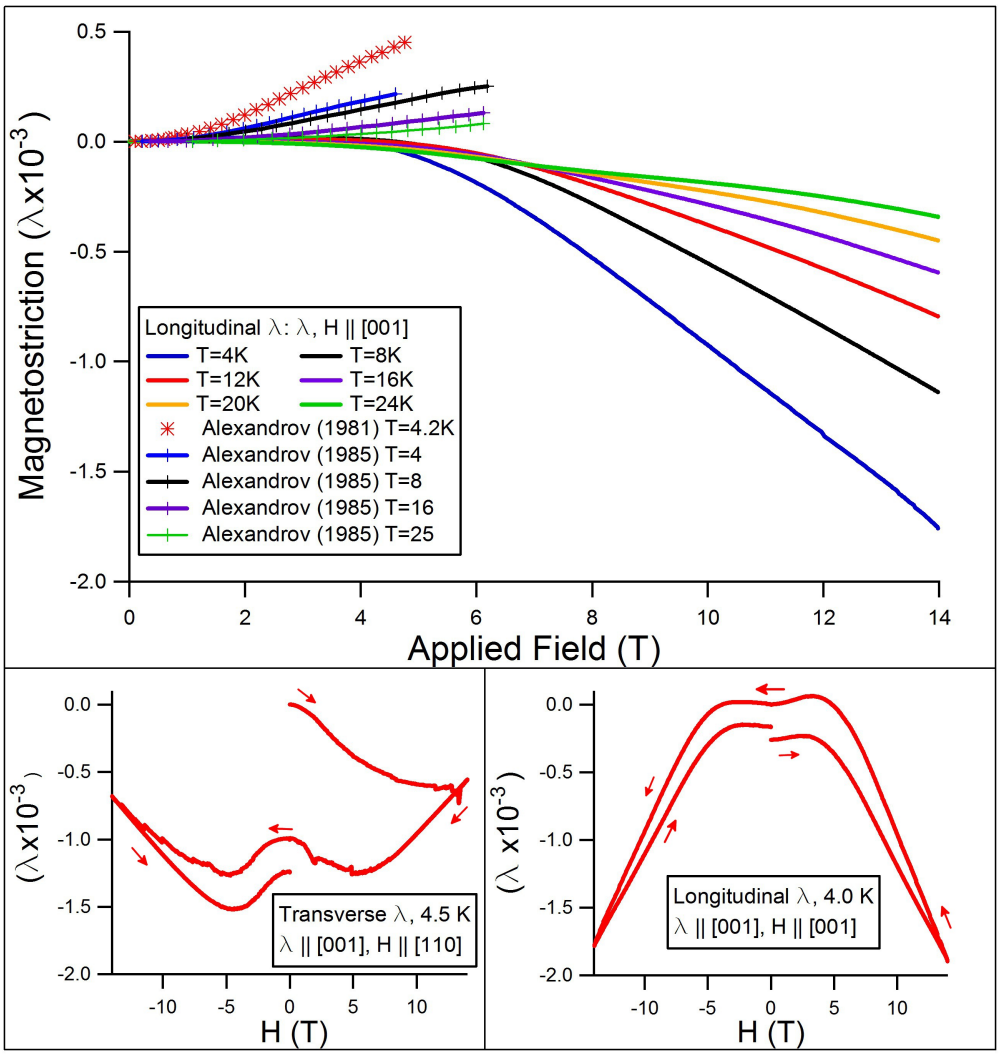

Figure 5.14: Magnetostriction measurements on $Tb_2Ti_2O_7$. Previous magnetostriction measurements from Aleksandrov *et al.* [40] are included. Magnetostriction at 4.2 K by Aleksandrov *et al.* was performed on a single crystal with **H**||[111], all other measurements were performed on polycrystalline samples. Bottom Left: Transverse magnetostriction 'loop', the applied field sweeps from $0T \Rightarrow 4T \Rightarrow -4T \Rightarrow 0T$, demonstrating the lack of reproducibility of transverse magnetostriction measurements. This lack of reproducibility is thought be caused by the mounting of the sample. Bottom Right: Longitudinal magnetostriction 'loop', the field again sweeps from $0T \Rightarrow 4T \Rightarrow -4T \Rightarrow 0T$. Longitudinal magnetostriction differs by a sign from the expectations based on Aleksandrov *et al.*'s and Ruff *et al.*'s works.

during the trial. Secondly the transverse magnetostriction (shown bottom left) is not repeatable. Finally, the scaling behavior discussed by Ruff *et al.* is not observed. There is, however, no direct comparison with any of the published data. Aleksandrov *et al.*'s single-crystal longitudinal magnetostriction measurements applied a magnetic field parallel to the [111] crystalline axis, while this work applied a field along [001]. Aleksandrov *et al.* assumed that the magnetostrictive response would be isotropic for all applied field directions [40], which was shown to be incorrect by Ruff *et al.* [64] and shown in Figure 5.8. Although it would not be unreasonable to observe some anisotropy, one would not expect the magnetostrictive response to change sign depending on the applied field for a paramagnetic material.

Given the poor quality of the transverse field magnetostrictive results, the longitudinal magnetostriction measurements must also be viewed with skepticism. One lesson in particular which can be taken from the magnetostrictive work is that a small sample must be extremely well anchored.

5.4 Discussion and Conclusions

Despite some experimental issues, the dilatometric investigation of $Tb_2Ti_2O_7$did produce some intriguing results which warrant further investigation. The feature observed at 100mK should may relate to a phase transition in $Tb_2Ti_2O_7$, and should be revisited. This experiment requires only minor changes before it can be successfully repeated.

The lack of agreement with Ruff *et al.*'s anomalous negative thermal expansion is should also be investigated further. In this regard, we may find some assistance in the Ph.D. thesis of Chapuis [16], who investigated the properties of $Tb_2Ti_2O_7$ and related compounds. One of the conclusions of Chapuis' work is that there could exists sample dependant feature in the specific heat and susceptibility of $Tb_2Ti_2O_7$. This would necessitate a detailed structural study to determine optimal growth rates and environments of $Tb_2Ti_2O_7$ samples. This work could not be efficiently carried out with the facilities available at the University of Waterloo and would need to be left to collaborators with expertise in this field. However there is no reason to doubt the thermal expansion measurements before a magnetic field is applied. Magnetostriction measurements and thermal expansion measurements will be repeated with an improved setup, this will also allow the disagreement with Ruff *et al.* [63] to be investigated further.

It is clear that the experiments carried out using the pumped ^{4}He probe were not entirely successful. The origin of the issues could be related to the sample and mounting technique used. The noticeable differences before and after $Tb_2Ti_2O_7$ has been exposed to a magnetic field suggest that the sample may have shifted a small amount when the field was applied or that $Tb_2Ti_2O_7$ has a history dependant specific heat similar to the spin ice Ho_2- and Dy_2-Ti_2O_7 [32]. Being unable to rule out the sample shifting, it is prudent to repeat this experiment such that

sample movement is not a possibility. The lack of repeatability in the transverse magnetostriction measurements, coupled with the discontinuous shifts as field is applied, support this conclusion.

Finally, the lack of reproducibility between consecutive thermal expansion trials shown in Figure 5.13 caused some concern. This effect was attributed to the disordered nature of both Kapton film and Stycast epoxy. The resolution has been to redesign the dilatometer such that these materials were not present on the axis measured and replaced with appropriate sapphire components. The final result is the dilatometer presented in Chapter 3. This updated dilatometer design shows great improvements over previous designs.

Chapter 6

Conclusions

This thesis has presented 3 major avenues of investigation. The first, being the design, construction, and testing of a high-resolution capacitive dilatometer has been shown to be accurate to within the level of noise in temperature control and other experimental parameters. The dilatometric investigation of the phase diagram of $LiHoF_4$ is the second avenue. This project was successfully completed, leaving the option of further work with this interesting ideal magnetic material. Finally, the study of $Tb_2Ti_2O_7$ produced some interesting results in the absence of an applied field and served to improve design of the dilatometer. With this material, there are also many options of further studies to complete. Future is outlined in further detail below.

Capacitive Dilatometer: Before this project can be considered complete, high resolution thermal expansion measurements of copper or a low thermal expansion material (such as Torlon) should be completed. Existing dilatometers are able to perform absolute thermal expansion measurements to within approximately 10^{-7} [71]. This test will determine the uncertainty of the dilatometer and allow for determination of absolute thermal expansion measurements of crystalline materials.

$LiHoF_4$: The investigation of the phase diagram of $LiHoF_4$ in an applied transverse magnetic field using capacitive dilatometry significantly improved the resolution of the critical points near the zero-field transition. These measurements agreed well with existing susceptibility [11] and neutron scattering [62] results, confirming the discrepancy with theoretical predictions [79].

This project leaves several avenues for further investigation. Magnetostrictive measurements in the a-b plane of $LiHoF_4$ can provide information regarding the magnetoelastic coupling in the transverse direction. The quantum critical region has yet to be explored using thermal expansion. The divergence of thermal expansion near a quantum critical region makes this technique ideal for study of $LiHoF_4$ at ultra-low temperatures. Only pure $LiHoF_4$ was studied in this thesis: $LiHo_{1-x}Y_xF_4$ also displays an array of interesting spin glass behavior as Ho^{3+} ions are replaced [58].

$Tb_2Ti_2O_7$: The questions raised during the $Tb_2Ti_2O_7$ investigation lead to a redesign of the dilatometer, yielding the tool presented in Chapter 3. In this regard, the work performed on $Tb_2Ti_2O_7$ was invaluable. In addition, the zero field measurements present an interesting feature at 100mK which should be reinvestigated. The anomalous thermal expansion observed by Ruff *et al.* [63] using X-ray scattering was not observed. This disagreement should be investigated further using a larger sample, and by performing measurements along multiple axes of $Tb_2Ti_2O_7$.

The evolution of thermal expansion in an applied field could be indicative of the ordered phases observed by Cao *et al.* [13] and Rule *et al.* [66]. Most illuminating here would be thermal expansion measurements in an applied field, beginning below 100mK and tracking the effects from ultra-low temperatures to higher temperatures.

Appendix A

Dilatometry How-To

This section aims to provide a ”How-to” manual for capacitive dilatometry measurements in Prof. Rob Hill's lab at the University of Waterloo. This appendix contains details regarding the assembly, characterization, and use of a dilatometer similar to or made from the drawings in Appendix B using the equipment and programs available in the aforementioned lab. It has been written for future students undertaking work which uses this capacitive dilatometer and so contain many details pertinent only to the University of Waterloo Physics department facilities.

This appendix assumes that all the components have been fabricated according to the drawings in Appendix B. Science Technical Services (STS) possesses an incredible depth of experience and skill, the availability of which is an invaluable resource which should not be overlooked. As of this writing, Mike Lang has fabricated 3 dilatometers and is a very skilled machinist. Given an option, he is probably the best person for the task.

A.1 Assembly

This section describes the assembly of the dilatometer, after all components have been fabricated.

After fabrication, there is still a fair amount of work to be completed before a functioning dilatometer is ready. This section will describe the assembly of these components, characterization of a dilatometer is left to the next section. Figure A.1 is repeated from Chapter 3 to provide a convenient reference for the names of components.

The first step in assembling the dilatometer is to epoxy the lower assembly together. Stycast 2850 epoxy is the tool of choice in this instance: when used with Catalyst 23LV, the thermal expansion of Stycast is closely matched with copper over a large range of temperatures. Stycast is a polymer, as such the thermal expansion of Stycast may not be repeatable to the level of precision possible with a carefully assembled dilatometer. Where Stycast is used, it is important

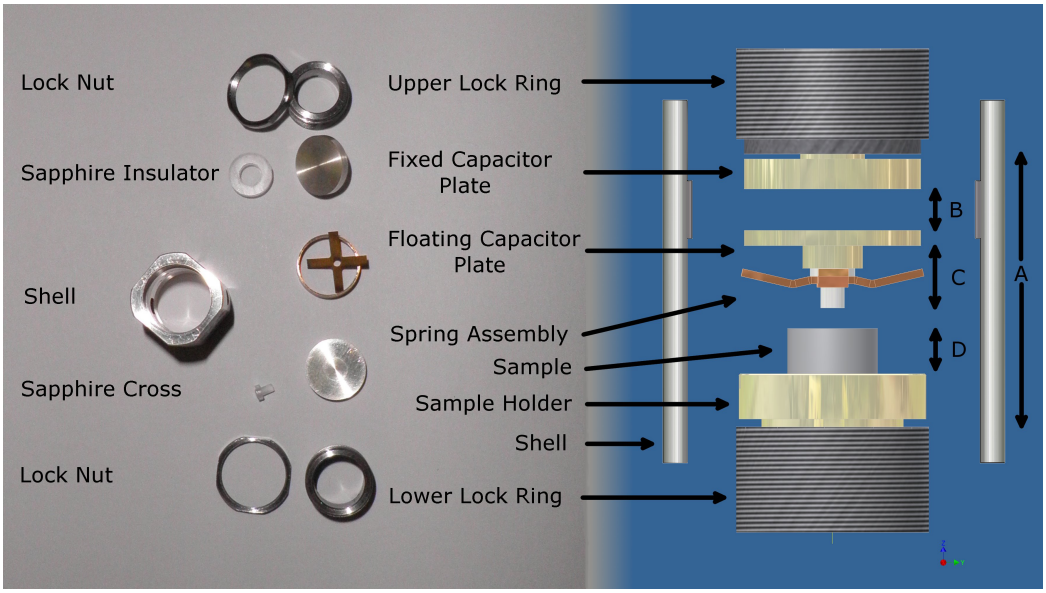

Figure A.1: Repeated from Chapter 3. Left: A photograph of an unassembled capacitive dilatometer. Right: Schematic of the dilatometer. The shell is a silver rod in which a cylindrical bore through its length maintains coaxial alignment of all other components and provides a ground plane around the capacitor plates. Both ends of the shell are threaded at 3.14 turns per millimeter. The upper lock ring threads into the silver shell and controls the position of the upper capacitor plate. The lower capacitor plate is anchored to the spring via a sapphire cross. The sample is then pressed against the sapphire cross, depressing the spring to maintain contact between the sapphire cross and the sample. The sample is mounted to the sample holder via silver paint or silver epoxy. The sample holder is held in place with the lower lock ring. The lower lock ring threads into the silver shell. Ultimately, the lower lock ring can be threaded in or out of the shell to control the spring deflection and position of the sample.

to avoid using large amounts and to create a radial bond (relative to the $\hat{z}$ cylindrical axis of the shell) between components which will have a smaller impact on thermal expansion.

The lower assembly consists of the fixed capacitor plate, the large sapphire insulator, and the lower lock ring. These components should be tightly slip fit to each other. In addition, Stycast epoxy and two pieces of the thickest Kapton film available will be used. Begin by mixing a batch of Stycast, and apply a small amount to the inside of the sapphire washer. Press the washer onto the post on the rear of the fixed capacitor plate and wipe away any excess Stycast. The sapphire washer should be sized such that the tapped end of the capacitor plate is flush or rests above the sapphire washer. Next lay the two Kapton strips on the back of the capacitor plate - these will act as spacers between the lock ring and the capacitor plate and should be large enough to be accessible once the lock ring has been epoxied in place. Apply a small amount of Stycast to the inside of the lock ring, and press the lock ring onto the sapphire washer and capacitor plate assembly. Note that the end of the lock ring with the four semicircular cut-outs should be accessible after assembly. Allow the Stycast to cure, either by leaving it in a cool, dry place for 24 hours, or put it in the furnace at 65°C for 4-6 hours. A good habit is to include a sample of the same batch of Stycast and subject it to the same curing process as the dilatometer components. This extra Stycast sample can be used as verification that the epoxy has cured. When Stycast is fully cured, it is hard enough to machine and the surface can only be scratched with a razor blade.

The next step is to polish the surface of the capacitor plates. This is the most painstaking part of the entire process, and must be done **very** carefully. You will need multiple sheets of 600-1200 and 1500 (or higher) grit sandpaper, masking tape, a couple mirrors (found in Phys 333, one for each of the sandpaper grits), the polishing apparatus also found in Phys 333, crystal bond or super glue, the top of the fixed plate test jig (the plate with the threading for the fixed lock ring), latex gloves, a bit of water or colloidal polishing fluid, and the floating capacitor plate and fixed plate assembly.

First clean the mirrors. Then clean the mirrors again, any grit left on the mirrors will damage the surface of what will ultimately be two mirror-finished capacitor plates. Tape a piece of sandpaper to each mirror, ensuring that it is flat and won't wrinkle. Now fasten the floating capacitor plate into the polishing jig using either crystal bond or super glue. Be sure to clean the mount for the capacitor plate thoroughly, anything left here could tilt the capacitor plate and lead to poor results. Once mounted, the floating plate is ready to be polished: starting with the coarsest piece of sandpaper, pour some water or polishing fluid on the sandpaper and move in slow figure 8's. You may need to press gently down on the polishing post (using an Allen key or similar) to maintain contact between the capacitor plate and the sand paper. Once the surface has reached a uniform roughness, move to the next finer grit of paper and repeat this process. Check the finish every 8-10 figure 8's, and avoid using coarse grit for too long. Silver is a soft material, it is possible to grind away the plates quickly. On the last and second last stages do not use polishing fluid, and wear latex gloves. The grit is fine enough to permeate skin and is certainly

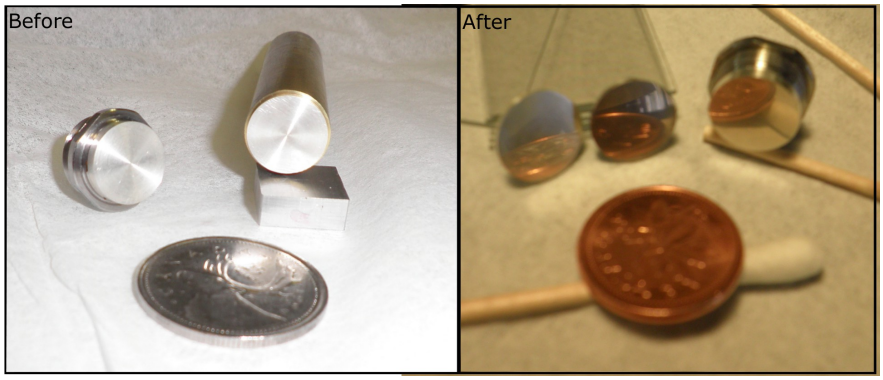

Figure A.2: Before and after pictures of the capacitor plates being polished. Left is before the plates have been polished, right is after the plates have been polished. A penny is included in the foreground, note the clarity of the reflections.

not something which should be ingested. As this fluid dries it leaves a precipitate behind which will scratch the surface of the capacitor plates. Once a mirror finish has been achieved (estimate 4-6 hours, depending largely on luck and patience) the adhesive can be removed with acetone.

The fixed plate can be mounted in the top of the fixed plate test jig. Screw in the lock ring until the fixed capacitor plate just protrudes from the jig. Use a lock nut to firmly fasten the fixed assembly in place, then repeat the polishing process as it was done with the floating plate. It may be necessary to replace some of the pieces of sandpaper, if they have been worn out. Figure A.2 shows before and after pictures of the capacitor plates. It is difficult to describe how important this step is: small surface blemishes on the capacitor plates will lead to low C_{max} values and a corresponding lack of sensitivity in measurements. If the plates are not mounted properly in the polishing jigs, the plane of the capacitor will be tilted with respect to the cylindrical axis of the dilatometer, which will wreak havoc on setting up the dilatometer and performing measurements. It is well worth the time to perform this task well.

The next step is to fasten the electrical leads to the capacitor plates. The fixed plate simply presses a wire against the rear of the plate using a screw. The screw used here should be brass, PEEK plastic or teflon. Ignore what people may tell you, A304 stainless steel (the most common form of stainless) becomes magnetic after repeated thermal cycling and exposure to high magnetic field and should not be used. The electrical lead on the floating plate capacitor is fastened in place using Epotek silver epoxy H20E Parts A and B. Mix Parts A and B in equal amounts by mass. Strip the end of a thin wire and wrap it around the post on the back of the capacitor plate. It is helpful to coil the wire in a slightly smaller diameter than the post such that it will squeeze the capacitor plate. Use a small amount of epoxy uniformly around the post to provide mechanical and electrical contact between the wire and the post. Place the capacitor plate on a glass slide and onto the hot plate (set to 4), and allow the epoxy to cure for 15 minutes. Allow

to cool, then check continuity between the wire and the capacitor plate. If necessary, methylene chloride can be used to quickly remove the H20E epoxy. Use a minimal amount on a Q-tip, methylene chloride will blemish silver surface.

If the cross spring is being used, bend the spring. There is a small jig to assist this process, consisting of a tapped 5.35 mm square post, and a small 2 mm square rod with a clearance hole. Bend carefully (the sharp edge of a razor blade works well), and double check afterwards that the spring fits into the spring ring nicely. Symmetry is important in this step: if the spring is off center it will also pull the floating capacitor plate off center. Stycast should be used to bind the spring into the spring ring.

The floating plate is now ready to be epoxied in place. Begin by threading in the fixed capacitor plate to the shell. Cut one or two rectangular strips of Kapton film long enough to wrap around the circumference of the fixed capacitor plate, and wide enough that they sit slightly above the surface of the fixed capacitor plate when they are wrapped around the capacitor plate sitting in the shell. Use the thickest Kapton film possible for this step. Place another piece of 100 μm thick Kapton film on the surface of the fixed capacitor plate, then set the floating capacitor plate on the fixed plate. Drop the spring into the shell, and adjust the fixed plate such that the spring rests firmly against the shoulder in the shell and there is enough room on the top of the capacitor plate to fit the sapphire washer. The window in the spring should be visible through the window in the shell.

Once everything is set in place, lock the fixed assembly in place using a lock nut. Drop the sapphire pin into the hole on the back of the floating capacitor plate and apply a minute amount of Stycast at the top of the floating capacitor plate to hold the sapphire pin in place. Coat the inside of the sapphire washer with Stycast and place this on the sapphire pin. Set the spring back into place - the sapphire pin should just protrude from the spring. Apply a small amount of Stycast around the pin on the spring. Finally, let the epoxy cure.

Finally, single pin connectors can be soldered to the ends of the leads. Congratulations, it is now time to test the newly assembled dilatometer!

A.2 Characterization

This section outlines the methods used to characterize an assembled dilatometer. Much of the process here is similar to that presented by Schmiedeshoff *et al.* [71]. There are three measurements to be made, testing the linearity of capacitance with respect to rotation, the linearity of capacitance with respect to spring deflection, and the cell effect.

The linearity with respect to rotation refers to the linearity of capacitance as the fixed plate is screwed further into or out of the shell. We know:

$$g = \frac{\epsilon_0 A}{C}\left[1 + \frac{C^2}{C_{max}^2}\right] \tag{A.1}$$

Where g is the gap between the plates, ϵ_0 is the permittivity of free space, A is the effective plate area, C is measured capacitance and C_{max} is the maximum capacitance. At this stage the dilatometer has just been assembled, so the effective plate area and C_{max} are unknown. This test will determine both of these values. The first step is to setup up the dilatometer in the linearity test setup, with a silver or copper sample gently pressed against the spring and monitoring the capacitance with the AH2500A. The linearity test setup uses a stepper motor to rotate the fixed plate by a controlled amount, and is controlled by the Labview program "Dilatometer_Control.vi" on the computer Supercold. The stepper motor creates some vibration as it rotates, at this stage the sample is being used to maintain the position of the floating plate assembly in the dilatometer.

Set an initial low capacitance (ie: 3 pF) by hand, and remove the lock ring from the fixed plate assembly. Using the Dilatometer_Control.vi you can set the step size in degrees, and the desired capacitance. When dialing in, the programs monitors for "Excess Noise" and "Indeterminate Offscale" warnings, and so will stop automatically when the capacitor plates come into contact. Set a step size for 2°, make sure the program is set to rotate in and the file name is descriptive and press "Run". This will begin rotating the fixed plate inwards, and generate a data set similar to Figure A.3.

An alternative setup is to screw in the fixed plate until the capacitor plates short, and to use the Dilatometry control program to dial out the capacitance. This is largely a matter of personal preference, both experiments give the same results.

The analysis is straightforward. Beginning from $g = \epsilon_0 A/C$, the fixed plate is screwed in by some amount θ. Knowing that the lock ring is threaded at 80 turns per inch, or 3.14 turns per mm we can convert this rotation into a change in the position of the fixed plate via $\Delta D = \beta\theta$. β is a constant which converts rotation in degrees to motion in nanometers, β = 884 nm/deg. Then the linear portion of the line in Figure A.3 can be fit with $1/C = (\beta/\epsilon_0 A)g$, and A can be calculated from the slope. The effective plate area A is a characteristic of the dilatometer, and only needs to be measured once. The Labview program automatically records the highest value of capacitance measured, this value can be used as C_{max} for the linearity with respect to spring deflection test.

The next step is to repeat this process using the copper or silver sample to deflect the spring of the floating capacitor plate assembly by 100 μm. This is more like a typical experimental setup. The value of A determined here should be used in all subsequent analysis.

The second characterization test is linearity with respect to spring deflection. This test is much closer to an actual experimental trial, and gives a better indication of what C_{max} will be from run to run. Set the dilatometer such that the plates are approximately 200 μm apart, and tighten a lock nut on the fixed capacitor plate to maintain its position. Load a copper or silver

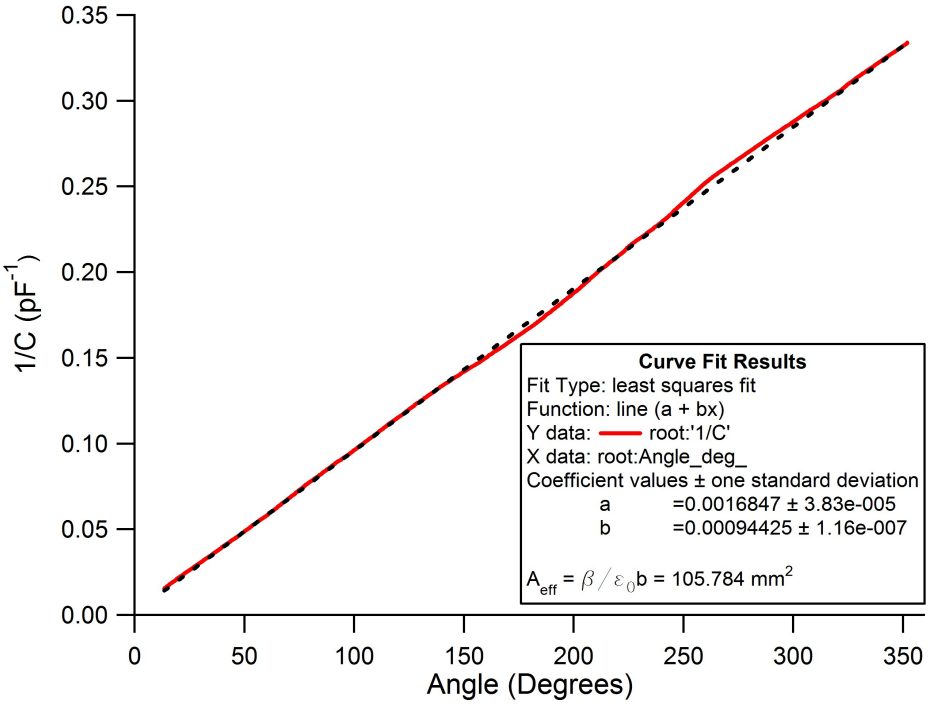

Figure A.3: Linearity of a dilatometer, with respect to rotation. Main: 1/C vs θ. The slope of these lines are proportional to the effective plate area, A. Inset: d/dθ(1/C) (left axis, black) and 1/C (right axis, blue) vs point number, roughly proportional to time. The effective plate area A can be calculated from the slope of 1/C vs θ, and C_{max} read off from the highest measured capacitance.

sample into the dilatometer such that the upper lock ring is set in the threads, but only the weight of the sample is depressing the spring. Lock the sample holder in place using a small Allen key, tweezers, or the small steel "L" keys. It is good practice to record this data with any of the Labview programs available.

Begin dialing in the upper lock ring, and take note of the position when the upper capacitor plate begins to be deflected (as seen by a change in capacitance). There are 12 evenly spaced marks on the top of the lock ring, these can be used for fairly even 30° rotations. Dial in the upper lock ring until the capacitor plates short, and take note of C_{max}. Plotting and fitting this data as in Figure A.3 will give a good indication of the behavior of the dilatometer as a sample expands. If this is done carefully the effective plate area can be extracted from this data, however unless C_{max} is unusable (smaller than 20 pF) then the value of A determined here will probably agree well with the value determined previously. To do this test well by hand is more labor intensive than letting the linearity jig perform the same task, with little payoff.

Finally, it is time to measure the cell effect of this newly assembled dilatometer. The cell effect is simply the response of the dilatometer when a silver sample is used, and is best done in conjunction with experiment. Experimental method is discussed in the following section, and so will be omitted here. What is important about the cell effect is that it be done as carefully as the experiment, and that capacitance is matched as closely as possible with the experiment. Recall Equation 3.3 from Chapter 3, in order for the last term to vanish B_{Ag} and B_{Sample} must be approximately the same.

A.3 Experimental Method

This section describes the experimental method used in a typical experimental trial of the dilatometer. This section focuses on the dilatometer only; the "Practical Cryogenics" handbook available in Phys 130 provides reasonably well written instructions on transfer of cryogenic liquids, safety, thermometry and other matters of interest. The pumped helium-4 probe has been discussed in N. Rahimi's thesis [59] and the dilution unit is discussed in I. Alkesho's thesis [4], these documents can be consulted for details on either of those systems.

A.3.1 Dilatometer Setup

The dilatometer has now been fabricated, assembled, and tested. Now it's time to actually use some helium and gather some data. Setting up the dilatometer will become routine, however the first few uses tend to provide some challenges. This section will hopefully provide some direction to improve the user's experience.

First, we need to mount the sample under investigation. The standard sample mount included in the drawings in Appendix B is rarely the ideal design for a sample and will usually need to be modified to fit the sample more tightly. The key parameter that must be respected is that the length from the outwards step of the sample holder to the end of the mounted sample is long enough to reach the spring, and has some extra length ($\approx$ 1 mm is sufficient) to deflect the spring, but is not so long that the lock ring does not thread into the shell. This length is usually 6 mm, however it can vary between different dilatometers and upon reassembly, and should be checked.

Mounting samples is not difficult, only requiring patience. With the appropriate (probably freshly fabricated) sample mount in hand, position the sample such that it is in the middle of the sample holder. Either of the silver Epotek epoxy or the silver paint can be used to mount the sample. The epoxy is much more robust and dries more quickly than the paint, however is much more difficult to remove and can damage the sample if the sample is strained. The paint is softer and easier to remove, however it must be left for 24 hours to dry after being applied. Using your bonding agent of choice, apply enough to hold the sample in place on the sample holder. Let the epoxy or paint dry, then begin assembling the dilatometer.

The distance the spring is deflected and the working capacitance are the two parameters which must be chosen for each experiment. A typical spring deflection for a robust sample is 100 μm. This deflection will usually maintain contact between the spring and the sample without applying a large amount of pressure to the sample. Depending on how robust a sample is you may choose to use a different spring deflection. A larger spring deflection could risk damaging the spring if the sample's thermal expansion is significantly larger than silver, while a lower deflection may lose contact with the spring. With new samples it is difficult to determine what the case may be, one useful trick is to apply a tiny dab of vacuum grease to the end of the sample when it is pressed into the spring, and to apply a lower (50 μm) spring deflection. Vacuum grease will freeze and bind the sample and spring together.

The working capacitance defines the sensitivity of measurements, and should be kept to less than 50% of C_{max}. The working capacitance must also be large enough to accommodate the response of the material under study. For example, during preliminary measurements of $Tb_2Ti_2O_7$'s magnetostrictive response, the working capacitance was too close to C_{max}. When a sufficiently large field was applied $Tb_2Ti_2O_7$ expanded enough to electrically short the plates. Additionally, when the dilatometer entered the non-linear region of capacitance there was a discontinuity in the magnetostrictive response, generated entirely by a poor experimental setup. This caused short-lived excitement, swiftly crushed when the error was identified. A reasonable first approximation is 100 μm spring deflection and 12.5 pF working capacitance if C_{max} is greater that 30 pF. The first cool down of a new sample will probably not be publishable data, and these values can be tweaked on subsequent thermal cycles.

The easiest way to set up the dilatometer is by setting it on the lab bench or desk, such that the cylindrical axis is vertical and the face of the floating capacitor plate is pointing towards the bench. If the pumped ^{4}He probe is being used the dilatometer can be mounted in the fork, if the

dilution unit is being used it can be placed in the copper clamp used to fasten the dilatometer to the mixing chamber and held upright with a vice grips. Begin by connecting the dilatometer to the AH2500A capacitance bridge, then dialing in the fixed plate such that capacitance is between 3-6 pF and locking the fixed assembly in place.

Setting the sample and the appropriate plate deflection is the next step. Before putting the sample into the dilatometer a thermistor and a thermal link (approximately 35 mm of copper or silver wire) should be mounted to the rear of the sample holder using a brass or teflon screw. The thermistor will be used to check thermal stability of the sample during an experiment, the thermal link improves the thermal contact between the sample and the cold stage. Ensure that the thermal link is pressed firmly between the thermistor and the sample holder, and that the thermistor is placed such that the lock ring can be fit onto the back end of the sample holder. The sample holder can now be placed into the dilatometer, and the upper lock ring threaded into the shell.

The next step is to set the spring deflection by screwing the upper lock ring into the shell. We do not wish to grind the sample against the spring, so a small Allen key or a stainless key should be inserted into the cut out in the sample holder through the window of the shell. This will hold the sample holder in place as the lock ring is turned. Calculate the plate separation from the initial capacitance and the capacitance when that spacing has been reduced by 100 μm, and screw in the upper lock ring gently until the desired spring deflection is achieved. Hold the upper lock ring in place and tighter a lock nut to hold the lock ring in place.

The difficult half of the dilatometer setup is now completed. The maximum value of capacitance (C_{max}) should be checked before every trial, this is our next task. Loosen the lock nut on the fixed assembly, and begin slowly screwing in the fixed assembly while watching capacitance. Continue screwing in the fixed assembly until capacitance shorts and take note of the final observed capacitance. This final capacitance value will be used as C_{max}. The fixed assembly can now be unscrewed until the desired working capacitance is reached then locked in place with a lock nut.

If C_{max} is too low for the desired working capacitance it may be possible to improve it by spinning the sample in the dilatometer, if the rotational orientation is not important. Loosen the upper lock ring and spin the sample until a minimum capacitance is reached, then apply the desired spring deflection and test C_{max} again. If this is unsuccessful the spring can also be rotated. If C_{max} remains unacceptably low then the sample may need to be modified or the dilatometer reassembled.

Once the dilatometer is setup, connect and test the thermistor and dilatometry communication lines. The setup is now complete!

A.3.2 Running an Experiment

Gathering data has been automated via Labview. These programs are all similar in operation, for clarity the discussion will focus on the use of "Dilatometer_HillMagnet.vi". Figure A.4 shows a screen capture of the front page of this program. This program runs on a timeout scheme - after the program is started a timer countdowns. When the timer reaches zero a measurement is taken, and the timer begins again. The value the timer takes initially is the "milliseconds to wait" value, shown top right of Figure A.4. While the program is running it will record time, temperature, capacitance, magnetic field and magnet current, and resistance in a ".cap-log.dat" file. The final tab labelled "PID" contains the temperature control for an experiment, shown in Figure A.5.

PID control uses three values to reach a stable setpoint temperature (the column labelled "Temp (k)"), proportional (P(%)), integral (I(%)) and derivative (D(%)). These three values control how much heat is put into the system via the expression below [43]:

$$Q = P\Big[e + I\int e \cdot dt + D\frac{de}{dt}\Big] \tag{A.2}$$

Where P, I, and D are as defined above, e is the setpoint temperature minus the actual temperature and t is the temperature. Roughly speaking, P controls the amount of heat applied, I will continue to apply heat until the system reaches the setpoint temperature, and D will slow a rapidly changing system to reduce the any overshoot of the setpoint temperature. While it is possible to derive PID settings from the thermal mass, setpoint, and thermal load of the system it is much simpler in practice to determine these values through trial and error. A good scheme is provided in the Lakeshore temperature controller manuals found in Phys 130. Tables of PID values for the pumped ^{4}He probe and the dilution unit are included at the end of this section. These will change if any aspect of the refrigeration system is changed.

The final two columns in the PID tab, "Range" and "Timeout" control the maximum heat which can be applied and the length of time of each PID step, respectively. "Range" can take on a variety of values depending on the temperature controller being used, it is best to check each controllers manual for these values. "Timeout" is the total time for each step.

There are two important values in Figure A.4 which have not been discussed: "# to Avg" and "Settling time", shown top right. These are intuitively obvious, controlling the number of data points to average and write to a data file and the length of time to wait after a PID step change before beginning averaging. These are used slightly differently depending on the type of temperature control (dynamic or quasistatic) used. A dynamic experiment rarely changes PID values but is continually changing the setpoint temperature. As a result the system is continually changing, the "# to Avg" controls how often average points are written and so controls the resolution of data. If set too low, then resolution will be very high and the white noise present in

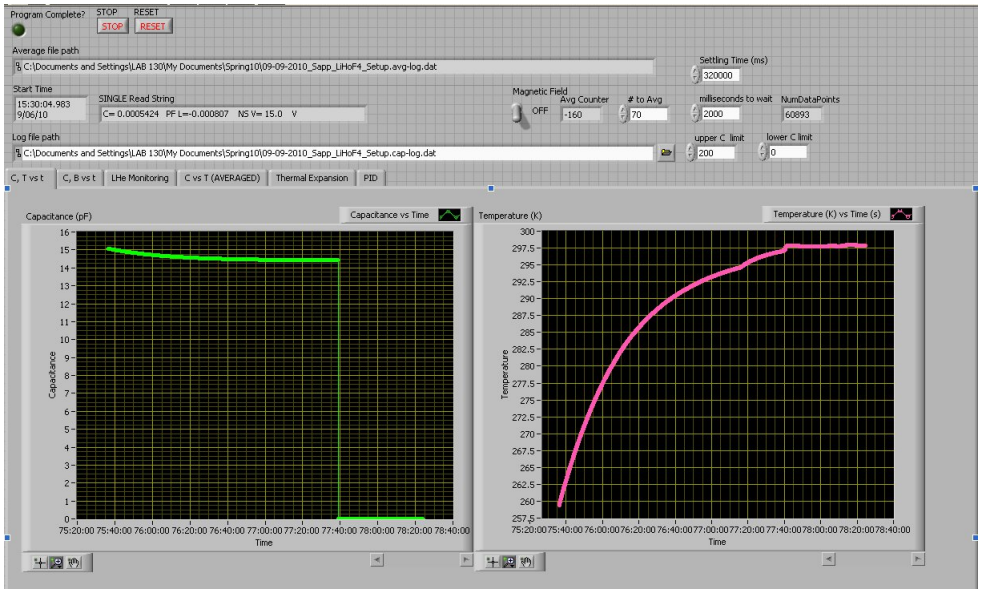

Figure A.4: Labview program used to collect data and control temperature.

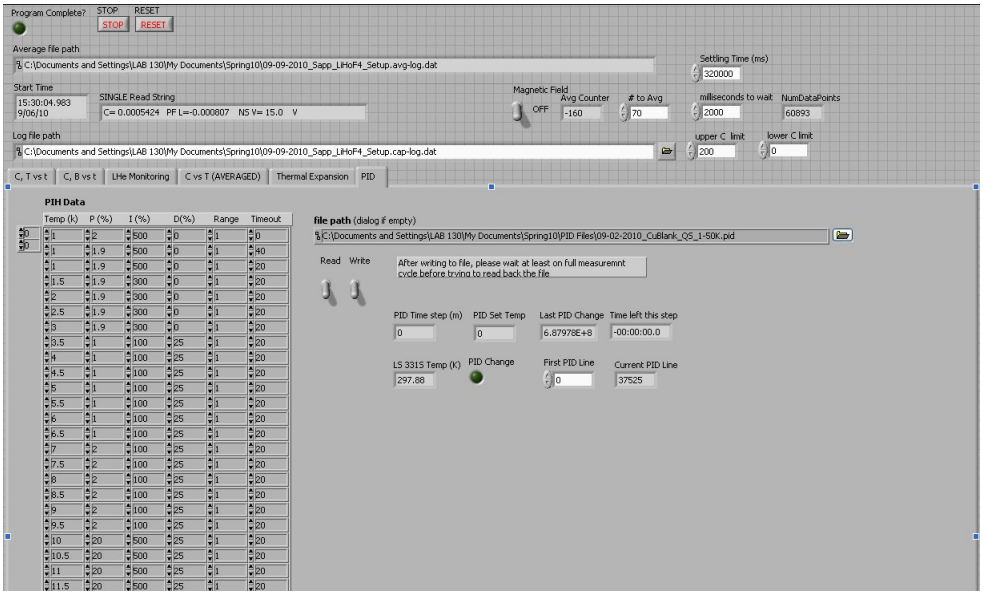

Figure A.5: PID tab of the Labview program, used to control the temperature.

any experiment will appear in the averaged file. If "# to Avg" is too high then there will be low resolution in the averaged file and features may be missed. "Settling time" is used to eliminate data just after a PID change where there are significant discontinuities in temperature which add large delta-function like spikes to temperature.

A quasistatic experiment changes the setpoint often, and waits for the system to settle at that temperature. In this case the "Settling time" allows the system to come to thermal equilibrium, then the "# to Avg" begins averaging points. An important point is that if the "# to Avg" is not complete when the PID timeout ends then the averaged value is discarded and not recorded. Hence, an important subtlety to this program lay in setting each of these values, and how they are each tracked. The "Settling time" is a misnomer, the value "Settling time" is divided by "milliseconds to wait" and this number of points is ignored before beginning averaging. The problem with this scheme is that communication with the instruments takes anywhere between 0.5 to 2 seconds. This time depends largely on the Average Time value set in the AH2500A bridge. Care must be taken to ensure that settling time and the # to average are set such that the system reaches equilibrium, and a sufficient number of points are averaged to reduce noise to a manageable level. One good technique is to account for an extra 0.5 s on each measurement and allow an extra half of the averaging time in the setpoint. For example, if the PID timeout is 20 minutes and "milliseconds to wait" is 1500 ms, we want to settle for 13 minutes and average 5 minutes which leaves 2 minutes of extra time. We will account for 2 s per measurement, and so set "Settling time" to ignore $13 * 60/2 = 390$ points, or 585 000 ms. "# to Avg" simply counts the number of points, so we will set this to $5 * 60/2 = 150$ points. This will allow for 2 minutes of extra time.[1]

Now that we have an understanding of the Labview program, we can discuss what is required for a successful experimental trial. Before running an experiment, there are five things which must be set for a successful trial: file name, settling time, number of points to average, the time-out between measurements, and the PID settings which control the temperature. The file name should be set to something with provides enough information to identify the specific experiment performed and ending in ".cap-log.dat". The amount of information varies greatly, at times only the date, material and temperature range is required, in other instances the date, material, orientation, applied field and field orientation, temperature and temperature control are all required. Use your own judgement, and assume that you will come back to this data set sometime in the future, after you've forgotten everything about it.

The PID setting can be entered into a comma-separated file, where each line is a line in the PID table shown in Figure A.5. This file can be selected using the "file path" entry in the PID tab, shown in Figure A.5. It is important to include only the PID values in this table, if a spreadsheet program is used to create the PID file to double check that each entry is a number (in place of an

[1]The author recognizes this is convoluted, backwards, and altogether quite silly. This program is badly in need of being rewritten, however in the spirit of "it's not broken, don't fix it" this has yet to be done.

expression, ie: above line + 0.5 K). It is advisable to double check the rate date points are being collected, and to adjust ”Settling time” or ”milliseconds to wait” if necessary.

If one of the superconducting magnets is being used, switch the ”Magnetic Field” to the On position. This will record the value of the current being supplied to the magnet by the IPS-100 magnet controller, and convert this current into an applied field. Note that if the magnet has been set persistent then this will read 0, despite the obvious falsehood of that statement. There are two programs which look identical, ”Dilatometer_HillMagnet.vi” and ”Dilatometer_OxInstMagnet.vi”, but the conversion from current to magnetic field is set for the 9T magnet in the thin cryostat which sits on the floor and the Oxford Instruments magnet in the cryostat which rests in the pit, respectively.

There is no software control set up for the magnet controller, it is not advisable to control a superconducting magnet remotely unless you are very certain of what is being done, or there is idiot-proof software interlocking to prevent any accidental quenching of the magnet. Neither of these were deemed realistic when the magnet control programs were last revised, so magnet control remains completely manual.

Once everything is ready, press ”Run” and wait for the data to collect. Congratulations!

A.3.3 PID Tables

The table below shows the PID values which are currently in use for a dynamic temperature sweep in the pumped ^{4}He probe.

$T_{initial}$	T_{final}	P	I	D	Range
1	3	1.7	500	0	1
3	8	3.5	300	0	1
8	20	25	500	0	1
20	50	12	120	75	2

The table below provides PID settings when performing quasistatic temperature control using the pumped ^{4}He probe. These were determined with the needle valve open approximately 1 division, and submerged in liquid helium.

Tinitial	Tfinal	P	I	D	Range
1	3	1.9	500	0	1
3	7	1	100	25	1
7	10	2	100	25	1
10	15	20	500	25	1
15	20	150	12	75	1
20	30	200	15	75	1
30	35	250	20	75	1
35	40	300	20	75	2
40	50	400	40	75	2

The table below provides PID values for use with the dilution unit, when performing either a quasistatic or dynamic temperature sweep. Note that the status of the Roots pump should be automatically changed by the Labview programs currently in use. If these programs are modified or new programs written, it is important that the Roots pump is not turned on automatically after it has been turned off (for example, after an experiment is finished and the dilution unit is cooled to base temperature). If done automatically, this could overwhelm the pump and create a leak in the circulation lines.

Tinitial (K)	Tfinal (K)	P	I	R	Roots
0.02	0.04	6	30	4	ON
0.04	0.1	6.3	30	4	ON
0.1	0.2	6.3	30	5	ON
0.2	0.4	12.5	15	5	ON
0.4	0.5	30	6	5	ON
0.5	1	30	9	6	OFF

A.3.4 Analyzing the Results

There are two analysis programs written which will do the preliminary analysis converting data to thermal expansion or magnetostriction, usually found in the ”Igor Programs” folder of Lab 130’s Documents on the computer ”Supercold”. Both lack user-friendliness and could benefit from being made into GUI’s.

The first, ”DilatometerThermExpAnalysis.v2.pxt” performs thermal expansion analysis of an averaged file as discussed in Chapter 3. The ”.pxt” extension indicates that this is a program template with a procedure which is run automatically, meaning that when it opens it will begin demanding information. The first window requests the averaged file which contains the data and at most one row of headers at the top of the file and no other text. Select the average file you wish to analyze.

The second window requests the strength of the magnetic field present during the experiment, to be entered in Tesla. The third requests the value of C_{max}, and the fourth the length of the sample in millimeters. The final window requests a file name: the output of this program will be written to the specified new file (or overwrite an old file). The output is a tab-separated file containing the temperature, capacitance, capacitor gap, thermal expansion, and first derivative of thermal expansion with respect to temperature. These values are also plotted when the analysis has completed.

The second programs, "DilatometerMagnetostrictionAnalysis.V2.pxt", will perform magnetostriction analysis on a log file, also presented in Chapter 3. As before, the first window is looking for the data file (subject to the same 'data only' constraint as the thermal expansion analysis). The second window requests the length of the sample, the third C_{max}, and the fourth will write the output to a specified file. The output from this program is a tab-separated file containing temperature, capacitance, capacitor gap, magnetic field, square of the magnetic field, magnetostriction, and first and second derivatives of magnetostriction with respect to field.

With this in hand, it is now up to you to provide more specific analysis to find critical points, chart magnetostrictive behavior, or whatever other wonderful effects can be observed using dilatometry!

Appendix B

Dilatometer Drawings

This appendix contains the schematics for the latest version of the dilatometer, including two versions of the spring assembly. The 2-part spring yields a spring constant roughly 10 times lower than the 1-piece spring. This spring is useful when dealing with delicate samples, or when a response on the scale of hundreds of micrometers is expected. The 2-part spring is not useful during magnetostrictive measurement of magnetic samples or for very careful measurements of absolute thermal expansion. Magnetostrictive tests on $LiHoF_4$ and $Tb_2Ti_2O_7$ samples produced nonsensical results which are thought to arise from torque effects which displace the sample and/or spring by a significant amount. The 2-part spring also uses Kapton and Stycast directly along the measurement axis of the dilatometer which introduces some history dependence in thermal expansion.

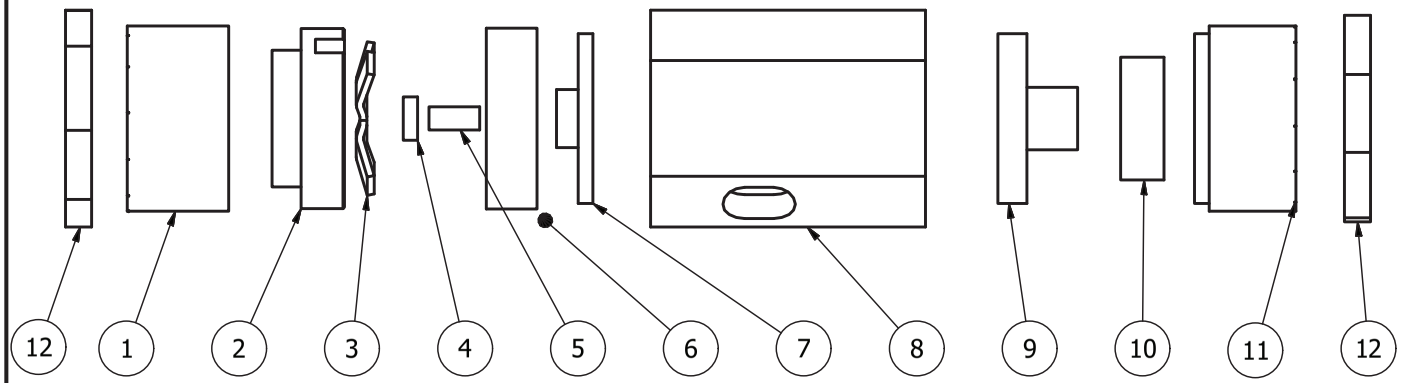

1) Lower Lock Ring
(Stainless Steel A316),
2) Sample Holder (Silver),

Lower Capacitor Assembly: 3,4,5,6,7;
3) Spring (Beryllium Copper),
4) Sapphire washer (Sapphire),
5) Sapphire pin (Sapphire),
6) Spring Ring Mount (Beryllium Copper)
7) Capacitor Plate (Silver),

8) Shell (Silver),

Upper Capacitor Assembly 9, 10, 11:
9) Upper Capacitor Plate - Silver,
10) Insulating Ring (Sapphire)
11) Upper Lockring (Stainless Steel A316),
12) Lock Washers (Stainless Steel A316)

DRAWN John Dunn	11/8/2007	All units in millimeters (mm) throughout. Sapphire components will be provided.
CHECKED		
QA		
MFG		
APPROVED		

TITLE
Compact Dilatometer Overview

SIZE		DWG NO	REV
A		SCD Update 19.05.2010 Drawings	

SCALE 3:1 SHEET 1 OF 14

Same thread as Upper Lock Ring

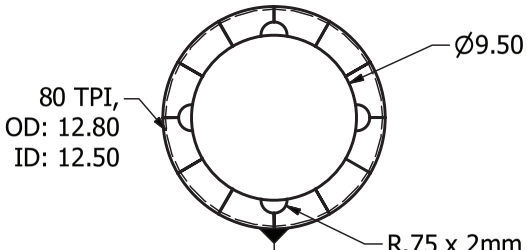

Please include approximately 80 turns/inch threading on outside of ring. Should thread into volume A of Shell.

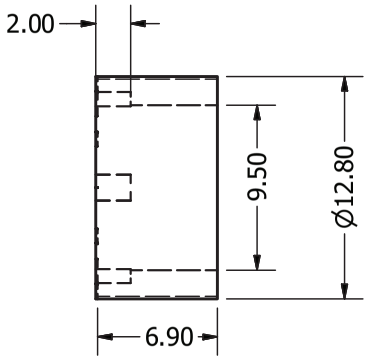

Please include 12 evenly spaced radial marks on top edge of ring

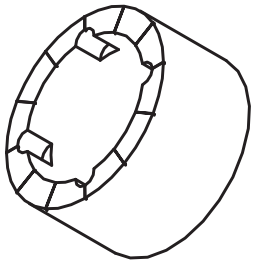

DRAWN John Dunn	11/8/2007	This component to made from Non-magnetic Stainless Steel (A304)
CHECKED		TITLE: Lower Lock Ring
QA		
MFG		
APPROVED		
		SIZE A / 1 / DWG NO SCD Update 19.05.2010 Drawings / REV
		SCALE 3:1 / SHEET 2 OF 14

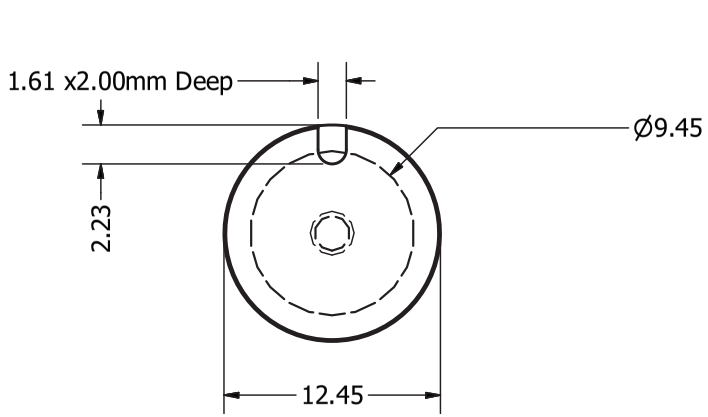

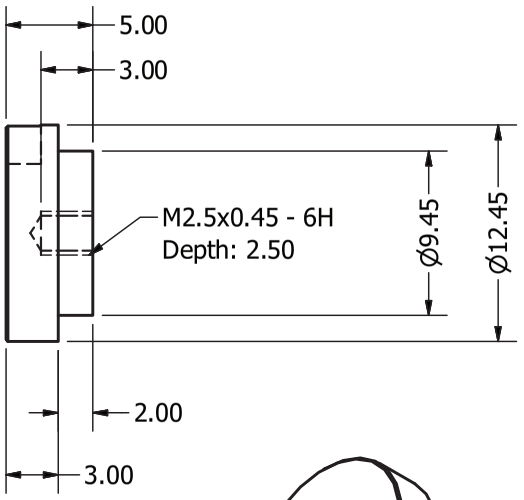

Note: Please include a small chamfer on the top edge, so the sample holder slips into Volume C of the Shell easily.

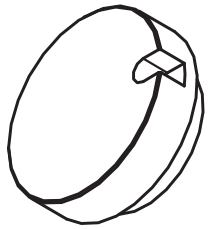

DRAWN John Dunn	11/8/2007	This component to be made from Silver
CHECKED		TITLE: Sample Holder - TbTiO7
QA		
MFG		
APPROVED		

SIZE		DWG NO	REV
A	2	SCD Update 19.05.2010 Drawings	

SCALE 3:1 SHEET 3 OF 14

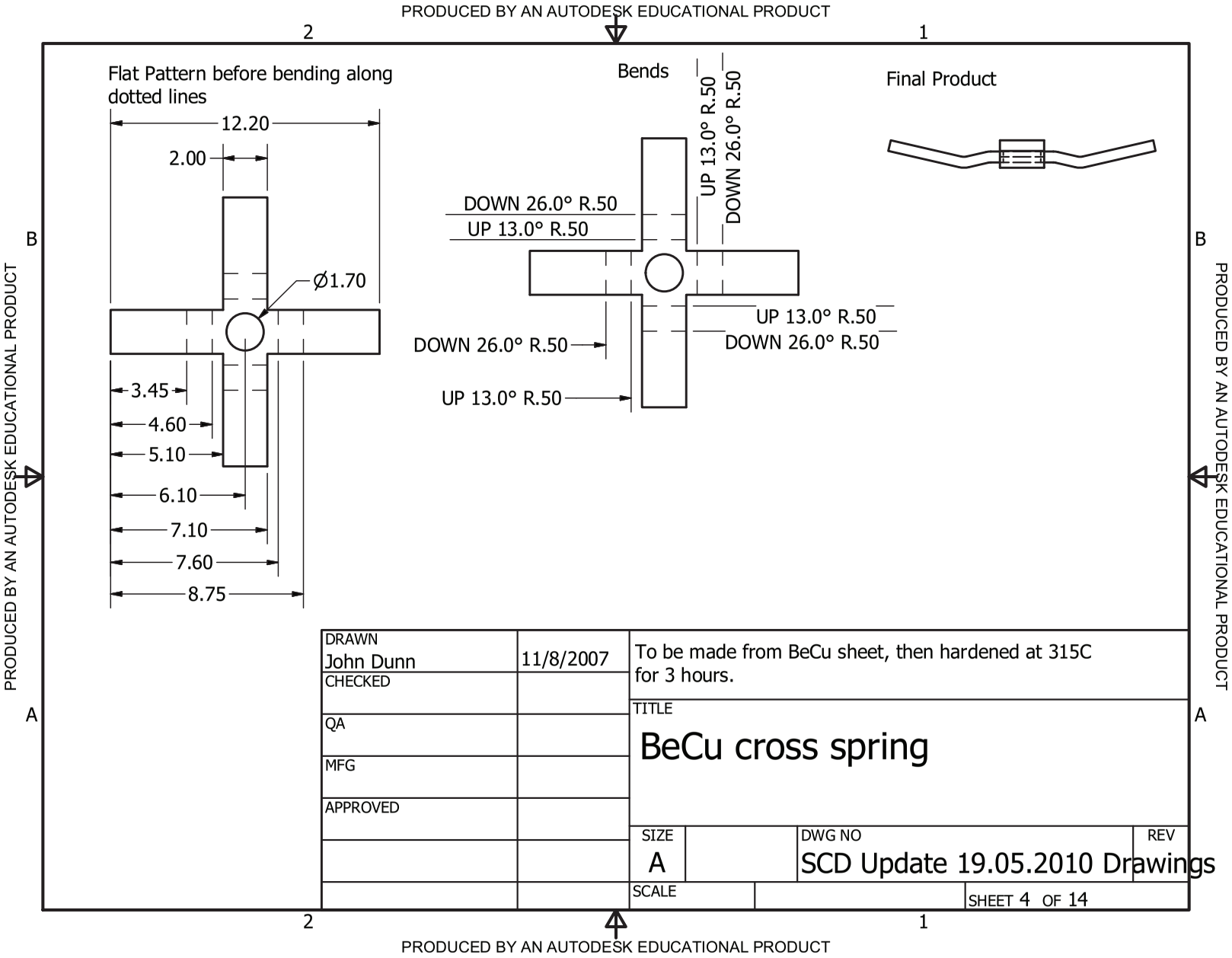

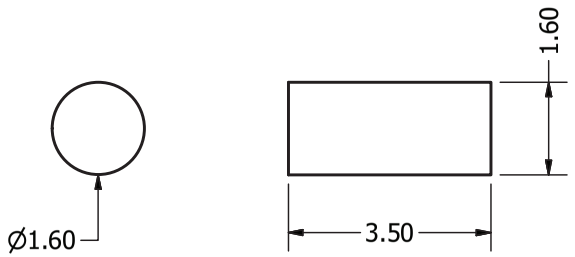

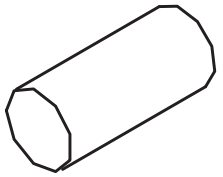

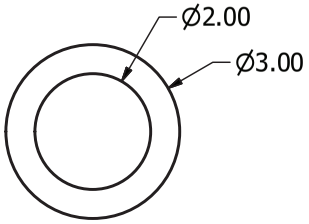

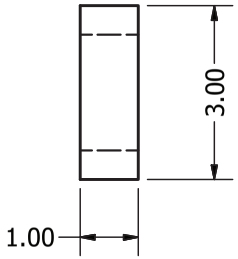

These components will be provided.

DRAWN John Dunn	11/8/2007	Dimensions are approximate, and should be taken from pieces provided.
CHECKED		
QA		TITLE: Sapphire Rod and Washer
MFG		
APPROVED		
SIZE A		DWG NO: SCD Update 19.05.2010 Drawings
SCALE		REV
		SHEET 5 OF 14

SECTION C-C
SCALE 4 : 1

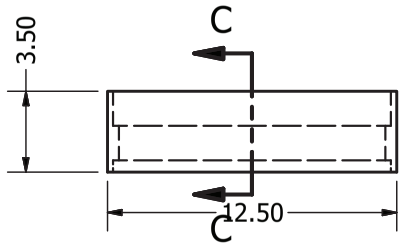

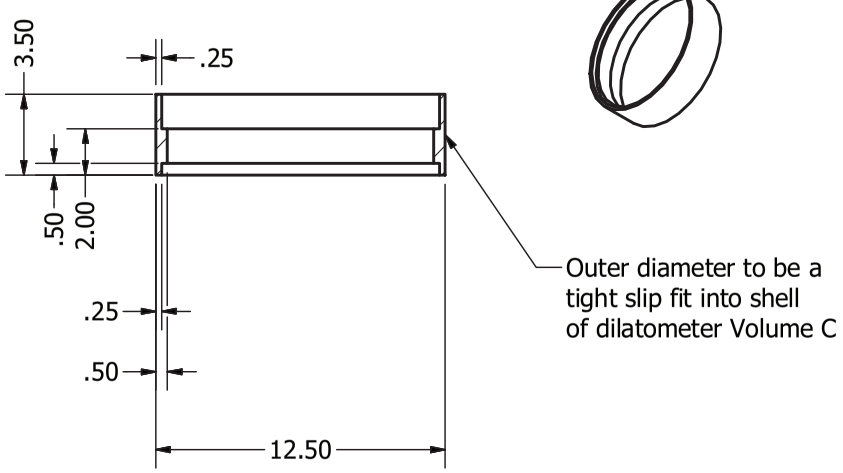

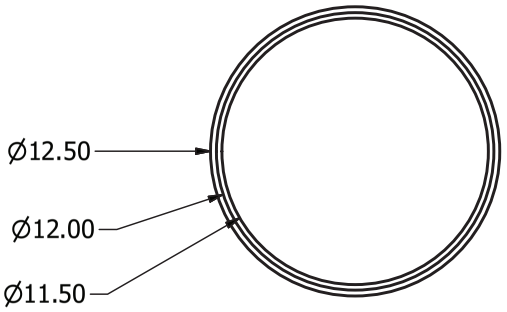

Note: Floating Capacitor Plate must sit inside 12.00mm diameter without making contact with edges.

DRAWN John Dunn	11/8/2007	This component to be made of BeCu
CHECKED		
QA		
MFG		
APPROVED		

TITLE
Spring Ring Mount

SIZE		DWG NO	REV
A		SCD Update 19.05.2010 Drawings	

SCALE 4:1 SHEET 6 OF 14

PRODUCED BY AN AUTODESK EDUCATIONAL PRODUCT

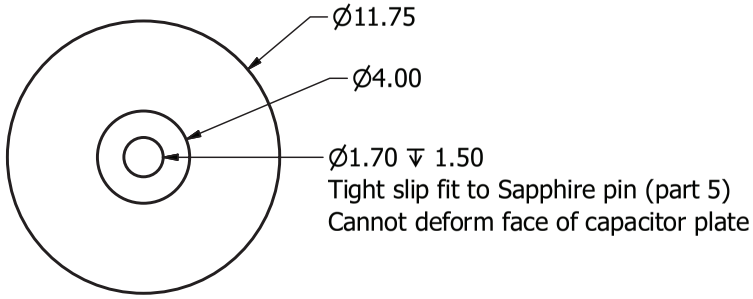

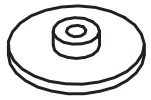

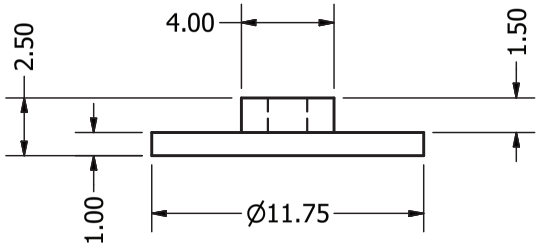

Note: 11.75mm diameters of Upper and Floating Capacitor plates must be as close to identical as possible.

Note: Floating capacitor plate must sit inside Spring Ring Mount 12.00mm diameter without making contact with edges.

DRAWN John Dunn	11/8/2007	This component to be made from Silver
CHECKED		TITLE: Floating Capacitor Plate
QA		
MFG		
APPROVED		
		SIZE A / DWG NO SCD Update 19.05.2010 Drawings / REV
		SCALE 4:1 / SHEET 7 OF 14

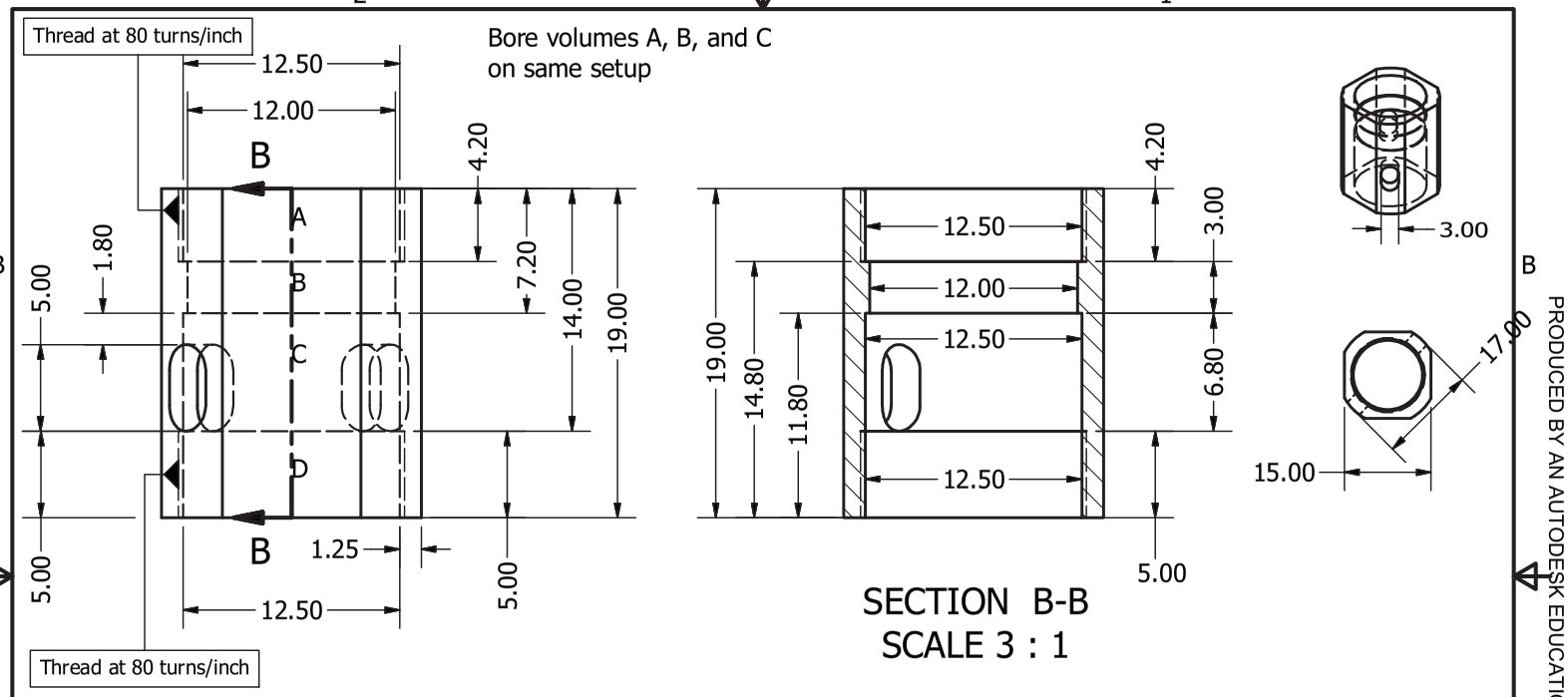

Please thread 12.5mm diameter holes in volume A and D with 80 turns/inch threading inside

Lock ring must thread into Volume A
Spring must be slip fit into Volume C, resting against the shoulder between volumes B and C
Sample Holder must be slip fit into Volume C
Lock ring must thread into Volume D

DRAWN	John Dunn	11/8/2007
CHECKED		
QA		
MFG		
APPROVED		

This component to be made from Silver.
Please modify existing Shell (provided) to match these dimensions.

TITLE: Shell

SIZE		DWG NO	REV
A	4	SCD Update 19.05.2010 Drawings	

SCALE 3:1 SHEET 8 OF 14

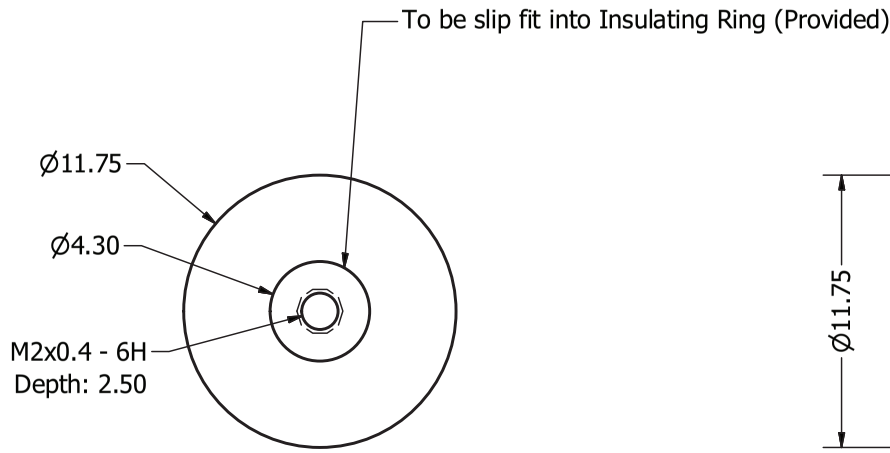

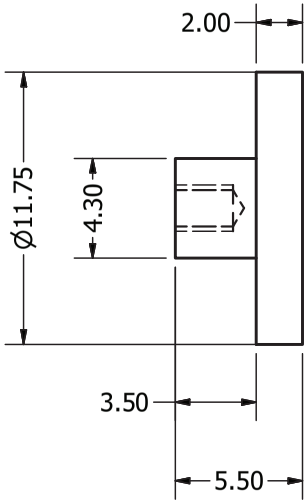

Note: Upper capacitor plate 11.75mm diameter must match as closely as possible Floating Capacitor plate diameter.

DRAWN John Dunn	11/8/2007	This component to be made from Silver Sapphire Upper Upper Insulator will be provided.
CHECKED		TITLE: Upper Capacitor Plate
QA		
MFG		
APPROVED		
SIZE A	DWG NO SCD Update 19.05.2010 Drawings	REV
SCALE	SHEET 9 OF 14	

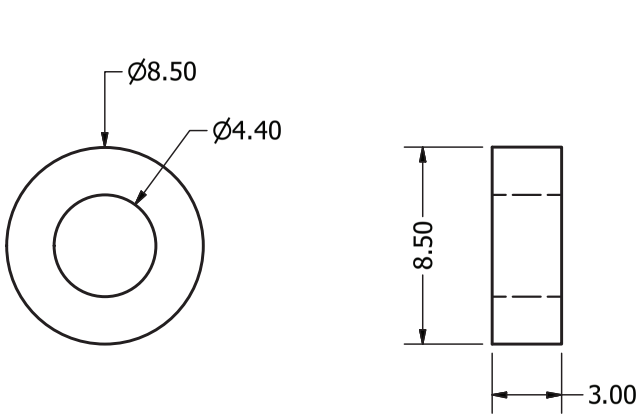

This component will be provided.

DRAWN John Dunn	11/8/2007	This component to be made of Sapphire. Measurements are approximate, should be taken from piece provided.
CHECKED		
QA		
MFG		
APPROVED		

TITLE

Insulating Ring

SIZE		DWG NO	REV
A		SCD Update 19.05.2010 Drawings	

SCALE 4:1 SHEET 10 OF 14

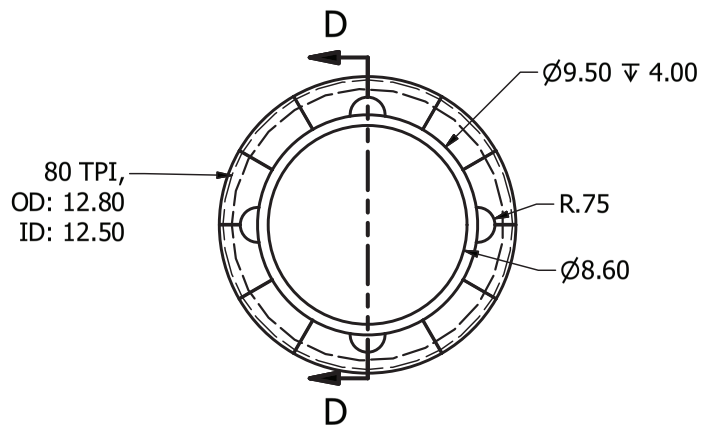

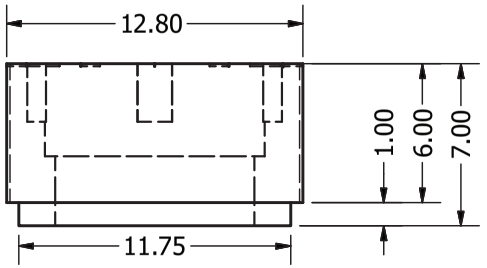

SECTION D-D
SCALE 4 : 1

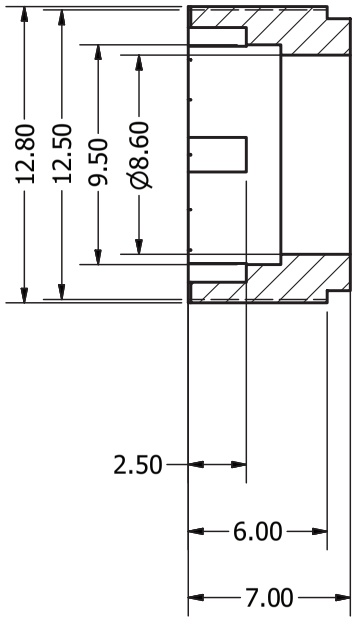

DRAWN John Dunn	11/8/2007	To be made from A316 Stainless Steel This component threads into Volume A of Shell
CHECKED		TITLE: Upper Lock Ring
QA		
MFG		
APPROVED		
		SIZE A | DWG NO SCD Update 19.05.2010 Drawings | REV
		SCALE | SHEET 11 OF 14

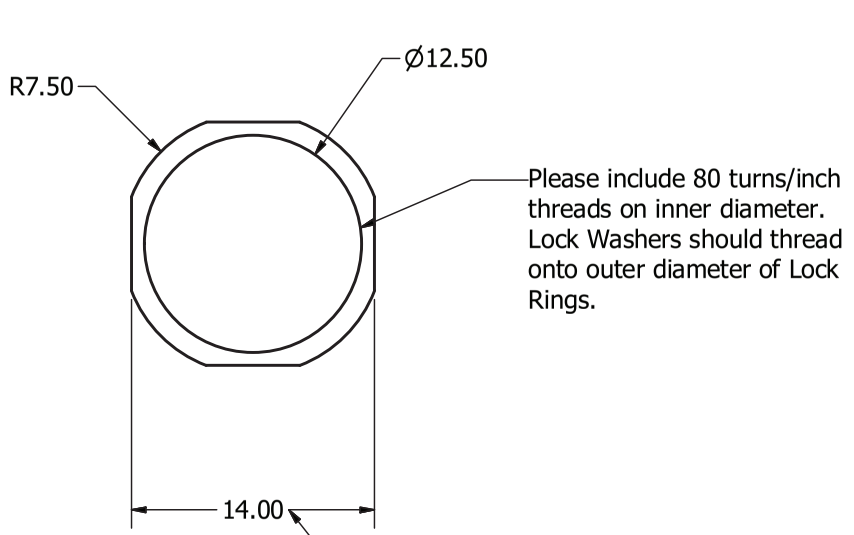

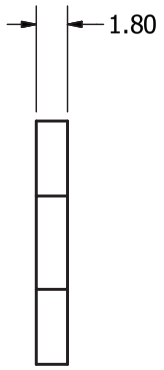

Quantity: 2

DRAWN John Dunn	11/8/2007	Please make this component from Non-Magnetic Stainless Steel (A316)
CHECKED		TITLE Lock Washer
QA		
MFG		
APPROVED		
		SIZE A / 7 / DWG NO SCD Update 19.05.2010 Drawings / REV
		SCALE 3:1 / SHEET 12 OF 14

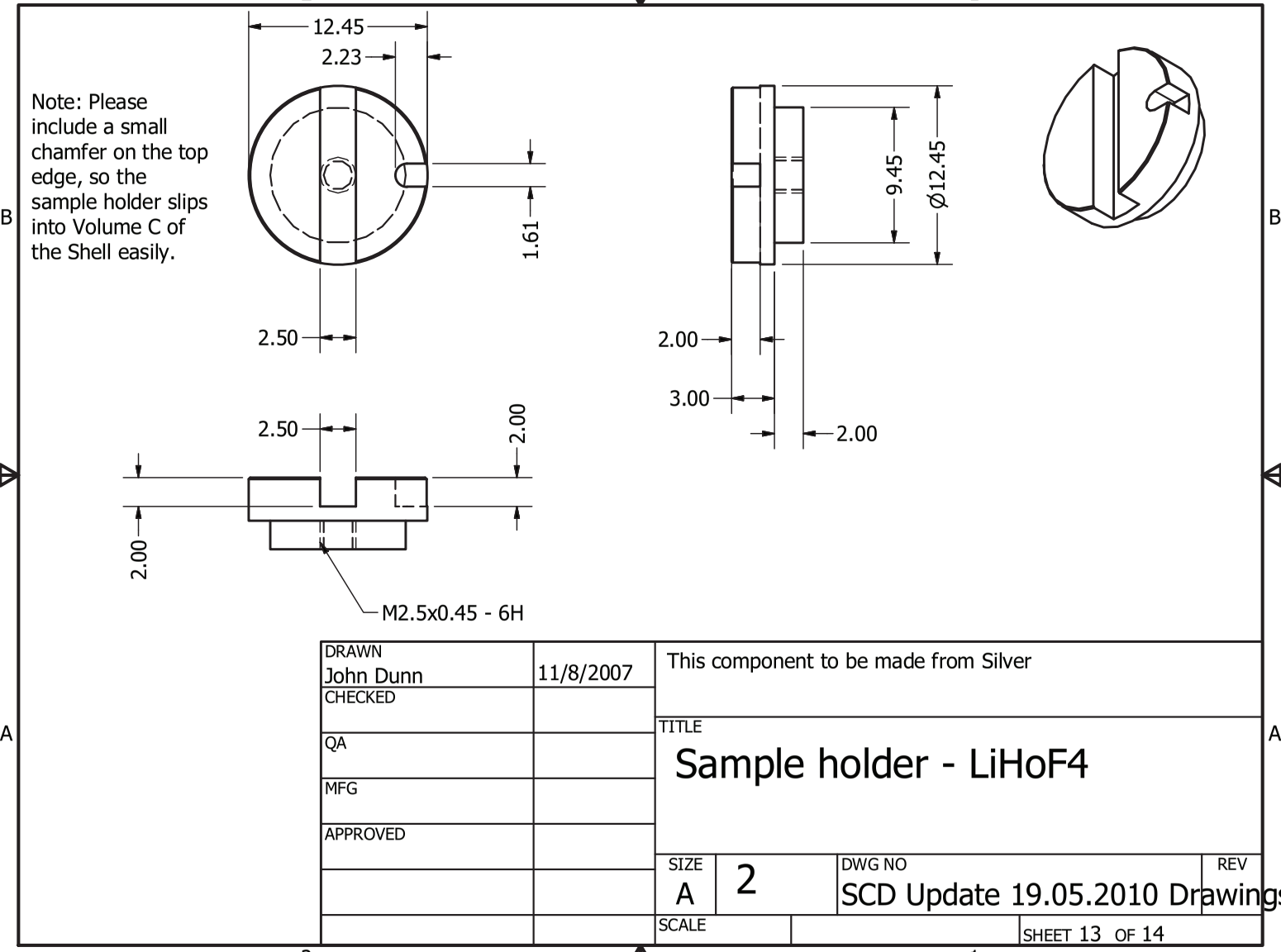

Note: Please include a small chamfer on the top edge, so the sample holder slips into Volume C of the Shell easily.

DRAWN John Dunn	11/8/2007	This component to be made from Silver
CHECKED		
QA		
MFG		
APPROVED		

TITLE

Sample holder - LiHoF4

SIZE		DWG NO	REV
A	2	SCD Update 19.05.2010 Drawings	

SCALE

SHEET 13 OF 14

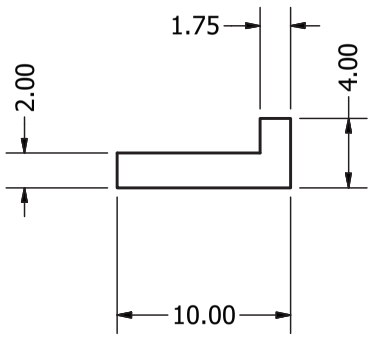

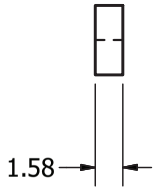

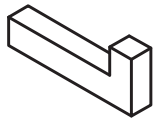

This is a key to fit into the notch cut out of the sample holder.

DRAWN John Dunn	11/8/2007	This component to be made from Stainless Steel
CHECKED		TITLE: Sample Holder Key and Lower Capacitor Nut
QA		
MFG		
APPROVED		
SIZE A	DWG NO SCD Update 19.05.2010 Drawings	REV
SCALE 3:1	SHEET 14 OF 14	

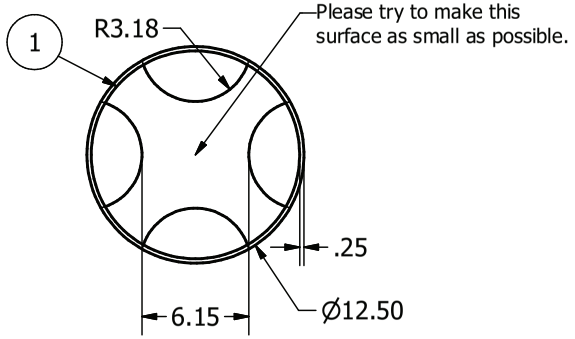

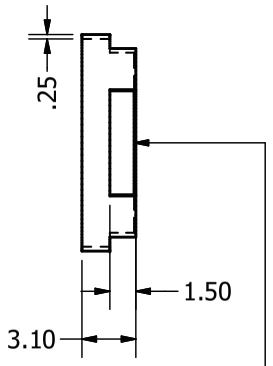

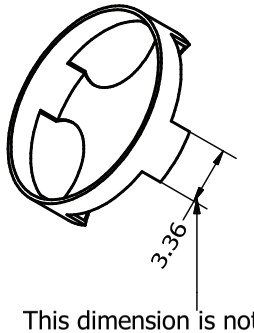

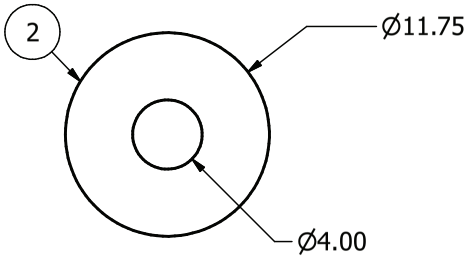

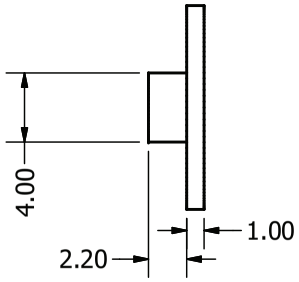

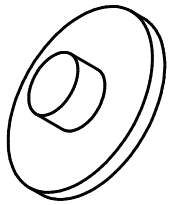

Note: Capacitor Plate (2) must sit inside of spring (1), without the edges of the plate in contact with the spring.

Spring (1) should slip fit into volume B of the Shell, resting against the shoulder between B and C.

DRAWN John Dunn	11/8/2007	The capacitor plate (2) to be made from Silver. The Spring (1) to be made from Beryllium Copper.
CHECKED		
QA		
MFG		
APPROVED		

TITLE

Lower Capacitor Plate Assembly -Spring and Plate

SIZE		DWG NO	REV
A	3	Compact Dilatometer 1	
SCALE 3:1		SHEET 4 OF 9	

References

[1] Compare, for example, the stability and accuracy of the measurement tools used by White to the current equipment offered by Andeen-Hagerling. 11

[2] Purchased from TYDEX, J.S.Co., St. Petersburg, Russia. 39

[3] A. Aharony and P. C. Hohenberg. Universal relations among thermodynamic critical amplitudes. *Phys. Rev. B*, 13(7):3081–3090, Apr 1976. 33

[4] Issam Alkhesho. Thermal conductivity measurements at very low temperatures. Master's thesis, University of Waterloo, Waterloo, Ontario, 2010. 20, 90

[5] P. W. Anderson. Ordering and antiferromagnetism in ferrites. *Phys. Rev.*, 102(4):1008–1013, May 1956. 55

[6] AS Andreenko, KP Belov, SA Nikitin, and AM Tishin. Magnetocaloric effects in rare-earth magnetic materials. *Soviet Physics Uspekhi*, 32(8):649, 1989. 10

[7] J E Battison, A Kasten, M J M Leask, J B Lowry, and B M Wanklyn. Ferromagnetism in lithium holmium fluoride-lihof 4 . ii. optical and spectroscopic measurements. *Journal of Physics C: Solid State Physics*, 8(23):4089, 1975. 1

[8] P. Beauvillain, J. P. Renard, I. Laursen, and P. J. Walker. Critical behavior of the magnetic susceptibility of the uniaxial ferromagnet liho$f$4. *Phys. Rev. B*, 18(7):3360–3368, Oct 1978. 1, 33

[9] M Beleggia, M De Graef, and Y. T. Millev. The equivalent ellipsoid of a magnetized body. *J. Phys. D: Appl. Phys.*, 39:891–899, 2006. 49

[10] A. Biltmo and P. Henelius. The ferromagnetic transition and domain structure in lihof 4. *EPL (Europhysics Letters)*, 87(2):27007, 2009. 51, 53

[11] D. Bitko and T. F. Rosenbaum. Quantum critical behavior for a model magnet. *Phys Rev Lett*, 77(5):940, 1996. 1, 26, 28, 30, 31, 33, 35, 36, 38, 39, 40, 51, 52, 53, 81

[12] B. L. Brandt, D. W. Liu, and L. G. Rubin. Low temperature thermometry in high magnetic fields. vii. cernox[trademark sign] sensors to 32 t. *Review of Scientific Instruments*, 70(1):104–110, 1999. 44

[13] H. Cao, A. Gukasov, I. Mirebeau, P. Bonville, and G. Dhalenne. Field-induced spin-ice-like orders in spin liquid $tb_2ti_2o_7$. *Phys. Rev. Lett.*, 101(19):196402, Nov 2008. 57, 69, 70, 82

[14] C. A. Catanese, A. T. Skjeltorp, H. E. Meissner, and W. P. Wolf. Magnetic and thermal properties of tb$(oh)_3$. *Phys. Rev. B*, 8(9):4223–4246, Nov 1973. 57

[15] P. B. Chakraborty, P. Henelius, H. Kjønsberg, A. W. Sandvik, and S. M. Girvin. Theory of the magnetic phase diagram of lihof$_4$. *Phys. Rev. B*, 70(144411):144411, 2004. 27, 28, 30, 31, 34, 36, 37, 38, 40, 51, 53

[16] Y. Chapuis. *Frustration géométrique, transitions de phase et ordre dynamique*. PhD thesis, Universit Joseph Fourier - Grenoble I, 2010. 61, 62, 73, 79

[17] Y. Chapuis, A. Yaouanc, P. Dalmas de Réotier, C. Marin, S. Vanishri, S. H. Curnoe, C. Vâju, and A. Forget. Evidence from thermodynamic measurements for a singlet crystal-field ground state in pyrochlore $tb_2sn_2o_7$ and $tb_2ti_2o_7$. *Phys. Rev. B*, 82(10):100402, Sep 2010. 57, 61

[18] H. P. Christensen. Spectroscopic analysis of liho$f4$ and lier$f4$. *Phys. Rev. B*, 19(12):6564–6572, Jun 1979. 34, 36

[19] P. Coleman and A. J. Schofield. *Nature*, 433:226–229, 2005. 31

[20] A. H. Cooke, D. A. Jones, J. F. A. Silva, and M. R. Wells. Ferromagnetism in lithium holmium fluoride - lihof$_4$:i. magnetic measurements. *J. Phys. C: Solid State Phys.*, 8:4083–4088, 1975. 27, 31, 36

[21] A.L. Cornelius, B.E. Light, R. S. Kumar, M. Eichenfield, T. Dutton, R. Pepin, and J.S. Gardner. Disturbing the spin liquid state in tb2ti2o7: Heat capacity measurements on rare earth titanates. *Physica B*, 359:1243–1245, 2005. 75

[22] V. F. Correa, T. P. Murphy, C. Martin, K. M. Purcell, E. C. Palm, G. M. Schmiedeshoff, J. C. Cooley, and S. W. Tozer. Magnetic-field-induced lattice anomaly inside the superconducting state of *cecoin*5: Anisotropic evidence of the possible fulde-ferrell-larkin-ovchinnikov state. *Phys. Rev. Lett.*, 98(8):087001, Feb 2007. 11

[23] Byron C. den Hertog and Michel J. P. Gingras. Dipolar interactions and origin of spin ice in ising pyrochlore magnets. *Phys. Rev. Lett.*, 84(15):3430–3433, Apr 2000. 58, 61

[24] David J. Dunlop. *Geophys. Res. Lett.*, 10:79–82, 1983. 49

[25] G. Engdahl, editor. *Handbook of Giant Magnetostrictive Materials*. Academic Press, 2000. 12, 66

[26] Matthew Enjalran and Michel J. P. Gingras. Theory of paramagnetic scattering in highly frustrated magnets with long-range dipole-dipole interactions: The case of the *tb*2*ti*2*o*7 pyrochlore antiferromagnet. *Phys. Rev. B*, 70(17):174426, Nov 2004. 63

[27] L.R. Corruccini Gang Luo, Steven T. Hess. Low temperature magnetic properties of the geometrically frustrated pyrochlores tb2ti2o7, gd2ti2o7, and gd2sn2o7. *Physics Letters A*, 291:306–310, Dec 2001. 58, 60, 73, 76

[28] J. S. Gardner, S. R. Dunsiger, B. D. Gaulin, M. J. P. Gingras, J. E. Greedan, R. F. Kiefl, M. D. Lumsden, W. A. MacFarlane, N. P. Raju, J. E. Sonier, I. Swainson, and Z. Tun. Cooperative paramagnetism in the geometrically frustrated pyrochlore antiferromagnet *tb*2*ti*2*o*7. *Phys. Rev. Lett.*, 82(5):1012–1015, Feb 1999. 57, 58, 66

[29] J. S. Gardner, B. D. Gaulin, A. J. Berlinsky, P. Waldron, S. R. Dunsiger, N. P. Raju, and J. E. Greedan. Neutron scattering studies of the cooperative paramagnet pyrochlore *tb*2*ti*2*o*7. *Phys. Rev. B*, 64(22):224416, Nov 2001. 61, 63, 64

[30] J S Gardner, B D Gaulin, and D. McK Paul. Single crystal growth by the floating-zone method of a geometrically frustrated pyrochlore antiferromagnet, tb2ti2o7. *Journal of Crystal Growth*, 191(4):740–745, 1998. 71

[31] J. S. Gardner, A. Keren, G. Ehlers, C. Stock, Eva Segal, J. M. Roper, B. Fåk, M. B. Stone, P. R. Hammar, D. H. Reich, and B. D. Gaulin. Dynamic frustrated magnetism in *tb*2*ti*2*o*7 at 50 mk. *Phys. Rev. B*, 68(18):180401, Nov 2003. 54, 57, 58, 73

[32] Jason S. Gardner, Michel J. P. Gingras, and John E. Greedan. Magnetic pyrochlore oxides. *Rev. Mod. Phys.*, 82(1):53, Jan 2010. 2, 10, 55, 57, 66, 79

[33] M. Garst and Achim Rosch. Sign change of the grüneisen parameter and magnetocaloric effect near quantum critical points. *Physical Review B*, 72:205129, 2005. 9, 10

[34] M. J. P. Gingras and B. C. den Hertog. Origin of spin-ice behavior in ising pyrochlore magnets with long-range dipole interactions: an insight from mean-field theory. *Can. J. Phys.*, 79(11-12):13391351, Sep 2001. 56

[35] M. J. P. Gingras, B. C. den Hertog, M. Faucher, J. S. Gardner, S. R. Dunsiger, L. J. Chang, B. D. Gaulin, N. P. Raju, and J. E. Greedan. Thermodynamic and single-ion properties of *tb*3+ within the collective paramagnetic-spin liquid state of the frustrated pyrochlore antiferromagnet *tb*2*ti*2*o*7. *Phys. Rev. B*, 62(10):6496–6511, Sep 2000. 55, 57, 58, 59, 61, 75

[36] J. A. Griffin, M. Huster, and Robert J. Folweiler. Critical behavior of the spontaneous magnetization at marginal dimensionality in liho$f$4. *Phys. Rev. B*, 22(9):4370–4378, Nov 1980. 33

[37] Nobuko Hamaguchi, Taku Matsushita, Nobuo Wada, Yukio Yasui, and Masatoshi Sato. Low-temperature phases of the pyrochlore compound *tb*2*ti*2*o*7. *Phys. Rev. B*, 69(13):132413, Apr 2004. 58, 60, 61, 62, 76

[38] P. E. Hansen, T. Johansson, and R. Nevald. Magnetic properties of lithium rare-earth fluorides: Ferromagnetism in lierf_4 and lihof_4 and crystal-field parameters at the rare-earth and li sites. *Phys. Rev. B*, 12(5315):5315 – 5324, 1975. 27, 28, 31, 34, 36

[39] M. J. Harris, S. T. Bramwell, P. C. W. Holdsworth, and J. D. M. Champion. Liquid-gas critical behavior in a frustrated pyrochlore ferromagnet. *Phys. Rev. Lett.*, 81(20):4496–4499, Nov 1998. 55

[40] I.V. I. V. Alexandrov, B.V. Lidskii, G. Mamsurova, M.G. Neigauz, K.S. Pigalskii, K.K. Pukhov, N.G. Trusevich, and L.G. Shcherbakova. Ordering and antiferromagnetism in ferrites. *Sov. Phys. JETP*, 62(2):1287, 1985. 63, 67, 76, 78, 79

[41] Ying-Jer Kao, Matthew Enjalran, Adrian Del Maestro, Hamid R. Molavian, and Michel J. P. Gingras. Understanding paramagnetic spin correlations in the spin-liquid pyrochlore *tb*2*ti*2*o*7. *Phys. Rev. B*, 68(17):172407, Nov 2003. 61

[42] A. Keren, J. S. Gardner, G. Ehlers, A. Fukaya, E. Segal, and Y. J. Uemura. Dynamic properties of a diluted pyrochlore cooperative paramagnet $(tb_py_{1-p})_2ti_2o_7$. *Phys. Rev. Lett.*, 92(10):107204, Mar 2004. 57

[43] Lakeshore Cryotonics. *Model 331 User Manual*. Westerville, Ohio, 2005. 93

[44] L.D. Landau and E.M. Lifshitz. *Statistical Physics*. Addison-Wesley Publishing Co., Don Mills, Ontario, 1969. 9

[45] E. W. Lee. Magnetostriction and magnetomechanical effects. *Rep. Prog. Phys*, 18:184–229, 1955. 3, 7

[46] J. Magariño, J. Tuchendler, P. Beauvillain, and I. Laursen. Epr experiments in litb$f$4, liho$f$4, and lier$f$4 at submillimeter frequencies. *Phys. Rev. B*, 21(1):18–28, Jan 1980. 36, 37

[47] I. Mirebeau, P. Bonville, and M. Hennion. Magnetic excitations in *tb*2*sn*2*o*7 and *tb*2*ti*2*o*7 as measured by inelastic neutron scattering. *Phys. Rev. B*, 76(18):184436, Nov 2007. 57, 63

[48] I. Mirebeau, I. N. Goncharenko, P. Cadavez-Peres, S. T. Bramwell, M. J. P. Gingras, and J. S. Gardner. Pressure-induced crystallization of a spin liquid. *Nature*, 420:54–57, Sept 2002. 69

[49] H. R. Molavian, P. A. McClarty, and M. J. P. Gingras. Towards an Effective Spin Hamiltonian of the Pyrochlore Spin Liquid Tb2Ti2O7. *ArXiv e-prints*, December 2009. 63, 65, 66

[50] Hamid R. Molavian, Michel J. P. Gingras, and Benjamin Canals. Dynamically induced frustration as a route to a quantum spin ice state in *tb*2*ti*2*o*7 via virtual crystal field excitations and quantum many-body effects. *Phys. Rev. Lett.*, 98(15):157204, Apr 2007. 63, 64, 66

[51] L. Neel. *Advances in Physics*, 4:191–242, 1955. 49

[52] James Nikkel and Brett Ellman. Testing renormalization group theory at the critical dimension in lihof$_4$. *Phys Rev B*, 64:214420, 2001. 27, 28, 33, 39, 40, 41, 42, 44

[53] N.D. Mermin N.W. Ashcroft, editor. *Solid State Physics*. Thomson Learning, 1976. 28

[54] Pathria, editor. *Statistical Mechanics*. Elsevier, 1996. 3, 27

[55] Linus Pauling. The structure and entropy of ice and of other crystals with some randomness of atomic arrangement. *Journal of the American Chemical Society*, 57(12):2680–2684, 1935. 55

[56] F. Pobell, editor. *Matter and Methods at Low Temperatures*. Springer, New York, 1996. 12, 73

[57] R Pott and R Schefzyk. Apparatus for measuring the thermal expansion of solids from 1.5 to 380 k. *J. Phys. E.:Sci. Instrum.*, 16:444–449, 1983. 18

[58] J.A. Quilliam. *Disorder, Geometric Frustration and the Dipolar Interaction in Rare-Earth Magnets*. PhD thesis, 2010. 81

[59] Somayyeh Rahimi. Thermal and charge conductivities of superconducting skutterudite compounds, prru4sb12 and pros4sb12. Master's thesis, University of Waterloo, Waterloo, Ontario, 2007. 20, 90

[60] F. Reif, editor. *Fundamentals of thermal and statistical physics*. McGraw-Hill, 1965. 5, 7

[61] H. M. Rønnow, J. Jensen, R. Parthasarathy, G. Aeppli, T. F. Rosenbaum, D. F. McMorrow, and C. Kraemer. Magnetic excitations near the quantum phase transisiotn in the ising ferromagnet lihof$_4$. *Phys. Rev. B*, 75(054426):054426, 2007. 27, 31, 36, 38, 51, 52

[62] H. M. Rønnow, R. Parthasarathy, J. Jensen, G. Aeppli, T. F. Rosenbaum, and D. F. McMorrow. Quantum phase transition of a magnet in a spin bath. *Science*, 308, 2005. 33, 36, 39, 51, 52, 81

[63] J. P. C. Ruff, B. D. Gaulin, J. P. Castellan, K. C. Rule, J. P. Clancy, J. Rodriguez, and H. A. Dabkowska. Structural fluctuations in the spin-liquid state of *tb*2*ti*2*o*7. *Phys. Rev. Lett.*, 99(23):237202, Dec 2007. 66, 68, 69, 75, 79, 82

[64] J. P. C. Ruff, Z. Islam, J. P. Clancy, K. A. Ross, H. Nojiri, Y. H. Matsuda, H. A. Dabkowska, A. D. Dabkowski, and B. D. Gaulin. Magnetoelastics of a spin liquid: X-ray diffraction studies of $tb_2ti_2o_7$ in pulsed magnetic fields. *Phys. Rev. Lett.*, 105(7):077203, Aug 2010. 66, 68, 69, 79

[65] D.L. Rule, D.R. Smith, and L.L. Sparks. Thermal conductivity of a polyimide film between 4.2 and 300k, with and without alumina particles as filler. *NISTIR*, (3948), 1990. 73

[66] K. C. Rule, J. P. C. Ruff, B. D. Gaulin, S. R. Dunsiger, J. S. Gardner, J. P. Clancy, M. J. Lewis, H. A. Dabkowska, I. Mirebeau, P. Manuel, Y. Qiu, and J. R. D. Copley. Field-induced order and spin waves in the pyrochlore antiferromagnet $tb_2ti_2o_7$. *Phys. Rev. Lett.*, 96(17):177201, May 2006. 69, 70, 82

[67] S. Sachdev, editor. *Quantum Phase Transitions*. Cambridge University Press, 2009. 27, 28

[68] Subir Sachdev. Quantum magnetism and criticality. *Nature Physics*, 4:173–185, Mar 2008. 27

[69] S Salaün, M T Fornoni, A Bulou, M Rousseau, P Simon, and J Y Gesland. Lattice dynamics of fluoride scheelites: I. raman and infrared study of $liyf_4$ and $lilnf_4$ (ln = ho, er, tm and yb). *J. Phys.: Cond. Matt.*, 9(32):6941, 1997. 36

[70] A. Sawada, T. Kubo, Y. Fujii, T. Komatsubara, Y. Onuki, N. Kimura, E. Yamamoto, and Y. Haga. Thermal expansion anomaly of upt3 below 70 mk. *Czech. Jour. Phys.*, 46:803–804, 1996. 11

[71] G. M. Schmiedeshoff. A versatile and compact capacitive dilatometer. *Rev. Sci. Instrum.*, 77:123907, 2006. 18, 81, 87

[72] F. Schwabl, editor. *Statistical Mechanics*. Springer, 2005. 3, 7

[73] G.S. Shakurov, M.V. Vanyunin, B.Z. Malkin, B. Barbara, R.Yu. Abdulsabirov, and S.L. Korableva. Direct measurements of anticrossings of the electron-nuclear energy levels in liyf4:ho3+ with submillimeter epr spectroscopy. *Applied Magnetic Resonance*, 28(3):251, 2005. 38

[74] David R. Smith and F. R. Fickett. Low-temperature properties of silver. *J. Res. Natl. Inst. Stand. Technol.*, 100:119 – 171, 1995. 12, 25

[75] S. L. Sondhi, S. M. Girvin, J. P. Carini, and D. Shahar. Continuous quantum phase transitions. *Rev. Mod. Phys.*, 79(1):315, 1997. 27, 31

[76] H. Eugene Stanley. *Introduction to Phase Transitions and Critical Phenomena*. Clarendon Press, Oxford, UK, 1971. 3, 4, 5, 6, 7, 8, 9

[77] P. Stasiak and M. J. P. Gingras. Assessment of the re(oh)3 ising magnetic materials as possible candidates for the study of transverse-field-induced quantum phase transitions. *Phys. Rev. B*, 78:224412, 2008. 53

[78] C. A. Swenson. *Thermal Expansion of Solids*, page 207. ASM International, 1998. 18

[79] S. M. A. Tabei, M. J. P. Gingras, Y. J. Kao, and T. Yavors'kii. Perturbative quantum monte carlo study of lihof$_4$ in a transverse magnetic field. *Phys Rev B*, 78:184408, 2008. 1, 26, 28, 29, 30, 31, 37, 38, 51, 52, 53, 81

[80] Jacques Villain. Insulating spin glasses. *Zeitschrift fr Physik B Condensed Matter*, 33:31–42, 1979. 10.1007/BF01325811. 55

[81] G. K. White. Measurement of thermal expansion at low temperatures. *Cryogenics*, 1:151–158, March 1961. 11

[82] G. K. White. Reference materials for thermal expansion: certified or not? *Thermochimica Acta*, 218:83–99, 1993. 24, 25

[83] G. K. White and J. G. Collins. Thermal expansion of copper, silver, and gold at low temperatures. *Journal of Low Temperature Physics*, 7(1/2):43–75, 1972. 17, 76

[84] G. K. White and J.G. Collins. Thermal Expansion of Copper, Silver, and Gold at Low Temperatures. *Journal of Low Temperature Physics*, 7(1), 1972. 24, 25, 77

[85] W. P. Wolf. The ising model and real magnetic materials. *Braz. J. Phys. [online]*, 30:794–810, 2000. 27

[86] Bernard Yates. *Thermal Expansion*. Plenum Press, New York, USA, 1972. 3, 8

[87] Lijun Zhu, Markus Garst, Achim Rosch, and Qimiao Si. Universally diverging grüneisen parameter and the magnetocaloric effect close to quantum critical points. *Phys. Rev. Lett.*, 91(6):066404, Aug 2003. 9, 10